Department of Physics and Astronomy
Heidelberg University

Master Thesis in Physics
submitted by

Nele Marie Griesbach

born in Reutlingen (Germany)

2025

Light-Shift Gates in a 2D Trapped-Ion Quantum Simulator

This Master Thesis has been carried out by *Nele Marie Griesbach* at the
Physikalisches Institut Heidelberg under the supervision of
Prof. Dr. Lauriane Chomaz
and
Assoz. Prof. Dr. Christian F. Roos,
Institut für Experimentalphysik Innsbruck.

Abstract

Trapped-ion systems represent one of the most promising platforms for quantum information processing, offering long qubit coherence times and exceptional control over qubit operations. A key ingredient for scalable quantum computation and quantum simulation is the implementation of high-fidelity quantum gates, which enable control of entanglement and superposition. In this work, experiments are performed with up to 105 $^{40}Ca^{+}$ ions confined in planar Coulomb crystals, forming a versatile quantum simulator capable of emulating transverse-field Ising models. To extend the accessible class of spin Hamiltonians and to increase the flexibility of the system, light-shift gates are implemented to realize ZZ-type entangling interactions. These gates allow for selective two-qubit coupling between arbitrary pairs of ions within large crystals. The light-shift gate is driven by a laser field far detuned from all electronic transitions, which suppresses photon scattering and thus supports high-fidelity operation. This thesis presents the underlying theoretical framework, simulations of the gate mechanism, detailed calibration procedures, and experimental results demonstrating successful light-shift gate operation with fidelities of up to 90 %.

ZUSAMMENFASSUNG

Gefangene Ionen stellen eine der vielversprechendsten Plattformen für die Quanteninformationsverarbeitung dar, da sie lange Qubit-Kohärenzzeiten und eine außergewöhnliche Kontrolle über Qubit-Operationen bieten. Ein wesentlicher Bestandteil für skalierbare Quantenberechnungen und Quantensimulationen ist die Implementierung von hochpräzisen Quantengattern, die eine Steuerung von Verschränkung und Überlagerung ermöglichen. In dieser Arbeit werden Experimente mit bis zu 105 $^{40}Ca^{+}$-Ionen durchgeführt, welche planare Ionenkristalle bilden und einen vielseitigen Quantensimulator bilden, der Ising-Modelle mit transversalem Feld simulieren kann. Um die zugängliche Klasse von Spin-Hamilton-Operatoren zu erweitern und die Flexibilität des Systems zu erhöhen, werden Lichtverschiebungsgatter implementiert, um ZZ-artige Verschränkungswechselwirkungen zu realisieren. Diese Gatter ermöglichen eine selektive Zwei-Qubit-Kopplung zwischen beliebigen Ionenpaaren innerhalb großer Kristalle. Das Lichtverschiebungsgatter wird durch ein Laserfeld angesteuert, das weit von allen elektronischen Übergängen verstimmt ist, wodurch die Photonenstreuung unterdrückt wird und somit eine hochpräzise Operation unterstützt wird. Diese Arbeit präsentiert den zugrunde liegenden theoretischen Rahmen, Simulationen des Gattermechanismus, detaillierte Kalibrierungsverfahren und experimentelle Ergebnisse, die den erfolgreichen Betrieb des Lichtverschiebungsgatters mit einer Gattergüte von bis zu 90 % belegen.

CONTENTS

1

INTRODUCTION

One of the landmark achievements in modern science is the development of quantum mechanics, a framework that fundamentally reshaped our understanding of the microscopic world and gave rise to research fields such as atomic, nuclear, and particle physics, as well as condensed matter physics and quantum chemistry. Its principles enabled transformative technologies, including the laser [1–3] and semiconductor-based devices for classical information processing, collectively known as the first quantum revolution. These technologies, while rooted in quantum mechanics, do not involve direct control of individual quantum systems or exploit uniquely quantum phenomena such as coherent superposition and entanglement. Only in the past three decades have such capabilities become experimentally accessible, driven by advances in atomic physics, laser technology, materials science, and the theoretical framework of quantum information processing [4]. These advancements mark a fundamental shift in the utilization of quantum systems and is commonly referred to as the "second quantum revolution" [5].

The complexity of quantum many-body systems, which underlies phenomena such as quantum magnetism and high-temperature superconductivity, has long been recognized. While the exponential growth of the Hilbert space is not necessarily prohibitive for analytical approaches, these systems are intrinsically intricate, often making exact analytical or numerical simulations intractable. While various approximation methods exist, they are typically limited in scalability or accuracy [6], or only applicable to states with low amounts of entanglement. Exotic highly-entangled states often remain inaccessible to these approaches [7, 8]. Only in recent decades has it become possible to study such systems directly in the laboratory through quantum simulation, as proposed by R. Feynman in 1982 [9], where controllable quantum platforms emulate the dynamics of the target system. To implement such simulations and perform quantum computations, it is necessary to represent and manipulate information at the level of individual quantum systems. This can be achieved using qubits, which form the fundamental units of quantum information. Analogous to classical information processing, in which information is encoded in binary bits taking the values 0 or 1, quantum information processing relies on qubits. Qubits are defined by two orthogonal quantum states, typically denoted as

1

$|0\rangle$ and $|1\rangle$. In contrast to classical bits, qubits can exist in arbitrary coherent superpositions of these basis states. Moreover, when multiple qubits are involved, they can form entangled states exhibiting correlations that cannot be explained within any classical framework. Various physical systems can serve as qubits, provided they possess at least two well-defined and addressable energy levels corresponding to the computational basis states $|0\rangle$ and $|1\rangle$. In addition, viable qubit implementations must meet a series of criteria [10], including reliable initialization and readout mechanisms, as well as long coherence times. To exploit these properties, quantum gates are implemented to coherently manipulate qubits in a controlled manner. These gates form the building blocks of quantum algorithms, enabling both quantum computing, where information is processed in ways beyond the reach of classical computers, and quantum simulation, where qubits emulate complex physical systems. Quantum gates can be used to generate superposition states or entangled states. Single-qubit gates change the state of individual qubits, while two-qubit (or multi-qubit) gates produce entangling interactions, enabling the implementation of quantum algorithms and the simulation of interacting quantum systems [11]. The ability to realize physical qubits and to prepare them in coherent superposition or entangled states has enabled a range of novel and potentially innovative applications.

Among various experimental platforms, trapped ions have emerged as an interesting system for quantum simulation. The ability to encode spin-lattice systems in trapped-ion crystals, combined with their long coherence times and the availability of advanced methods for state preparation, coherent control, and high-fidelity readout, establishes trapped ions as a powerful and versatile platform for the study of quantum magnetism [12–17]. In particular, analog and variational quantum simulation experiments have demonstrated precise manipulation of large ion crystals, enabling the exploration of quantum many-body physics with systems comprising tens to hundreds of particles [18–23]. Spin-1/2 particle ensembles, relevant to condensed matter magnetism and molecular excitation transport [24], become especially challenging to simulate for higher-dimensional lattices or in the presence of long-range interactions. Trapped-ion quantum simulators can directly probe such regimes. Scaling requires precise control of large ion arrays, achieved using Penning [25, 26] or Paul traps [21, 27]. Generating quantum correlations and studying many-body physics requires entangling interactions. In their absence, each qubit would evolve independently, and the simulator could only reproduce trivial, non-interacting spin dynamics - well within classical computational reach. The complexity of phenomena such as quantum magnetism, spin transport, and phase transitions arises from interaction terms in the system Hamiltonian, whose faithful implementation on a quantum simulator demands interaction terms between the individual spins.

In this work, we make use of a linear Paul trap, where we are able to confine up to 105 $^{40}Ca^{+}$, arranged into planar Coulomb crystals [23]. In the existing setup, global entangling interactions are implemented using techniques similar to Mølmer–Sørensen gates [28, 29], a well-established scheme in trapped-ion systems. They provide a powerful resource for generating as an example collective XX, YY or XY couplings and thereby permitting the study of transverse-field Ising models [14]. However, these gates do not directly provide ZZ couplings, which are essential for simulating a broader class of spin

Hamiltonians and implementing certain quantum information protocols. While global entangling interactions are a powerful tool to generate collective XX and XY couplings, it is also advantageous to additionally implement two-qubit gates to selectively entangle arbitrary pairs of ions. In particular, such gates enable the preparation of nontrivial input states tailored to the Hamiltonian under investigation, thereby expanding the range of accessible quantum simulations and increasing the simulator's versatility. In quantum computing these gates can be used for universal gate sets and efficient circuit compilation.

To enable such selective interactions, we employ light-shift gates that realize controllable two-qubit ZZ interactions. The basic concept was first suggested by Milburn, based on the subsequent theoretical works [29–31] and later experimentally developed by Leibfried et al. [32]. These gates are geometric phase gates, meaning that they act by imprinting a phase without altering the motional state. The mechanism relies on state-dependent optical dipole forces that coherently displace the ions' shared motional state in phase space. As the trajectory closes, the system acquires a geometric phase determined solely by the enclosed area, independent of the initial motional state. When the force differs for the two states of the ions, this phase becomes conditional, thereby implementing an entangling gate between the selected qubits. To experimentally realize controllable two-qubit interactions within our system, we combine tightly focused addressing beams for single-qubit rotations with a global beam that mediates the entangling interaction, coupling only to ions prepared in the computational subspace. We employ a laser operating at a wavelength of 532 nm. This choice offers two key advantages. First, high-power laser systems at this wavelength are commercially available and therefore straightforward to implement in the experimental setup. Second, 532 nm light is far detuned from any electronic transition in $^{40}Ca^{+}$, which suppresses photon scattering. The resulting scattering rate reduces to the order of 2.4×10^{-5} Hz for an intensity of 637 MW m^{-2} [33]. Photon scattering is one of the dominant intrinsic error mechanisms in laser-driven entangling gates, as it leads to decoherence of the motional and internal states of the ions. Reducing the scattering rate is therefore essential for achieving high-fidelity operations. At 532 nm, the large detuning ensures that scattering is no longer the limiting factor. Instead, the ultimate fidelity of the gate is determined by other mechanisms, most prominently the finite lifetime of the metastable D state. The feasibility of high-fidelity gates under such conditions has been analyzed theoretically by Sawyer and Brown [33] and confirmed experimentally by Clark et al. [34] for a pair of ions.

This work presents simulations, calibration procedures, and experimental results related to the implementation of the light-shift gate. Chapter 2 introduces the fundamental principles of quantum information processing with trapped ions. Chapter 3 discusses atom–light interactions, including AC Stark shifts, geometric phase gates, and scattering processes. The experimental apparatus used for the measurements is described in Chapter 4. Chapter 5 presents and analyzes the experimental implementation of the light-shift gate. Moreover, prospective system upgrades aimed at achieving higher gate fidelities are discussed in Chapter 6. Finally, Chapter 7 summarizes the key results and provides an outlook on future developments.

2

Quantum Information with Trapped Ions

This chapter introduces the fundamental principles of using trapped ions as a platform for quantum information processing. First, we present the qubit, the basic unit of quantum information (Sec. 2.1). We then explain how individual ions encode qubits (Sec. 2.2), focusing on the $^{40}Ca^{+}$ ion, favored in experiments for its atomic structure and accessible optical transitions. Subsequently, we describe the mechanism by which ions are confined using Paul traps. Finally, we briefly explain how multiple trapped ions can be harnessed to simulation interacting quantum spin models (Sec. 2.3). These systems provide a versatile and highly controllable platform for exploring many-body quantum dynamics and serve as a powerful tool in the broader context of quantum simulation.

2.1 QUBITS

In classical computing, a bit serves as the fundamental unit of information, existing in one of two distinct states, commonly denoted as 0 and 1. Similarly, in quantum computing, a quantum bit, or qubit for short, is represented using two quantum states, $|0\rangle$ and $|1\rangle$ [4]. Unlike classical bits, qubits have the unique ability to exist in other states than $|0\rangle$ and $|1\rangle$ as well. In general, they form coherent superpositions of the two basis states $|0\rangle$ and $|1\rangle$:

$$|\Psi\rangle = \alpha|0\rangle + \beta|1\rangle, \tag{2.1}$$

where $\alpha, \beta \in \mathbb{C}$ are complex probability amplitudes satisfying the normalization condition $|\alpha|^2 + |\beta|^2 = 1$. This means, a qubit can be encoded in any arbitrary superposition state of $|0\rangle$ and $|1\rangle$. However, upon measurement, the outcome is always binary, corresponding to one of the two eigenstates of the chosen measurement basis (e.g., $|0\rangle$ or $|1\rangle$ in the computational basis), determined by the probabilities $|\alpha|^2$ and $|\beta|^2$. In laboratory experiments, qubits can be implemented using a variety of physical platforms. Prominent examples include neutral atoms [35], trapped ions [36], superconducting circuits [37] and photons [38]. In the latter case, the qubit is typically encoded in the polarization state of single photons, where the basis states are formed by left-handed and right-handed polarization states.

To visualize the state of a single qubit, the Bloch sphere is often used, as shown in Fig. 2.1. For this, we can rewrite Eq. 2.1 as

$$|\Psi\rangle = \cos\frac{\theta}{2}|0\rangle + e^{i\varphi}\sin\frac{\theta}{2}|1\rangle, \tag{2.2}$$

where θ and φ are polar coordinates.

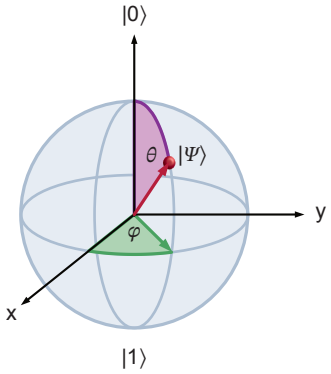

Figure 2.1: **Representation of qubit states on a Bloch sphere**. The states $|0\rangle$ and $|1\rangle$ are located at the north and south poles, respectively. Any pure qubit state $|\Psi\rangle$, as indicated by the red arrow, corresponds to a point on the sphere's surface and is fully specified by the polar and azimuthal angles θ and φ.

The fundamental advantage of quantum computation becomes increasingly evident as the number of qubits in a system grows. For this, we assume a system of n qubits, which

are represented in a computational basis where each basis takes the form $|x_1 x_2 ... x_n\rangle$, respresenting a classical bit string with $x_i \in \{0,1\}$. Consequently, the quantum state of such a system is defined by 2^n amplitudes, highlighting the exponential growth of computational resources compared to classical systems. Multi-qubit states $|\Psi\rangle$ can be described by the tensor product of the individual single qubit states $|\Psi_i\rangle$:

$$|\Psi\rangle = |\Psi_1\rangle \otimes |\Psi_2\rangle \otimes ... \otimes |\Psi_n\rangle . \tag{2.3}$$

2.2 TRAPPED IONS AS QUBITS

To achieve precise control over ions, it is necessary to confine them within a well-defined region of space, using electromagnetic interactions. Due to the constraints imposed by Maxwell's equations, it is fundamentally impossible to generate a purely electrostatic potential that confines charged particles in all three spatial dimensions. This is also known as Earnshaw's theorem. To overcome this limitation, a widely adopted approach involves employing a combination of static (DC) and oscillating (RF) electric fields to create a time-averaged restoring forces that gives rise to an anisotropic harmonic potential [32]. Traps that utilize this technique are known as Paul traps and were first developed by Wolfgang Paul [39]. In the following, the specific ion species employed in this work - singly ionized calcium ($^{40}Ca^+$) - will be introduced and discussed in detail.

2.2.1 CALCIUM ION

To trap ions as qubits, a number of prerequisites must be met. The trapped ion needs to offer a range of accessible optical transitions, which allow for efficient laser cooling. Additionally, it should exhibit long-lived electronic states for qubit encoding, together with optical transitions that permit laser-based coherent manipulation. Group-2 atomic ions are widely employed for this purpose, as their single valence electron gives rise to a hydrogen-like energy level structure.

In our case, we use $^{40}Ca^+$ ions - a system extensively studied and well-established in Innsbruck's quantum information research. This isotope has no nuclear spin, and therefore no hyperfine splitting, simplifying its energy level structure. Its transition frequencies between its low-lying electronic states span from the near-ultraviolet to the near-infrared, which makes it compatible with commercially available laser sources. The simplified level-structure of $^{40}Ca^+$ is shown in Fig. 2.2. The ions undergo two distinct cooling processes to reach near the motional ground state: Doppler cooling and ground-state cooling via electromagnetically induced transparency (EIT) cooling (for more information on EIT cooling see Ref. [40, 41]), by using 397 nm light via the dipole transition $S_{1/2} \leftrightarrow P_{1/2}$. Simultaneously, this transition is also used to read out the state of the ion via spatially resolved fluorescence measurements. To prevent optical pumping to the metastable $D_{3/2}$ state during cooling or detection, a 866 nm repump laser is used. By applying an external magnetic field, the Zeeman effect lifts the degeneracy of the electronic levels, causing a splitting into m_j sublevels, which range from $-J$ to $+J$. These Zeeman-split states provide the basis for encoding qubits. We typically use two different qubit encodings. The first is a ground-state (GS) qubit formed by $|1\rangle = S_{1/2}(m_j = -1/2)$ and $|0\rangle = S_{1/2}(m_j = +1/2)$. The second is an optical qubit formed by one of the $S_{1/2}(m_j = \pm 1/2)$ ground states and one of

the $D_{5/2}(m_j = -5/2, ..., +5/2)$. While the optical qubit is controlled with an ultranarrow ($\approx$1 Hz) laser at 729 nm, the GS qubit can be manipulated with an RF coil or a Raman transition employing a laser with a wavelength of 395 nm.

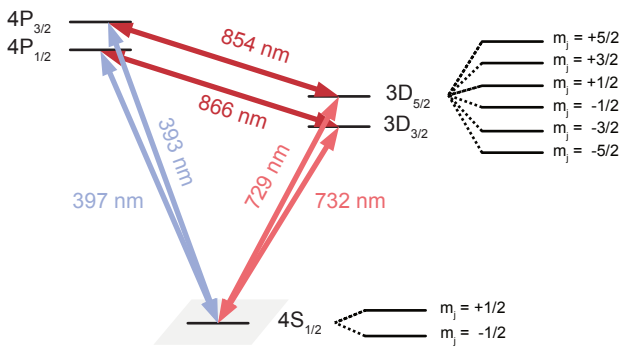

Figure 2.2: **Reduced energy level diagram of $^{40}Ca^+$**. The ion is Doppler cooled and read out via the $S_{1/2} \leftrightarrow P_{1/2}$ dipole transition with 397 nm light. The optical qubit is encoded in the two Zeeman sublevels of the $S_{1/2} \leftrightarrow D_{5/2}$ transition and controlled using 729 nm light. To prevent optical pumping to the metastable states $D_{3/2}$ and $D_{5/2}$, two repump lasers at 854 nm and 866 nm are used.

2.2.2 IDEAL LINEAR PAUL TRAP

Having identified the ion species, we now turn to the method of confinement. The Coulomb interaction of charged particles with electromagnetic fields enables trapping in a localized region for extended durations. Wolfgang Paul demonstrated in 1953 that RF fields can be used for mass-selective ion confinement [39], leading to the development of the Paul trap. In its linear configuration, ions are confined in two dimensions by a high-frequency electric quadrupole field, where the trajectory stability is determined by the charge-to-mass ratio Ze/m. By using four hyperbolic electrodes that span along the z-axis (see Fig. 2.3), the ideal undisturbed quadrupole potential is given by

$$\Phi_{\text{dyn}}(x, y, t) = \Phi_0(t) \cdot \frac{(x^2 - y^2)}{r_0^2}, \tag{2.4}$$

where $2r_0$ is the distance between two opposite electrodes with the potential $\pm\Phi_0$. Here, the voltage Φ_0 is characterized by an AC field V with frequency Ω and a DC field U of the form

$$\Phi_0(t) = U + V \cos \Omega t. \tag{2.5}$$

Due to the periodic change of sign of the electric force, this gives rise to alternating focusing and defocusing in both spatial directions. With a suitable frequency, this leads to a stable ion trajectory following the strong-focusing concept known from accelerator physics [39, 42]. In addition, we can apply a static potential to the end cap electrodes, held at a potential of U_0, to enable confinement in the axial direction. Close to the trap

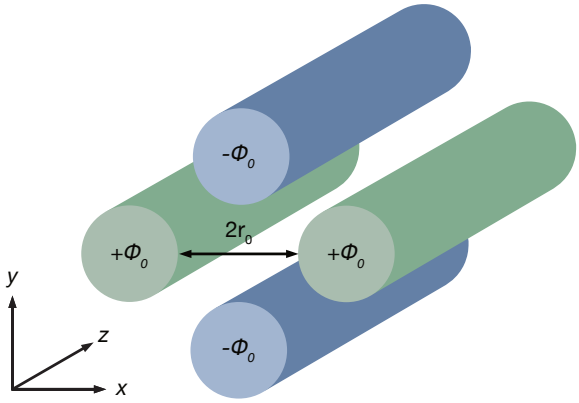

Figure 2.3: **Ideal linear Paul trap**. Radial confinement in the $x-y$ is provided by opposing electrode pairs driven with RF voltages ($\pm\Phi_0$), where the electrode spacing is $2r_0$.

center, the trapping potential can be approximated by

$$\Phi_{\text{stat}}(x,y,z) = \frac{\kappa U_0}{z_0^2}\left(z^2 - \frac{(x^2+y^2)}{2}\right), \tag{2.6}$$

where κ is a geometric factor and z_0 defines the distance between trap center and the end-cap. To characterize how the ions move in the trap, we set up the following differential equation of motion

$$m\ddot{r}_i + e\vec{\nabla}(\Phi_{\text{dyn}} + \Phi_{\text{stat}}) = 0 \tag{2.7}$$

where $i \in \{x,y,z\}$. At first glance, we would expect the time-dependent part of the force to disappear, when we average over time. However, in an inhomogeneous, periodic field such as the quadrupole field, a small mean force remains, which always acts in the direction of the decreasing field, in this case in the direction of the central axis. For this reason, the ions remain stored in the radial direction under suitable conditions. By applying transformation parameters (also called stability parameters)

$$a_x = \frac{8eU}{mr_0^2\Omega^2} - \frac{4e\kappa U_0}{mz_0^2\Omega^2}, \qquad a_y = -\frac{8eU}{mr_0^2\Omega^2} - \frac{4e\kappa U_0}{mz_0^2\Omega^2}, \qquad a_z = \frac{8\kappa eU_0}{mz_0^2\Omega^2}, \tag{2.8}$$

$$q_x = -q_y = \frac{4eV}{mr_0^2\Omega^2}, \tag{2.9}$$

$$\Omega t = 2\xi, \tag{2.10}$$

we can define Mathieu's differential equation of motion [43]

$$\frac{d^2r_i}{d\xi^2} + (a_i - 2q_i\cdot\cos 2\xi)\cdot r_i = 0. \tag{2.11}$$

From this equation, we get two types of solutions:

- *Stable* trajectory: the ions oscillate with finite amplitude in the x and y directions and cross the quadrupole field in the z direction without hitting the electrodes.
- *Unstable* trajectory: the oscillation amplitude in x- or y- direction grows exponentially, such that the particles are removed from the electrodes.

A particle remains trapped when the Mathieu equation yields a non-divergent solution. An analytical analysis gives the general Mathieu equation in the limit of a small enough q-parameter [32]

$$r_i(t) = r_{0,i}\cos\left(\omega_i t + \phi\right)\left(1 + \frac{q_i}{2}\cos\Omega t\right), \tag{2.12}$$

where ω_i is given by

$$\omega_i = \frac{\beta_i \Omega}{2} \qquad \text{with} \qquad \beta_i = \sqrt{a_i + \frac{q_i^2}{2}}. \tag{2.13}$$

The general Mathieu equation (2.12) is a combination of two superimposed motions:

- *Secular motion*: a slow oscillation with frequency $\omega_i = \frac{\beta_i \Omega}{2}$ and
- *Micromotion*: a fast oscillation at frequency Ω and amplitude $q_i/2$.

Micromotion experienced by an ion when its equlibrium position does not align with the point of minimum potential, also known as the RF-zero line, is called excess micromotion. As micromotion adversely affects the interaction between the ion and the laser field, it is essential to minimize its amplitude in order to maintain high-fidelity quantum control. In the case of a linear chain, micromotion can be effectively minimized by aligning the ion positions along the RF-null line. For multiple ions confined in the trap, at sufficiently low temperatures, the ions form Coulomb crystals. Their equilibrium positions are determined by the balance between the trap's confining potential and the mutual Coulomb repulsion. Depending on the trap anisotropy, these crystals can be one-, two-, or three-dimensional. Small oscillations of ions around these equilibrium positions give rise to collective vibrational modes, which can be described as a set of coupled harmonic oscillators. When the ions are arranged in a linear chain, the RF-null line can still be aligned to minimize micromotion. However, in higher-dimensional crystals, some ions are necessarily displaced from the RF-null, inherently inducing excess micromotion. To mitigate the resulting adverse effects, laser beams are typically applied along directions that are perpendicular to the direction of micromotion, thereby minimizing the coupling between the laser field and the micromotion-induced velocity of the ions [23]. To achieve micromotion in just one direction, the ion crystal is precisely aligned to the orientation of the electrodes.

2.3 SPIN MODELS

An important advantage of extending the system into two spatial dimensions is the ability to explore two-dimensional spin models. These models provide a fundamental framework

for studying interacting many-body quantum systems and offer a tractable setting for both theoretical analysis and numerical simulation. In this work, we focus exclusively on spin-1/2 particles, with basis states $|\uparrow\rangle$ and $|\downarrow\rangle$. Notable examples of such spin models include the Ising model and the XY model, both of which capture essential features of quantum magnetism and collective spin dynamics in lattice systems and are discussed very briefly in the following. For more details and their experimental implementation, see [44, 45].

- **Ising model**: One of the most fundamental spin-1/2 models is the Ising model, originally introduced by E. Ising [46], which describes spin-spin interactions constrained to a single spatial axis. A widely studied variant is the transverse-field Ising model, which incorporates quantum fluctuations by including an external field perpendicular to the interaction axis. The Hamiltonian for N spins in this model is given by:

$$H_{\text{Ising}} = \hbar \sum_{i,j}^{N} J_{ij} \hat{\sigma}_x^i \hat{\sigma}_x^j + B \sum_i \hat{\sigma}_z^i, \tag{2.14}$$

  where $\hat{\sigma}_x^i \hat{\sigma}_x^j$ is a two-body spin-spin coupling operator. The first term represents pairwise spin-spin interactions along the x-axis, characterized by the coupling strength J_{ij}. The sign of the coupling strength determines the nature of the interaction: positive J_{ij} favors parallel spin alignment (ferromagnetic coupling), while negative J_{ij} favors anti-parallel alignment (antiferromagnetic coupling). The second term corresponds to a transverse magnetic field applied along the z-axis, characterized by a field strength B. This field counteracts the spin-spin coupling in the x-direction and drives the spin system toward alignment along the z-axis, thereby inducing spin polarization.

- **XY model**: In the regime of a strong transverse field B, where the field term in the transverse-field Ising Hamiltonian dominates over the spin-spin interaction, the system's effective dynamics can be approximated by the XY model [47]. In this limit, the Hamiltonian takes the form:

$$H_{\text{XY}} = \hbar \sum_{i,j}^{N} J_{ij} (\hat{\sigma}_x^i \hat{\sigma}_x^j + \hat{\sigma}_y^i \hat{\sigma}_y^j). \tag{2.15}$$

  This Hamiltonian describes spin-exchange (or flip-flop) interactions in the x-y plane, whereby an excitation can be coherently transferred between spins. Specifically, an excitation in spin i can be annihilated while simultaneously creating an excitation in spin j, and vice versa. As a result, the total number of spin excitations—also referred to as the total magnetization—is conserved under the XY dynamics, with additional spin flips being energetically suppressed.

3

Atom-Light Interaction

Atom-light interactions play a central role in quantum information science, enabling control over both the electronic and motional states of atomic systems. In this chapter, we examine the foundational aspects of these interactions, with a focus on their relevance to trapped-ion platforms. We begin by analyzing the interaction between laser light and a two-level atomic system (Sec. 3.1), laying the groundwork for understanding coherent control and optical transitions. We then extend this discussion to the case of off-resonant light fields, introducing the AC Stark shift and its implications for qubit manipulation (Sec. 3.2). Particular attention is given to group-II ions, such as $^{40}Ca^{+}$, which are central to our experimental work. Next, we explore spin-motion coupling (Sec. 3.3), an important feature of trapped-ion systems that allows for the implementation of entangling quantum gates. To that end, we introduce the quantum harmonic oscillator model and the concept of coherent motional states in Sec. 3.4. These tools provide the theoretical framework for describing ion motion under laser interaction. We then present two widely used entangling gate schemes based on geometric phases: the Mølmer–Sørensen (MS) gate and the light-shift (LS) gate, see Sec. 3.5. These gates are essential for realizing multi-qubit quantum logic in ion traps. Finally, we address a common limitation of LS gates — decoherence arising from spontaneous light scattering — which imposes fundamental constraints on gate fidelity (Sec. 3.6).

3.1 INTERACTION WITH A TWO-LEVEL SYSTEM

The two-level atom represents the simplest quantum system, yet it exhibits remarkably rich physical behavior, characterized by a Hilbert space spanned by just two basis states. In such a system, a qubit can be encoded provided that several criteria are met, including sufficient lifetimes and coherence times, reliable state readout, and proper state initialization. One prominent example are e.g. Zeeman sublevels of the ground or metastable states. Due to the analogy with the mathematical description of spin states, the two-level system can exist in a superposition of two distinct states, conventionally denoted as "up" and "down".

In this section, we will discuss the interaction of an atom with a light field of the form $E = E_0 \cos(\omega_L t + \Phi_L)$ with frequency ω_L and phase Φ_L. We consider an atom with the two eigenstates

$$\begin{pmatrix} 0 \\ 1 \end{pmatrix} = |\downarrow\rangle = \big|g\big\rangle \text{ and } \begin{pmatrix} 1 \\ 0 \end{pmatrix} = |\uparrow\rangle = |e\rangle\,. \tag{3.1}$$

These states correspond to the ground state and excited state, respectively and are separated by the energy $\hbar\omega_0$. With this, we can write the Hamiltonian of the bare two-level atom

$$H_a = \frac{\hbar\omega_0}{2}\sigma_z, \tag{3.2}$$

where σ_z describes the Pauli operator. By applying a light field for a duration t, populations between the two states $\big|g\big\rangle$ and $|e\rangle$ can be transferred via the interaction energy, given by the following Hamiltonian

$$H_L = \hbar\Omega\sigma_x \cos\big(\omega_L t + \phi_L\big). \tag{3.3}$$

In this framework, the Rabi frequency Ω quantifies the coupling strength between the laser field and the atom by [48]

$$\Omega = \frac{\langle e|\,\mathbf{d}\cdot\mathbf{E}_0\,\big|g\big\rangle}{\hbar}. \tag{3.4}$$

Here, we defined the electric dipole operator $\mathbf{d} = e\mathbf{r}$, where $\mathbf{r}$ represents the position of the electron and e its elementary charge. In this formulation, we assume that the electric dipole moment arises from a single electron only.

For investigating the dynamics of the system, it is convenient to transform the Hamiltonian $H = H_a + H_L$ into the interaction picture. This is achieved by applying the unitary transformation $U = \exp(iH_a t/\hbar)$. To obtain an analytic approximate solution, we use the rotating wave approximation (RWA). The RWA simplifies the system dynamics by neglecting rapidly oscillating terms in the interaction Hamiltonian, which average out over time and have negligible net effect on the evolution. Physically, these counter-rotating terms correspond to processes that simultaneously create or annihilate excitations in both the atom and the field, which are highly non-resonant and thus contribute minimally to the

dynamics. By applying the RWA, the effective Hamiltonian in the interaction picture is reduced to terms oscillating slowly at the detuning frequency $\Delta = \omega_L - \omega_0$, enabling a tractable and accurate description of coherent atom-light interactions under near-resonant driving conditions. Using this approximation, we can write the full Hamiltonian in the interaction picture

$$H_I = \frac{\hbar\Omega}{2}[\sigma_x \cos(\Delta t + \phi_L) + \sigma_y \sin(\Delta t + \phi_L)]. \tag{3.5}$$

By defining the electronic raising and lowering operators

$$\sigma_- = |g\rangle\langle e| \text{ and } \sigma_+ = |e\rangle\langle g|, \tag{3.6}$$

we can rewrite Eq. 3.5 as

$$H_I = \frac{\hbar\Omega}{2}\left[\sigma_+ e^{i(\Delta t+\phi_L)} + \sigma_- e^{i(\Delta t+\phi_L)}\right]. \tag{3.7}$$

In the following, we will look into what happens, when the light field is resonant with the atomic transition frequency and how we can use this for controlling the state of a qubit. On resonance ($\Delta = 0$), the laser light induces coherent oscillations between the populations of the two states $|g\rangle$ and $|e\rangle$, which are also known as Rabi oscillations. The interaction Hamiltonian can be written as

$$H_{I,\Delta=0} = e^{-\frac{iH_I t}{\hbar}} = \begin{pmatrix} \cos\left(\frac{\Omega t}{2}\right) & -ie^{i\phi_L}\sin\left(\frac{\Omega t}{2}\right) \\ -ie^{i\phi_L}\sin\left(\frac{\Omega t}{2}\right) & \cos\left(\frac{\Omega t}{2}\right) \end{pmatrix}. \tag{3.8}$$

In simpler terms, on the Bloch sphere this operation can be thought of as spinning the qubit's state vector around an axis that lies in the xy-plane. The direction of this axis depends on the phase ϕ, while the amount of rotation is set by the angle $\theta = \Omega t$. By shining resonant light on the qubit, we can perform a controlled single-qubit rotation, allowing the qubit state to be moved to any desired point on the Bloch sphere. This single-qubit rotation can be written as [4]

$$R(\theta,\phi) = \begin{pmatrix} \cos\left(\frac{\theta}{2}\right) & -ie^{-i\phi}\sin\left(\frac{\theta}{2}\right) \\ -ie^{i\phi}\sin\left(\frac{\theta}{2}\right) & \cos\left(\frac{\theta}{2}\right) \end{pmatrix}. \tag{3.9}$$

For a phase of $\phi = 0$ and $\phi = \pi/2$, this corresponds to a rotation $R_x(\theta)$ and $R_y(\theta)$, respectively. Applying $R_x(\pi/2)$ to a state that is initially in the ground state $|g\rangle$, this will rotate the state into a superposition of $|g\rangle$ and $|e\rangle$. This operation is commonly referred to as a $\pi/2$-pulse. Respectively, by applying $R_x(\pi)$, the initial state $|g\rangle$ will be shifted to the excited state $|e\rangle$, i.e. it is accordingly called a π-pulse.

3.2 AC STARK SHIFT

In the non-resonant case ($\Delta \neq 0$), the light field induces a shift of the atomic level structure, also known as the AC Stark effect or Autler-Townes effect, discovered by S. Autler and

C. Townes in 1955 [49]. This phenomenon arises when an oscillating electric field - such as that of a laser - is detuned from resonance with an atomic transition, leading to modifications in the absorption and emission spectra. In the following, we first analyze the AC Stark shift within the framework of a two-level system before extending the discussion to more complex atomic structures.

3.2.1 AC STARK SHIFT FOR A TWO-LEVEL SYSTEM

The corresponding Hamiltonian in the interaction picture is derived from Eqs. 3.2 and 3.3 and is given by

$$H_I^{AC} = -\frac{\hbar\Delta}{2}\sigma_z + \frac{\hbar\Omega}{2}\sigma_x. \tag{3.10}$$

To calculate how much the energy of a level is shifted, we can take a look at the eigenvalues $\lambda_\pm = \pm\hbar/2\sqrt{\Omega^2+\Delta^2}$. The energy shift can then be calculated by $\Delta E = \lambda_\pm - \lambda_\pm(\Omega = 0)$. The direction of the AC Stark shift is fundamentally determined by the sign of the detuning $\Delta = \omega_L - \omega_0$. For negative detuning ($\Delta < 0$, red-detuned light), the photon energy is lower than the atomic transition energy, causing a repulsive interaction that increases the energy gap by shifting the excited state up and the ground state down. For positive detuning ($\Delta > 0$, blue-detuned light), the photon energy exceeds the atomic transition energy, leading to an attractive interaction that reduces the energy gap by shifting the levels closer together. A summary is illustrated in Fig. 3.1. The total differential AC Stark shift for a two-level system is given by

$$\Delta E_{AC} = -\frac{\Omega^2}{2\Delta}. \tag{3.11}$$

For large detunings ($\Delta \gg \Omega$), the fast-oscillating terms in the Hamiltonian average out to zero [50]. Under this condition, the system dynamics can be described by the effective Hamiltonian $H_{\text{eff}}^{\text{AC}}$:

$$H_{\text{eff}}^{\text{AC}} = \frac{\hbar\Delta E_{\text{AC}}}{2}\sigma_z. \tag{3.12}$$

The differential AC Stark shift plays a crucial role in the implementation of LS gates, as it enables state-dependent coupling by affecting the two qubit states differently. As shown in Eq. 3.12, this shift can be exploited to realize σ_z gates.

3.2.2 AC STARK SHIFT FOR A REAL ATOM

For a real atom, the calculation of the AC Stark shift is more complex, since many more electronic states are involved, which couple off-resonantly to the laser field. In this context, we investigate the Stark shift arising from light of a specified wavelength, polarization, and propagation direction for a realistic atomic system. This enables a precise characterization of the differential Stark shift between qubit levels, which is crucial for the implementation of quantum gates. The following discussion is based on the paper from B. C. Sawyer and K. R. Brown [33].

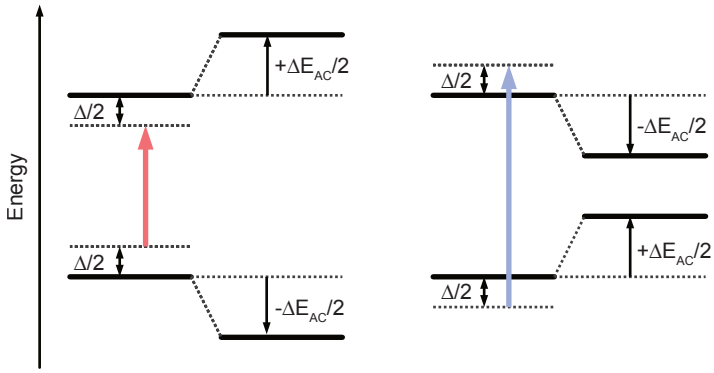

Figure 3.1: **Energy level shifts induced by off-resonant coupling.** For red-detuned light, the levels shift apart. For blue-detuned light, the levels shift closer together.

The AC Stark shift arising from off-resonant coupling by a laser beam with an electric field amplitude E_0 for a state $|i\rangle$ with another state $|k\rangle$ is given by (a detailed derivation of this equation can be found in [51])

$$\Delta E_k = \left(\frac{E_0^2 \hat{\varepsilon}_q^2 \mu_{ki,q}^2}{4\hbar}\right)\left(\frac{1}{\omega_{ki}-\omega_L}+\frac{1}{\omega_{ki}+\omega_L}\right). \tag{3.13}$$

Here, ω_L is the angular frequency of the laser and $\omega_{ki} = (\omega_k - \omega_i)$ is the atomic transition frequency between the states $|i\rangle$ and $|k\rangle$. $\hat{\varepsilon}_q$ denotes the projection of the electric laser field on the quantization axis. The projection $\hat{\varepsilon}_q$ is obtained by constructing the laser polarization vector in the laboratory frame, defined by the laser's propagation direction (θ, ϕ), see Fig. 3.2. Here, θ describes the angle between the **k**-vector and the quantization axis and ϕ the angle between the polarization direction and the plane spanned by the quantization axis and the **k**-vector. The laser polarization vector is then expressed in the spherical basis

$$\mathbf{e}_0 = (0,0,1), \tag{3.14}$$

$$\mathbf{e}_{+1} = \frac{1}{\sqrt{2}}(-1,i,0), \tag{3.15}$$

$$\mathbf{e}_{-1} = -\mathbf{e}_{+1}^*. \tag{3.16}$$

From this the projection follows as

$$\hat{\varepsilon}_q = \mathbf{e}_q^\dagger \cdot \mathbf{e}, \tag{3.17}$$

where **e** is the normalized laser polarization vector.

$\mu_{ki,q}$ is the electric dipole operator given by

$$\mu_{ki,q}^2 = |\langle k|\mu_q|i\rangle|^2 = \frac{3\pi\varepsilon_0\hbar c^3}{\omega_{ki}^3} A_{J_k J_i}(2J_k+1)\begin{pmatrix} J_i & 1 & J_k \\ m_i & q & -m_k \end{pmatrix}^2, \tag{3.18}$$

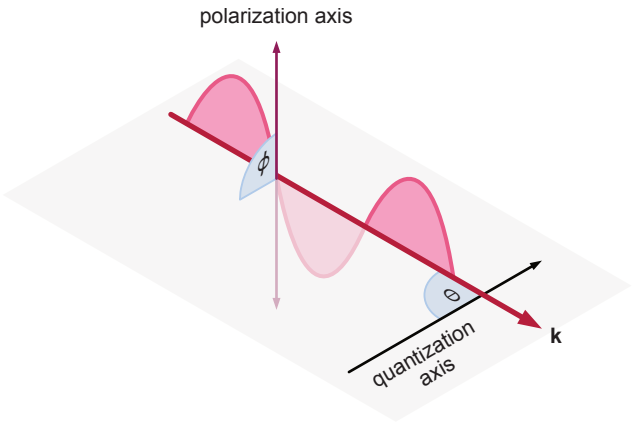

Figure 3.2: **Geometry of the quantization axis and polarization axis**. An exemplary geometry of the quantization axis and the k-vector of the laser is shown. The k-vector has an angle θ towards the quantization axis. ϕ describes the angle between the polarization direction and the plane spanned by the quantization axis and the **k**-vector.

where the matrix elements can be calculated, using the Wigner-Eckart theorem, also known as the $3j$-symbol. We can also relate the $3j$-symbol to Clebsch-Gordan coefficients [52] via

$$\begin{pmatrix} J_i & 1 & J_k \\ m_i & q & -m_k \end{pmatrix} = \frac{(-1)^{J_i-1+m_k}}{\sqrt{2J_k+1}} \langle J_i m_i; 1q | J_k m_k \rangle . \tag{3.19}$$

Hereby, J is the total angular momentum number and m the magnetic quantum number. ε_0 describes the permittivity of free space and $\hbar$ the reduced Planck constant. $A_{J_k J_i}$ is defined by the spontaneous emission rate between an excited state $|k\rangle$ and the initial state $|i\rangle$. The Clebsch-Gordan coefficients and linewidths for all seven transitions in the $^{40}Ca^+$ ion can be extracted from Fig. 3.3. It is evident that the AC Stark shift is primarily dominated by the $S \leftrightarrow P$ and $P \leftrightarrow D$ transitions, due to the significantly stronger dipole coupling associated with these transitions, compared to quadrupole couplings, as quantified by their larger Einstein coefficients.

We extend our discussion to group-2 atomic ions and assume that all intermediate states $|k\rangle$ are sublevels of the $P_{1/2}$ and $P_{3/2}$ states. If we use the relation $E_0^2 = 2I/(\varepsilon_0 c)$, we can rewrite Eq. 3.13 as a function of intensity. By adding up all possible intermediate states, we obtain the total energy shift:

$$\Delta E = \sum_{k,q} \left\{ \left(\frac{I \hat{\varepsilon}_q^2 \mu_{ki,q}^2}{2\varepsilon_0 \hbar c} \right) \left(\frac{1}{\omega_{ki} - \omega_L} + \frac{1}{\omega_{ki} + \omega_L} \right) \right\}. \tag{3.20}$$

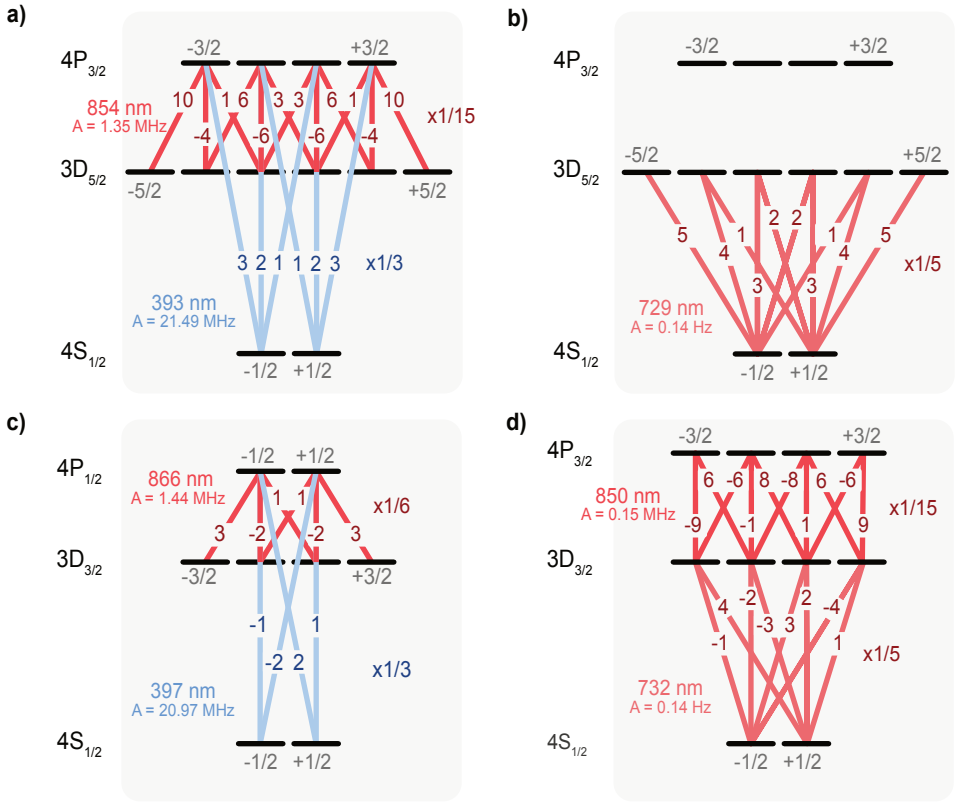

Figure 3.3: **Clebsch-Gordan coefficients for $^{40}Ca^{+}$.** All seven transitions for the $^{40}Ca^{+}$ ion are shown. For simplicity, the Clebsch-Gordan coefficients are shown without taking the square root sign, so the values correspond directly to $|C|^2$. The constant factor for each transition is given alongside, and the linewidth for each transition is also indicated.

3.3 SPIN-MOTION COUPLING

So far, we have limited our discussion on the atom-light interaction to the case, where the atom is held fixed in space. Now, we want to examine the case, where the atom is trapped in a harmonic potential. When an atom is confined in a harmonic potential and illuminated by laser light, the motional states of the oscillator become coupled to the electronic states of the two-level atom, with the oscillator behaving as a linear system and the two-level atom providing the nonlinearity. The atom oscillates at a frequency ω in the harmonic trap, where the position of the atom changes the phase ϕ_L of the incoming light field. This motion causes a Doppler shift, which effectively modulates the laser frequency. Because of this, motional sideband transitions appear at $\omega_0 \pm \omega$, allowing the laser to influence both the atom's internal electronic state and its external motional degrees of freedom at the same time.

For a more general investigation, we have to extend the Hamiltonian described in Sec. 3.1

with the Hamiltonian for the motion in the harmonic potential

$$H = H_a + H_l + H_m \tag{3.21}$$

$$= \frac{\hbar\omega_0}{2}\sigma_z + \hbar\Omega(\sigma_+ + \sigma_-)\cos\left(k\hat{x} - \omega_L t - \phi_L\right) + \hbar\omega\left(a^\dagger a + \frac{1}{2}\right), \tag{3.22}$$

where k is the wave vector of the laser and $\hat{x}$ denotes the position operator. a and $a^\dagger$ represent the creation and annihilation operators (see Eq. 3.31) of the harmonic oscillator mode. Additionally, we define the Lamb-Dicke parameter, which describes the coupling of light to the atom's motion given by

$$\eta = k\sqrt{\frac{\hbar}{2m\nu_{\text{trap}}}}. \tag{3.23}$$

Here, m represents the mass of the atom and ν_{trap} is the frequency of the ion's oscillation in the trapping potential. A Lamb-Dicke parameter $\eta < 1$ indicates that the energy spacing of the harmonic oscillator states exceeds the ion's recoil energy, thereby suppressing transitions that change the ion's motional state. If the motional wave packet x_0 is smaller than the laser wavelength, we enter the Lamb-Dicke regime $\eta^2(2\bar{n}+1) \ll 1$, where $\bar{n}$ is the vibrational quantum number. With this assumption, we can make the following Taylor approximation:

$$e^{i\eta(ae^{-i\omega t} + a^\dagger e^{i\omega t})} = \mathbb{1} + i\eta\left(ae^{-i\omega t} + a^\dagger e^{i\omega t}\right) + \mathcal{O}(\eta^2) \tag{3.24}$$

Using this, we can write the Hamiltonian in the interaction picture [32]

$$H_{\text{int}} = \frac{\hbar\Omega}{2}\left(\sigma_+ e^{-i(\Delta t + \phi_L)}\left[1 + i\eta\left(ae^{-i\omega t} + a^\dagger e^{i\omega t}\right) + \mathcal{O}(\eta^2)\right] + h.c.\right). \tag{3.25}$$

By tuning the laser detuning to either $\Delta = 0$ or $\Delta = \pm\omega$ (see Fig. 3.4), we establish three distinct scenarios that serve as the foundation for numerous quantum operations in trapped-ion experiments.

- **Carrier transition**, $\Delta = 0$: The laser is resonant with the atomic transition, altering only the internal state of the atom. These transitions are of the form $|g,n\rangle \leftrightarrow |e,n\rangle$ with $n = 0, 1, 2, \ldots$. This interaction can be represented by the Hamiltonian

$$H_{\text{carrier}} = \frac{\hbar\Omega}{2}\left(\sigma_+ e^{-i\phi_L} - \sigma_- e^{i\phi_L}\right). \tag{3.26}$$

- **Red sideband (RSB) transition**, $\Delta = -\omega$: The absorption of red-detuned laser light drives transitions between the states $|g,n\rangle \leftrightarrow |e,n-1\rangle$. The corresponding Hamiltonian is given by

$$H_{\text{RSB}} = \frac{i\hbar\Omega}{2}\left(\sigma_+ a e^{-i\phi_L} - \sigma_- a^\dagger e^{i\phi_L}\right), \tag{3.27}$$

  with Rabi frequency $\Omega_{n-1,n} = \eta\sqrt{n}\Omega$.

- **Blue sideband (BSB) transition**, $\Delta = +\omega$: Similarly, the absorption of blue-detuned laser light drives transitions between the states $|g, n\rangle \leftrightarrow |e, n+1\rangle$. The Hamiltonian is then given by

$$H_{\mathrm{BSB}} = \frac{i\hbar\Omega}{2}\left(\sigma_+ a e^{-i\phi_L} - \sigma_- a^\dagger e^{i\phi_L}\right), \tag{3.28}$$

with Rabi frequency $\Omega_{n,n+1} = \eta\sqrt{n+1}\Omega$. This dependence of the coupling strength on the motional state enables measuring the vibrational state populations by driving the BSB transition and monitoring the time-dependent evolution of the ion's excited upper electronic state population.

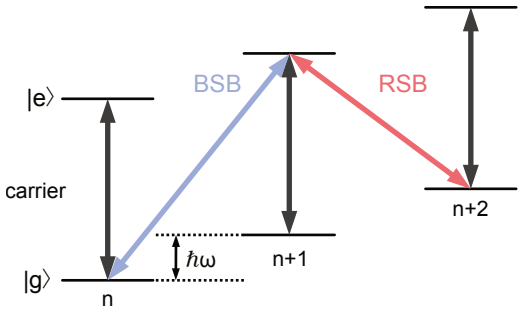

Figure 3.4: **Energy levels in a two-level trapped ion**. The spin–motion states are arranged in a ladder-like structure, where $|g\rangle$ and $|e\rangle$ denote the electronic states and n labels the motional states, spaced by integer multiples of the motional energy $\hbar\omega$. Carrier (car) transitions are shown with black arrows, while blue (BSB) and red (RSB) arrows indicate the associated sideband transitions.

The interaction between the motional and electronic states allows the use of Coulomb forces in an ion crystal to facilitate interactions between ions through the excitation and de-excitation of their collective motion. This mechanism is fundamental to most multi-qubit quantum gates in trapped-ion experiments. The latter requires a state-dependent spin-motion coupling, which can be engineered by applying laser fields with carefully tailored geometries and frequency components, enabling various driving schemes for the electronic and motional states. The specific implementation depends on the chosen gate mechanism and remains an active area of research in trapped-ion quantum information processing.

3.4 THE HARMONIC OSCILLATOR AND COHERENT STATES

Depending on the driving schemes of the motional modes, various states of the harmonic oscillator can be generated. Prominent examples are thermal, Fock or coherent states. For the understanding of the experiments in this work, coherent states are of great importance. This discussion follows the foundational work by R. Glauber [53]. We begin by considering the classical harmonic oscillator: a particle of mass m confined in a one-dimensional quadratic potential described by $V(x_c) = m\omega^2 x_c^2/2$, where x_c denotes the position coordinate and ω is the angular oscillation frequency. As with any

harmonic system, the motion of the oscillator can be represented in phase space, where the state of the system traces a certain trajectory, as shown in Fig. 3.5. This motion can be expressed using the complex variable $\alpha_c(t) = |\alpha_c|e^{i\omega t}$, with $\alpha_c = x_c + i\,p_c$ and momentum coordinate p_c. In the resonant case, the oscillator undergoes a clockwise rotation while its amplitude increases (Fig. 3.5a)). When observed from the perspective of a rotating frame, this motion is equivalent to a straight trajectory in phase space (Fig. 3.5b)). Conversely, in the off-resonant case, the oscillator undergoes a clockwise rotation, accompanied by an increase in amplitude. Notably, in contrast to the resonant scenario, the state reverts to its initial position after a certain time (Fig. 3.5c)). In the rotating frame, this trajectory is depicted as a closed trajectory in phase space (Fig. 3.5d)). The smaller the detuning is, the closer the trajectory approaches an ideal circular shape.

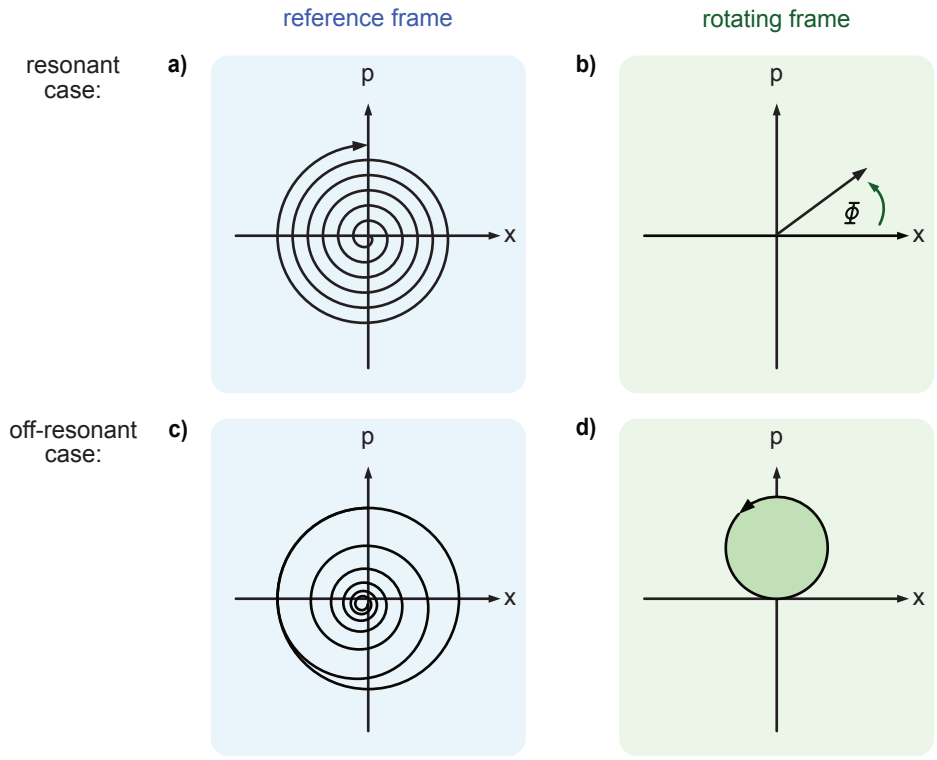

Figure 3.5: **Classical harmonic oscillator dynamics in the reference and rotating frames**. The upper row shows the resonant case, while the lower row illustrates the off-resonant case. In each case, the left panels correspond to the reference frame and the right panels to the rotating frame, which rotates with the eigenfrequency ω. In the resonant case, the oscillator rotates clockwise with increasing amplitude, which appears as a straight trajectory in the rotating frame (**a)**–**b)**). In contrast, under off-resonant driving, the oscillator also rotates clockwise and grows in amplitude, but eventually returns to its initial state, resulting in a closed trajectory in the rotating frame (**c)**–**d)**).

Transitioning to a quantum mechanical description, the classical variables x_c and p_c are replaced by the corresponding quantum operators $\hat{x}$ and $\hat{p}$. Analogous to the classical

case, the total energy of the system is expressed as the sum of kinetic and potential energy, represented by the Hamiltonian

$$H_{\text{osc}} = \frac{\hat{p}^2}{2m} + \frac{1}{2}m\omega^2\hat{x}^2. \tag{3.29}$$

Using the creation and annihilation operators

$$a^\dagger = \sqrt{\frac{m\omega}{2\hbar}}\left(\hat{x} - \frac{i}{m\omega}\hat{p}\right), \tag{3.30}$$

$$a = \sqrt{\frac{m\omega}{2\hbar}}\left(\hat{x} + \frac{i}{m\omega}\hat{p}\right), \tag{3.31}$$

we can rewrite Eq. 3.29, yielding

$$H_{\text{osc}} = \hbar\omega\left(a^\dagger a + \frac{1}{2}\right) = \hbar\left(\hat{N} + \frac{1}{2}\right). \tag{3.32}$$

The eigenstates $|n\rangle$ of the number operator $\hat{N} = a^\dagger a$ are known as Fock states, and the eigenvalues $n \in \mathbb{N}$ indicate the number of phonons in the oscillator. The energy of a given state $|n\rangle$ is increased or decreased by one phonon, respectively, by applying the creation and annihilation operators:

$$a^\dagger|n\rangle = \sqrt{n+1}\,|n+1\rangle\,, \tag{3.33}$$

$$a|n\rangle = \sqrt{n}\,|n-1\rangle\,, \text{ with } a|0\rangle = 0. \tag{3.34}$$

It has been demonstrated that all Fock states $|n\rangle$ can be obtained through the reiterated employment of the creation operator on the ground state

$$|n\rangle = \frac{1}{\sqrt{n!}}(a^\dagger)^n|0\rangle\,. \tag{3.35}$$

A coherent state $|\alpha\rangle$ represents the quantum mechanical counterpart most analogous to a classically excited state of a harmonic oscillator. The following discussion outlines the mechanism by which such a state can be generated through the application of a time-dependent driving force.

Applying a time-dependent external force

$$F(t) = A\sin(\omega_d t + \phi_d) = \frac{A}{2i}\left[e^{i(\omega_d t+\phi_d)} - e^{-i(\omega_d t+\phi_d)}\right] \tag{3.36}$$

with amplitude A, drive frequency ω_d, and phase ϕ_d to the quantum harmonic oscillator, introduces an additional interaction energy described by $H_{\text{int}}(t) = -\hat{x}F(t)$. The total Hamiltonian of the system becomes then $H = H_{\text{osc}} + H_{\text{int}}(t)$. As in the previous analysis, the influence of this time-dependent perturbation can be isolated by transitioning to the interaction picture, using the unitary transformation $U = \exp(-iH_{\text{osc}}t/\hbar)$. In this frame, the interaction Hamiltonian takes the form:

$$H_{\text{int}} = \left(ae^{-i(\delta t+\phi_d)} + a^\dagger e^{+i(\delta t+\phi_d)}\right), \tag{3.37}$$

where $\delta = \omega - \omega_d$ is the detuning between the oscillator frequency and the drive. When the driving frequency is resonant with the natural frequency of the oscillator, i.e., $\omega_d = \omega$ and terms oscillating at the sum frequency are neglected under the rotating wave approximation, the interaction Hamiltonian simplifies to:

$$H_{\text{int}} = \frac{Ax_0}{2i}\left(ae^{i\phi_d} + a^\dagger e^{-i\phi_d}\right). \tag{3.38}$$

By introducing a complex, dimensionless amplitude defined by

$$\alpha = e^{-i\phi_d} Ax_0 t/(2\hbar), \tag{3.39}$$

the resulting unitary time evolution under the interaction Hamiltonian, $U = \exp(-iH_{\text{int}}t/\hbar)$, can be expressed in terms of the displacement operator:

$$D(\alpha) = e^{\alpha a^\dagger - \alpha^* a}. \tag{3.40}$$

When applied to the ground state $|0\rangle$ of the harmonic oscillator, this operator generates a coherent state:

$$|\alpha\rangle = D(\alpha)|0\rangle = \sum_n e^{-|\alpha|^2/2} \frac{\alpha^n}{\sqrt{n!}} |n\rangle. \tag{3.41}$$

This expression reveals that the probability of occupying the n-th Fock state follows a Poisson distribution with mean phonon number $\bar{n} = |\alpha|^2$, as illustrated in Fig. 3.7. Thus, a coherent state can be interpreted as a displaced version of the oscillator's ground state in phase space.

Furthermore, the sequential application of two displacement operators satisfies the composition rule:

$$D(\alpha)D(\beta) = D(\alpha+\beta)e^{\frac{1}{2}(\alpha\beta^* - \alpha^*\beta)} = D(\alpha+\beta)e^{i\,\text{Im}(\alpha\beta^*)}, \tag{3.42}$$

demonstrating that displacements are additive up to a phase factor. This accumulated phase corresponds to the area enclosed in phase space, as illustrated by the shaded region in Fig. 3.6.

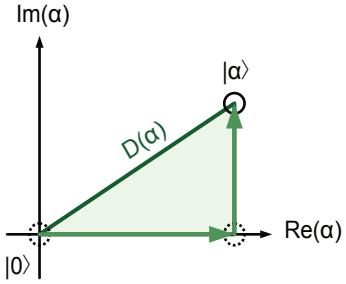

Figure 3.6: **Displacement of the motional ground state**. Phase space representation in a frame co-rotating at frequency ω. The displacement of the motional ground state $|0\rangle$ creates a coherent state $|\alpha\rangle$.

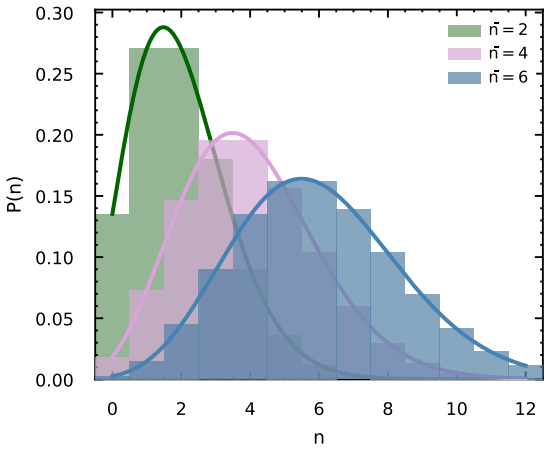

Figure 3.7: **Poissonian distributions in a coherent state**. The Fock space representation is shown for mean phonon numbers 2, 4 and 6. The displacement amplitude scales with the mean phonon number as $\alpha = \sqrt{\bar{n}}$. The solid lines depict a Poissonian fit to the phonon number distribution.

3.5 GEOMETRIC PHASE GATES

One of the fundamental capabilities in the domain of quantum information processing is the ability to entangle the internal states of two or more ions. By applying laser fields, it is possible to coherently excite the motional modes of an ion. Furthermore, the laser parameters can be tuned such that this excitation becomes conditional on the internal spin state of the ion. Through this mechanism of conditional excitation and motional coupling, an entangling gate operation can be implemented. In this section, we will introduce the basic concept of geometric phase gates. Among the various approaches developed, two prominent geometric-phase gates between two qubits are widely used [54]: the LS gate [55–59] and the MS gate [28, 60], which are discussed in the following sections.

Geometric phase gates employ a spin-dependent force to collect spin-dependent phases by driving closed-loop trajectories in motional phase space. Upon completion of these closed paths, the spin and motion become disentangled, ensuring separability. However, the system acquires a phase shift that depends solely on the geometry of the traversed path in phase space. This path-dependent phase is referred to as the (Berry) geometric phase [61].

The analysis presented herein follows the approach outlined in [62]. To investigate the influence of an externally applied, time-dependent driving force on a quantized harmonic oscillator, we begin by expressing the system's Hamiltonian within the interaction picture. In this framework, the oscillator is subject to a classical driving force oscillating at frequency ω, which couples to the oscillator's position operator and introduces an additional time-dependent interaction. The force is defined by

$$F(t) = F_0 \cos\big(\omega t - \phi\big), \tag{3.43}$$

where F_0 and ϕ denote the amplitude and phase of the drive, respectively. The interaction Hamiltonian is given by

$$H_{\text{force}} = -zF(t), \tag{3.44}$$

where z is the position operator of the oscillator. Expressing z in terms of ladder operators,

$$z = z_0(a + a^\dagger), \qquad z_0 = \sqrt{\frac{\hbar}{2m\omega_z}} \tag{3.45}$$

with z_0 the characteristic length of the oscillator's ground state, the Hamiltonian becomes

$$H_{\text{force}} = -z_0 F_0 (a e^{-i\omega_z t} + a^\dagger e^{+i\omega_z t}) \cos\big(\omega t - \phi\big) \tag{3.46}$$

$$= \frac{z_0 F_0}{2} a^\dagger e^{i\phi - i\delta t} + \text{h.c.}, \tag{3.47}$$

where ω_z denotes the harmonic oscillator frequency. We assume a near-resonant driving regime, defined by $\delta := \omega - \omega_z \ll \omega_z$ and accordingly neglect terms that are far off-resonant. We now extend the analysis to a composite system consisting of multiple spin degrees of freedom coupled to a single quantized motional mode through a spin-dependent interaction

$$H_{\text{SDF}} = \frac{i\Omega_D}{2} \Lambda a^\dagger e^{i\phi - i\delta t} + \text{h.c.}, \tag{3.48}$$

where Λ represents a collective spin operator, defined as an appropriate linear combination of Pauli matrices acting on all spin degrees of freedom. Ω_D denotes the coupling Rabi frequency. To evaluate the geometric phase acquired by the system, we compute the propagator associated with this Hamiltonian using the Magnus expansion formalism.

$$U(t) = D(\alpha(t)\Lambda) e^{-i\Phi(t)\Lambda^2} \tag{3.49}$$

$$\alpha(t) = \frac{\Omega_D}{\delta} \sin\left(\frac{\delta t}{2}\right) e^{i\phi - i\delta t/2} \tag{3.50}$$

$$\Phi(t) = \frac{\Omega_D^2}{4\delta^2} (\delta t - \sin \delta t). \tag{3.51}$$

Here, $D(\cdot)$ denotes the displacement operator, defined by $D(\alpha) := \exp\left(\alpha a^\dagger - \alpha^* a\right)$, as already introduced in Sec. 3.4. To elucidate the action of the propagator, it is instructive to expand it in the eigenbasis of the collective spin operator Λ

$$U = \sum_k D(\alpha(t)\lambda) e^{-i\Phi(t)\lambda^2} |\lambda\rangle\langle\lambda|. \tag{3.52}$$

Let $\{\lambda\}$ denote the set of eigenvalues of the collective spin operator Λ. Within this eigenbasis, it becomes evident that the propagator induces displacements of the motional state conditioned on the magnitude and phase of the corresponding spin eigenvalue. Furthermore, each spin eigenstate acquires a geometric phase of the form $\Phi(t)\lambda^2$. In general, if the propagator is applied for an arbitrary time t, the spin and motion become entangled. Consequently, measurement of the spin subsystem alone - effectively tracing over the motion - results in a mixed state of the spin state due to this entanglement. However, if the interaction duration is chosen to be $\tau = 2\pi K/\delta$, where $K \in \mathbb{Z}$, the displacement parameter satisfies $\alpha(\tau) = 0$, ensuring that spin and motion are disentangled at time τ

$$U(\tau) = \sum_\lambda \exp\left(-i\Phi(\tau)\lambda^2\right) |\lambda\rangle\langle\lambda|. \tag{3.53}$$

In this case, a spin-dependent geometric phase has been generated while maintaining separability between the spin and motional degrees of freedom. The applied spin-dependent force drives different components of the spin state along distinct circular trajectories in the motional phase space, as illustrated in Fig. 3.8. The resulting geometric phase Φ acquired by each spin component is proportional to the area enclosed by its respective trajectory [58]

$$\Phi = \mathrm{Im}\left(\int_\gamma \alpha^* d\alpha\right) = \frac{1}{\hbar}\int_A dz dp = \frac{A}{\hbar}, \tag{3.54}$$

where A denotes the enclosed area. This means the acquired phase depends solely on the area A enclosed by the trajectory in phase space, and is independent of both the duration required to complete the trajectory and the velocity at which it is traversed. More precisely, the two-qubit phase is endowed with a dynamic phase component. The dynamic phase is precisely twice the geometric phase with an opposite sign, resulting in a final two-qubit phase that corresponds to the geometric phase [63]. When $\alpha = 0$, corresponding to $\delta\tau = 2\pi K$, the system completes K full loops in phase space. Importantly, the resulting propagator is to the first order independent of the initial motional state of the system.

3.5.1 MØLMER-SØRENSEN GATES

The MS gate, introduced in 1999 by Anders Sørensen and Klaus Mølmer [28], enables robust and high-fidelity two-qubit operations by exploiting the collective motion of ions. Unlike earlier gate schemes - such as the Cirac-Zoller gate [11] - which requires the ion's motion to be cooled to the ground state, the MS gate operates effectively even when the ions are in a thermal state [28]. While motional heating still degrades gate performance, the effect can be mitigated by increasing the detuning from the motional sideband. This requires the ions to traverse more loops in phase space to accumulate the same entangling phase, reducing the sensitivity of the gate to thermal excitations.

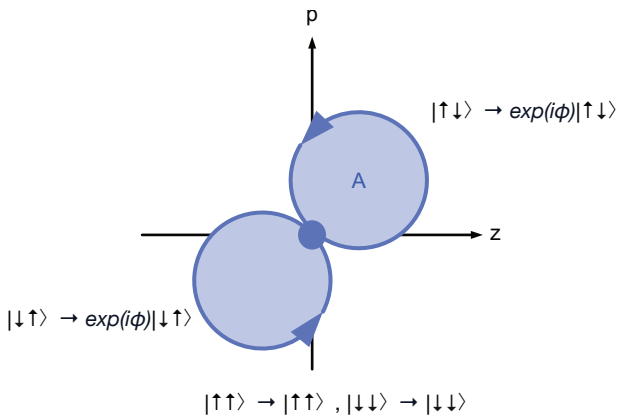

Figure 3.8: **Phase-space representation of the two-ion evolution under a geometric phase gate.** The states $|\uparrow\uparrow\rangle$ and $|\downarrow\downarrow\rangle$ trace closed loops in phase space, each accumulating a geometric phase corresponding to the enclosed area $A/\hbar$

To implement the MS gate, two laser beam tones are detuned from the qubit transition frequency ω_0 to off-resonantly drive the red and blue sidebands of the ions, see Fig. 3.9. The detuning from the qubit transition is $\Delta_{r,b} = \pm(\omega_0 + \delta_{sb})$, where δ_{sb} is an additional detuning from the sidebands. With suitable detunings from the sidebands and Rabi frequencies of the beams, geometric phases are collected. We can write the phases of the red and blue detuned light fields $\phi_{r,b}$ time-dependent $\phi_r = \phi_{r,0} - \delta_{sb}t$ and $\phi_b = \phi_{b,0} + \delta_{sb}t$. The phases of the bichromatic interaction become

$$\phi_+ = \frac{\phi_r + \phi_b - \pi}{2} = \frac{\phi_{r,0} + \phi_{b,0} - \pi}{2} \tag{3.55}$$

and

$$\phi_- = \frac{\phi_r - \phi_b}{2} = \frac{\phi_{r,0} - \phi_{b,0}}{2} - \delta_{sb}t. \tag{3.56}$$

With these definitions, the Hamiltonian of the bichromatic interaction can be written as

$$H_{\text{bic}} = \frac{i\hbar\eta\Omega}{2}(\cos(\phi_+)\sigma_x - \sin(\phi_+)\sigma_y)(\cos(\phi_-)(a^\dagger + a) + i\sin(\phi_-)(a^\dagger - a)), \tag{3.57}$$

where η describes the Lamb-Dicke parameter, $a^\dagger$ and a are the creation and annihilation operators, respectively and Ω denotes the carrier Rabi frequency. When an off-resonant bichromatic laser field is applied, the atomic wave function traces a circular path in phase space and periodically returns to its initial state after an interaction time of $t = 2\pi/\delta_{sb}$. Upon completing this loop, it acquires the geometric phase Φ as previously introduced. A detailed derivation of the Hamiltonian of the interaction can be found in [64]. For our purpose we forego this and rather only give the effective Hamiltonian for a gate acting on two ions:

$$H_{\text{MS}}(\tau) = \frac{\hbar\pi}{4}\text{sign}(\delta_{sb})\sigma_x^{(1)}\sigma_x^{(2)}. \tag{3.58}$$

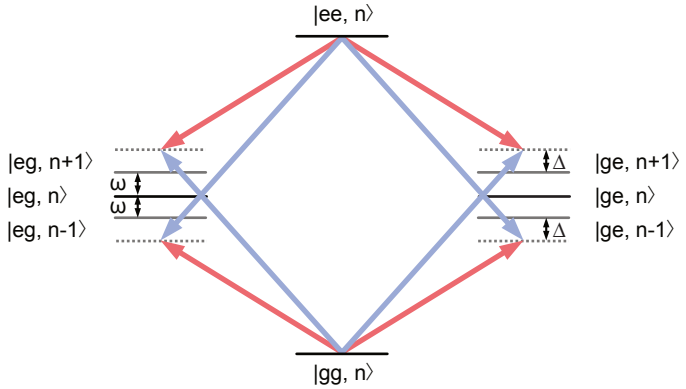

Figure 3.9: **Energy diagram for two ions interacting with a bichromatic laser field**. The ions have a quantized COM vibrational mode of frequency ω. The bichromatic laser field enables a resonant two-photon transition between $|gg,n\rangle$ and $|ee,n\rangle$. There are four different paths, each of them going through an intermediate virtual state separated by Δ from one of the sidebands.

Note that the factor $\pi/4$ corresponds to a maximally entangling MS gate. While MS gates are, in principle, highly effective, their implementation on optical transitions is challenging due to the stringent requirements on laser coherence. This issue is exacerbated in systems with multiple qubit encodings, where a single global beam can induce unwanted differential Stark shifts on other qubits. Furthermore, global-beam implementations are power-intensive, posing difficulties when using narrow-linewidth lasers. Raman-driven MS gates alleviate the sensitivity to laser coherence but require operation near resonance, which increases the rate of spontaneous emission [65].

3.5.2 LIGHT-SHIFT GATES

An alternative approach to implement entangling gates is offered by LS gates. By combining the robustness of Raman-driven schemes with operation at very large detunings from atomic resonances, LS gates can retain favorable coherence properties while strongly suppressing spontanoues decay. With this, low photon scattering errors (2.4×10^{-5} for an intensity of $637\,\mathrm{MW\,m^{-2}}$) can be reached, allowing for the implementation of high-fidelity two-qubit gates [33]. In this scheme, two laser beams intersect to form a standing wave at the positions of the ions. These beams are far detuned from any electronic transitions of the ions, meaning they do not drive direct qubit transitions. Instead, the interaction induces a shift (also called a light-shift) in the ions' internal energy levels via the AC Stark effect, as described above. Due to the fact that the upper $|\uparrow\rangle$ and lower $|\downarrow\rangle$ qubit states couple predominantly to different dipole-allowed transitions (this holds for wavelengths that are not magic wavelengths), the resulting Stark shift is state-dependent, i.e. we obtain a differential AC Stark shift. It is given by $\Delta_\downarrow(\mathbf{r},t)-\Delta_\uparrow(\mathbf{r},t)$, which forms the basis for implementing state-selective interactions in the LS gate. Here, $\Delta_\downarrow(\mathbf{r},t)$ and $\Delta_\uparrow(\mathbf{r},t)$ are the different Stark shifts for the possible states $|\downarrow\rangle$ and $|\uparrow\rangle$, respectively.

To link the ion's spin state with its motion, a small detuning δ between the two beams is

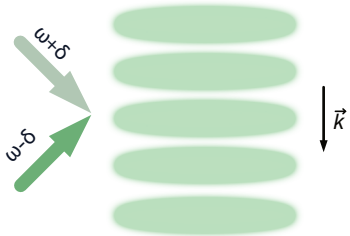

3

Figure 3.10: **Moving standing wave.** The laser beams are intersecting at an angle of 90° with linear polarizations and are detuned from their transition frequency ω by $\pm\delta$. The **k**-vector is aligned with the out-of-plane modes.

introduced, equal to the mode frequency. This generates a moving standing wave and leads to a force exciting the ion's motion, see Fig. 3.10. This so-called optical dipole force (ODF) couples the electronic state with the motion.

The Hamiltonian describing the LS gate is given by [62]

$$H = \sum_j \frac{1}{2}(\Delta_\downarrow |\downarrow_i\rangle\langle\downarrow_j| + \Delta_\uparrow e^{i\delta\phi} |\uparrow_j\rangle\langle\uparrow_j|) e^{-i\omega t} e^{i\phi_0} e^{i\Delta k z_j^0} e^{i\eta_c(a_c + a_c^\dagger)} + \text{h.c.}, \tag{3.59}$$

where we consider a system comprising two ions, with the LS beams aligned such that they couple exclusively to the axial motional modes and uniformly illuminate both ions. The parameter $\delta\phi$ represents the phase-shift between the force experienced by the $|\uparrow\rangle$ and $|\downarrow\rangle$ states. The frequency difference between the two LS beams is denoted by ω, and the index j labels the ions. The parameter ϕ_0 corresponds to the initial phase difference between the LS beams, whose differential wave vector is given by Δk, and z_j^0 denotes the equilibrium position of the j-th ion. In this formulation, only the coupling of the COM (c) axial motional mode is included. Additionally, we allow for spin-dependent AC Stark shift magnitudes, denoted by $\Delta_\uparrow$ and $\Delta_\downarrow$, which act differently on the respective qubit states.

Expanding Eq. 3.59 within the Lamb-Dicke regime yields a simplified form of the interaction Hamiltonian

$$H = \sum_j \frac{i\eta_c}{2}(\Delta_\uparrow |\uparrow_j\rangle\langle\uparrow_j| - \Delta_\downarrow |\downarrow_j\rangle\langle\downarrow_j|) e^{-i\delta t} e^{i\phi_0} e^{i\Delta k z_j^0} a_c^\dagger + \text{h.c.}. \tag{3.60}$$

In this derivation, we assume specific beam polarizations that result in a phase shift $\delta\phi = \pi$. This can be achieved by realizing linear polarization at angles of $\pm 45°$ to the quantization axis along $\hat{z}$. Further, we consider the system to be near-resonant with the COM motional mode of 2.22 MHz in our case.

The resulting Hamiltonian describes a spin-dependent force acting in the σ^z basis. This means, for two ions we have a $\sigma^z\sigma^z$-type interaction. For each spin state, the effective

Rabi frequencies determine both the amplitude and phase of the force, and are given by:

$$\uparrow\uparrow : (1 + e^{i\phi_m})\Delta_\uparrow \tag{3.61}$$

$$\uparrow\downarrow : \Delta_\uparrow - e^{i\phi_m}\Delta_\downarrow \tag{3.62}$$

$$\downarrow\uparrow : e^{i\phi_m}\Delta_\uparrow - \Delta_\downarrow \tag{3.63}$$

$$\downarrow\downarrow : -(1 + e^{i\phi_m})\Delta_\downarrow, \tag{3.64}$$

where $\phi_m = \Delta\mathbf{k}\cdot\mathbf{d}$ is the LS beam phase difference between the ions ($\mathbf{d}$ is the ion separation vector). For $\phi_m = \pi$, the ODF is maximized, resulting in zero net force on $\uparrow\uparrow$ or $\downarrow\downarrow$, while inducing a force of amplitude $\pm(\Delta_\uparrow + \Delta_\downarrow)$ on $\uparrow\downarrow$ and $\downarrow\uparrow$. The ODF drives the two-qubit states $|\uparrow\downarrow\rangle$ and $|\downarrow\uparrow\rangle$ along circular trajectories in phase space, rotating in the same directions but positioned diametrically opposite to one another. This opposite displacement, as shown in Fig. 3.8, arises from the sign reversal of the spin-dependent Stark shift in the Hamiltonian for these states, as evident from Eqs. 3.61 and 3.64. To implement the ideal phase gate, the phase difference between $\uparrow\uparrow$ and $\downarrow\downarrow$ must satisfy $|\Phi(\uparrow\uparrow) - \Phi(\downarrow\downarrow)| = \pi/2$. This condition leads to the requirement [33]

$$\left|\frac{4\pi\eta_c^2\Delta_{0,\Delta}(x_{0,1})\Delta_{0,\Delta}(x_{0,2})}{\delta_k^2}\right| = \frac{\pi}{2}, \tag{3.65}$$

where $\Delta_{0,\Delta}(x_{0,1})$ and $\Delta_{0,\Delta}(x_{0,2})$ denote the differential Stark shifts at the position of the ions. Assuming a gate performed at fixed detuning that traces two loops in phase space over a total duration τ_g, the appropriate detuning is given by $\delta_k = 4\pi/\tau_g$, which yields the gate duration [33]

$$\tau_g = \sqrt{\frac{2\pi^2}{|\eta_c^2\Delta_{0,\Delta}(x_{0,1})\Delta_{0,\Delta}(x_{0,2})|}}. \tag{3.66}$$

3.5.3 PERFORMANCE EVALUATION OF GATES

To assess the performance of quantum gates, we consider the gate fidelity, a metric that quantifies the accuracy of quantum operations. Specifically, it measures the closeness between the actual quantum operation implemented and the ideal target operation it is intended to realize. High gate fidelities indicate that the performed operation closely approximates the desired unitary transformation, thereby reflecting the reliability of the quantum gate under realistic physical conditions. Various techniques exist for characterizing the gate performance, including gate set tomography [66], quantum process tomography [67], and randomized benchmarking [68]. In this work, we employ two methods, using both Bell state fidelity measurements and quantum state tomography, which will be both discussed in the following.

BELL STATE FIDELITY MEASUREMENTS

A simplified approach for measuring gate fidelities is by applying the gate operation to a single input state and assuming that its performance generalizes to other input states [69, 70]. Specifically, we consider the input state $|\downarrow\downarrow\rangle$, for which the ideal output of the gate sequence is the Bell state $\left|\Phi^+\right\rangle = \frac{1}{\sqrt{2}}(|\uparrow\uparrow\rangle + e^{i\Phi}|\downarrow\downarrow\rangle)$. Letting ρ denote the resulting density

matrix after the gate sequence, the fidelity with respect to the target Bell state Φ^+ is given by:

$$\mathscr{F} = \left\langle \Phi^+ \right| \rho \left| \Phi^+ \right\rangle = \frac{1}{2}(\rho_{\uparrow\uparrow,\uparrow\uparrow} + \rho_{\downarrow\downarrow,\downarrow\downarrow}) + \frac{1}{2}\left(e^{i\Phi}\rho_{\uparrow\uparrow,\downarrow\downarrow} + e^{-i\Phi}\rho_{\downarrow\downarrow,\uparrow\uparrow}\right). \tag{3.67}$$

We define $\rho_{ij,kl}$ as the matrix element associated with the transition from $|kl\rangle$ to $\left|ij\right\rangle$. The first term captures the populations of the $|\downarrow\downarrow\rangle$ and $|\uparrow\uparrow\rangle$ states, while the second term accounts for the quantum coherences between them. Consequently, determining the overall fidelity requires measuring both the state populations (first term) and the coherences (second term). The coherences can be extracted by applying an analysis pulse. This pulse consists of a $\pi/2$-pulse applied to the state with a variable phase ϕ, resulting to oscillations in the parity P as a function of ϕ [62]

$$P(\Phi) = p_{\uparrow\uparrow} + p_{\downarrow\downarrow} - p_{\downarrow\uparrow} \tag{3.68}$$

$$\propto A\sin\left(2\phi + \Phi\right). \tag{3.69}$$

Accordingly, the measured amplitude A reflects the coherence term included in Eq. 3.67. Thus, we can calculate the fidelity by measuring the population in the $|\uparrow\uparrow\rangle$ and $|\downarrow\downarrow\rangle$ states, as well as the parity amplitude

$$\mathscr{F} = \frac{p_{\uparrow\uparrow} + p_{\downarrow\downarrow} + A}{2}. \tag{3.70}$$

The phase Φ of the Bell state is disregarded, as the primary interest lies in the degree of entanglement.

QUANTUM STATE TOMOGRAPHY

Another way to estimate the quality of the gate operation is by reconstructing the density matrices of quantum states. The fidelity between a measured state ρ and the ideal target state ρ' is defined as

$$\mathscr{F}(\rho,\rho') = \left(\mathrm{tr}\sqrt{\sqrt{\rho'}\rho\sqrt{\rho'}}\right)^2. \tag{3.71}$$

The following discussion closely follows the work of M. Bock [71].

A general single-qubit density matrix can be written as

$$\rho = \frac{1}{2}\left(\sigma_I + \sum_{i=x,y,z} r_i\sigma_i\right). \tag{3.72}$$

Here, $r_i = \langle\sigma_i\rangle = \mathrm{Tr}(\rho\sigma_i)$ are the components of the Bloch vector, obtained from the expectation values of the Pauli matrices σ_i. To determine these values experimentally, we repeatedly prepare the same quantum state and perform projective measurements in the σ_x, σ_y and σ_z bases. These measurements correspond to six projectors $\Pi_k = (|R\rangle\langle R|, |L\rangle\langle L|, |H\rangle\langle H|, |V\rangle\langle V|, |D\rangle\langle D|, |A\rangle\langle A|)$, which are described as positive-operator

valued measures (POVM). For each projector Π_k, we count detection events N_k and normalize them by the total number of events for a given basis setting N_{basis}. With this we can define relative frequencies f_k:

$$f_k = \frac{N_k}{N_{\text{basis}}} = \frac{N_{\Pi_k}}{N_{\Pi_{R/H/D}} + N_{\Pi_{L/V/A}}}. \tag{3.73}$$

These relative frequencies are used to reconstruct the density matrix.

Rather than directly computing the density matrix from measured expectation values (which can sometimes yield unphysical results), we use maximum-likelihood estimation (MLE). MLE finds the physical density matrix ρ_{est} that fits the measured data best by a maximizing likelihood functional $\mathscr{L}$

$$\rho_{\text{est}} = \arg\max \mathscr{L}(f_k, p_k(\rho)). \tag{3.74}$$

The MLE algorithm that is employed in this work is based on an iterative approach developed by Ježek et al. [72], where the likelihood functional is defined as

$$\mathscr{L}(f_k, p_k(\rho)) = \sum_k f_k \ln\big(p_k\big) - \mu \text{Tr}(\rho). \tag{3.75}$$

Here, $p_k = \text{Tr}(\rho\Pi_k)$ are the probabilities predicted by the model, and μ is a Lagrange multiplier enforcing $\text{Tr}(\rho) = 1$. For finding a solution according to Eq. 3.74, we need to find the maximum from an extremum condition by varying $\mathscr{L}$ with respect to ρ and obtain a set of nonlinear equations:

$$R_{(n)} = \sum_k \frac{f_k}{p_k(\rho_{(n)})}\Pi_k, \tag{3.76}$$

$$\mu_{(n)} = \sqrt{\text{Tr}(R_{(n)}\rho_{(n)}R_{(n)}}, \tag{3.77}$$

$$\rho_{(n+1)} = \mu_{(n)}^{-2} R_{(n)}\rho_{(n)}R_{(n)}. \tag{3.78}$$

We can solve Eq. 3.78 iteratively using Matlab. Since the measured detection counts are subject to statistical fluctuations (typically Poissonian), the reconstructed density matrix and the resulting fidelity also carry uncertainties. To estimate these errors, we use Monte Carlo simulations [73].

3.6 LIGHT SCATTERING

One main source of decoherence in LS gates, is photon scattering. In this discussion, we once again focus on $^{40}Ca^{+}$ ions. To calculate the strength of scattering, we examine the differential scattering cross-section $d\sigma/d\Omega$. The scattering cross-section describes the rate at which energy is extracted from the incoming beam due to scattering into a unit solid angle $d\Omega$ in a specific direction, divided by the rate at which energy in the incident beam passes through a unit area perpendicular to its propagation.

Two distinct scattering processes can be distinguished: elastic and inelastic scattering, as

illustrated in Fig. 3.11. In elastic scattering, the initial and final state are identical, whereas in inelastic scattering, the final internal state differs from the initial one. In the following, we will discuss both, inelastic and elastic photon scattering decoherence, based on the paper from B. C. Sawyer and K. R. Brown [33].

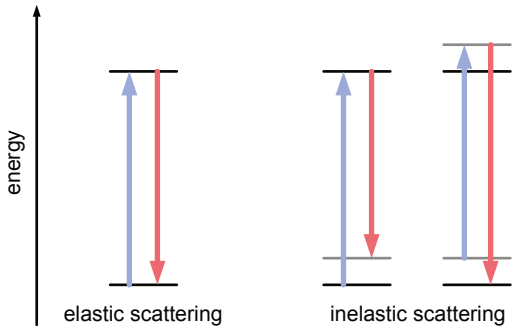

Figure 3.11: **Elastic and inelastic scattering**. On the left: elastic scattering is shown, where the kinetic energy is conserved. On the right: inelastic scattering is shown. There, two processes can be differentiated: Stokes scattering and Anti-Stokes scattering. In both cases the kinetic energy is not conserved.

3.6.1 INELASTIC (RAMAN) SCATTERING

In the case of inelastic scattering, the kinetic energy of the incident photon is not conserved (see Fig. 3.11). We start by discussing the differential scattering cross-section for inelastic scattering [74]

$$\frac{d\sigma^{i\to f}}{d\Omega} = \frac{\omega_L(\omega_L-\omega_{fi})^3}{(4\pi\varepsilon_0)^2\hbar^2c^4}\left|\sum_k\left(\frac{\langle f|\hat{\varepsilon}_s\cdot\vec{\mu}|k\rangle\langle k|\hat{\varepsilon}\cdot\vec{\mu}|i\rangle}{\omega_{ki}-\omega_L}+\frac{\langle f|\hat{\varepsilon}\cdot\vec{\mu}|k\rangle\langle k|\hat{\varepsilon}_s\cdot\vec{\mu}|i\rangle}{\omega_L+\omega_{kf}}\right)\right|^2, \quad (3.79)$$

where $|i\rangle$ is the initial state, $|k\rangle$ are the intermediate excited states (for $^{40}Ca^+$ ions, these are the P states), and $|f\rangle$ is the final state. The angular transition frequencies between the states a and b are represented as $\omega_{ba}=\omega_b-\omega_a$. The electric dipole operator is given by $\vec{\mu}$. $\hat{\varepsilon}$ and $\hat{\varepsilon}_s$ denote the polarization of the laser and of the scattered photon, respectively. The first term of Eq. 3.79 is often times referred to as "counter-rotating" term and the second term as "rotating" term. The counter-rotating term describes off-resonant scattering through the intermediate excited state $|k\rangle$, where the atom ultimately transitions to the final state $|f\rangle$ after spontaneous emission of a photon. In contrast, the rotating term couples the initial state $|i\rangle$ to an intermediate state $|k\rangle$ via spontaneous emission of a photon, eventually transitioning to the final state $|f\rangle$ via the gate laser photon. To calculate the total scattering rate from state $|i\rangle$ to $|f\rangle$ via all intermediate excited states $|k\rangle$, we need to integrate Eq. 3.79 over $d\Omega$ and multiply by the incoming photon flux $I/(\hbar\omega_L)$:

$$\Gamma^{i\to f}=\frac{3\pi c^2 I}{2\hbar}(\omega_L-\omega_{fi})^3\sum_{s=0,\pm1}\left|\sum_k(2J_k+1)\sqrt{\frac{A_{J_kJ_i}A_{J_kJ_f}}{\omega_{ki}^3\omega_{kf}^3}}\left(\frac{\langle f|T_s^1|k\rangle\langle k|\hat{\varepsilon}\cdot\vec{T}|i\rangle}{\omega_{ki}-\omega_L}+\frac{\langle f|\hat{\varepsilon}\cdot\vec{T}|k\rangle\langle k|T_s^1|i\rangle}{\omega_L+\omega_{kf}}\right)\right|^2, \quad (3.80)$$

where we assumed that all intermediate states are sublevels of $P_{1/2}$ and $P_{3/2}$. $S_{1/2}$, $D_{3/2}$ and $D_{5/2}$ can be initial or final states. The matrix elements can be calculated via

$$\langle a| T^1_q |b\rangle = (-1)^{J_a - m_a} (-1)^{L_a+S+J_b+1} \begin{pmatrix} J_a & 1 & J_b \\ -m_a & q & m_b \end{pmatrix}. \tag{3.81}$$

The photon can take the polarization states $q = -1, 0, +1$. The electronic orbital angular momentum of a state $|a\rangle$ is given by L_a. S describes the total electronic spin. In the case of $^{40}Ca^+$ ions, S is 1/2.

For a single ion, we can now define the total inelastic scattering rate, assuming we are in a superposition of the qubit states $|\uparrow\rangle$ and $|\downarrow\rangle$. Furthermore, we assume equal populations in the qubit states $|\uparrow\rangle$ and $|\downarrow\rangle$. The total inelastic scattering rate is then given by

$$\Gamma_{\text{in}} = \frac{1}{2}\left(\sum_{f\neq\uparrow} \Gamma^{\uparrow\to f} + \sum_{f\neq\downarrow} \Gamma^{\downarrow\to f}\right). \tag{3.82}$$

3.6.2 ELASTIC (RAYLEIGH) SCATTERING

For elastic scattering, the kinetic energy and thus the wavelength of the incident light is conserved. This means a photon is scattered by an ion without changing the ion's internal energy levels - i.e., it stays in the same electronic state, but the photon's direction and phase are randomized. When a photon is elastically scattered, the ion's wavefunction acquires a random phase shift.

To analyze the elastic scattering rate we start out again by looking at the scattering amplitude from Eq. 3.79 and employ the result from H. Uys et al. [75]

$$\Gamma_{\text{el}} = \frac{3\pi c^2 I}{4\hbar} \sum_{s=(0,\pm1)} \left(\chi_s^{\uparrow\to\uparrow} - \chi_s^{\downarrow\to\downarrow}\right)^2, \tag{3.83}$$

where

$$\chi_s^{i\to i} = \sum_k (2J_k+1)\cdot A_{J_k J_i} \sqrt{\frac{\omega_L^3}{\omega_{ki}^3}} \left(\frac{\langle i| T^1_s |k\rangle \langle k| \hat{\varepsilon}\cdot\vec{T} |i\rangle}{\omega_{ki}-\omega_L} + \frac{\langle i| \hat{\varepsilon}\cdot\vec{T} |k\rangle \langle k| T^1_s |i\rangle}{\omega_L+\omega_{ki}}\right). \tag{3.84}$$

Again, we assumed equal populations of $|\uparrow\rangle$ and $|\downarrow\rangle$ states.

4

EXPERIMENTAL SETUP

The experimental apparatus was designed to achieve quantum control over large ion crystals composed of up to 100 $^{40}Ca^{+}$ ions. In order to obtain this level of control, a number of prerequisites must be met: first, the generation of a highly controlled trapping environment that effectively isolates the ions from external sources of noise, thereby enabling long coherence times; and second, the ability to exert control over the ions' quantum states through the application of tailored magnetic and laser fields. Together, these capabilities facilitate the implementation of high-fidelity quantum gates. In this chapter, an overview of the ion trap is presented (see Sec. 4.1). Furthermore, the process of how the ions are prepared and manipulated is briefly explained in Sec. 4.2, followed by a discussion of the LS gate laser setup in Sec. 4.3.

4.1 ION TRAP SETUP

Ion confinement in this experiment is achieved using a modified linear Paul trap (see Fig. 2.3, whose design deviates from the conventional configuration). Specifically, the trap features a distinctive electrode arrangement in which the DC blades are split and repositioned vertically, forming a three-layer geometry, see Fig. 4.1. This architecture offers significant experimental advantages: it provides large optical access in the micromotion-free plane, which is required to send laser beams from various directions for efficient laser cooling and quantum state manipulation. In particular, it allows for beam geometries with **k**-vectors perpendicular to the ion crystal's plane for coupling between the electronic state and the out-of-plane motional modes. The interaction with the latter is free of micromotion and thus, the modes of choice to engineer spin-motion and spin-spin coupling. Moreover, a high-NA objective (NA = 0.44) enables site-resolved imaging and individual ion addressing with laser beams.

The RF electrode is positioned at a distance of 400 µm from the center of the ion trap. The DC electrodes are segmented, with the outermost segments functioning as endcap electrodes that provide axial confinement of the ions. To mitigate the influence of RF field components along the axial direction, which arise from discontinuities between the DC electrode segments, additional grounded electrodes are incorporated between the RF and DC electrodes. These ground electrodes serve to suppress spurious axial RF fields, thereby minimizing excess micromotion of the trapped ions in that direction. The trap is operated at an RF drive voltage of approximately 1 kV peak-to-peak and a frequency $\Omega_{\mathrm{rf}} = 2\pi \times 43.22\,\mathrm{MHz}$. These parameters are selected to maintain a Mathieu stability parameter $q \ll 1$, ensuring a low micromotion amplitude. Under these trapping conditions, the Coulomb crystals formed during the experiments described in this thesis exhibit secular oscillation frequencies of approximately 2.22 MHz in the strongly confining direction and several hundred kilohertz in the two more weakly confining directions. More details about the ion trap can be found in [23, 44, 45].

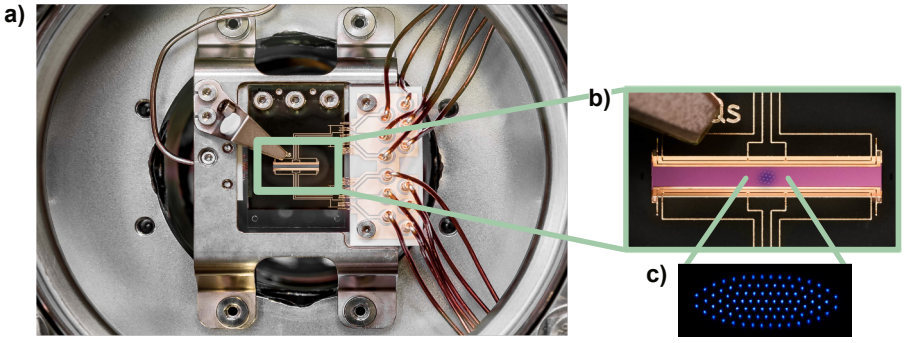

Figure 4.2: **Photographs of the ion trap**. In **a)**, a photograph of the trap assembly as viewed through the front viewport is presented. Visible components include wirebonds connecting the trap electrodes to the DC interposer boards, along with the laser ablation target. **b)** provides a closer view of the ion trap itself. The trapped ion crystal, located at the center of the trap, is shown in **c)**. Image credits: David Jordan, IQOQI.

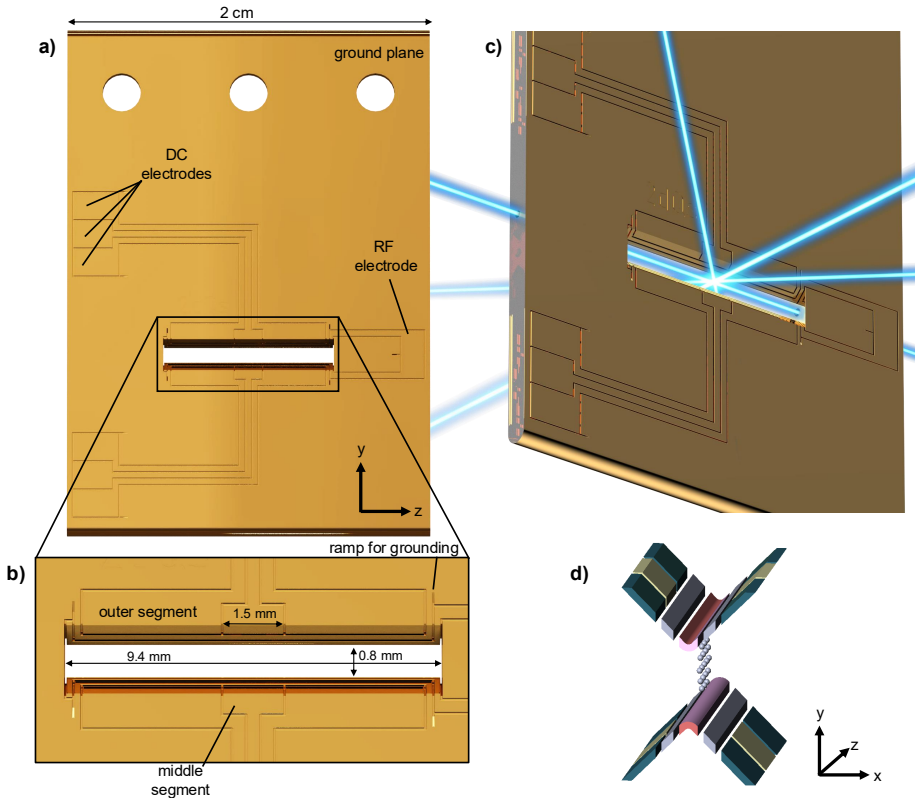

Figure 4.1: **Renderings of the ion trap**. **a)** CAD model of the trap chip viewed from the RF electrode side; the opposite side hosts six DC electrodes in mirror symmetry. **b)** Zoom of the central trapping region. **c)** Laser access in the horizontal (xz) plane: eight directions towards the trap center are available, including the axial direction, where holes in the chip provide optical access. **d)** Schematic of the monolithic trap electrodes and planar ion crystal. Ions are confined in the trap center in the (yz) plane. RF electrodes are shown in pink, DC electrodes in yellow, and endcap electrodes in blue-green; the grey electrodes next to the RF rails are grounded. This configuration enables optical access in the horizontal (xz) plane, perpendicular to micromotion (y), as well as from $\pm 45^\circ$ relative to the crystal plane for spectroscopy beams. Figure adapted from [44].

4.2 ION PREPARATION AND MANIPULATION

Precise manipulation of trapped ions requires a set of lasers, each serving a specific role in the experimental sequence. As illustrated in Fig. 4.3, this includes beams for isotope-selective photoionization, Doppler and EIT cooling, coherent qubit control, entangling interactions via Raman and LS beams, and high-resolution imaging. A 729 nm laser is employed to coherently drive qubit transitions, either in a global or individually addressed manner. In the following, we briefly discuss the procedures for loading the ions into the trap, cooling them, and reading out their quantum state.

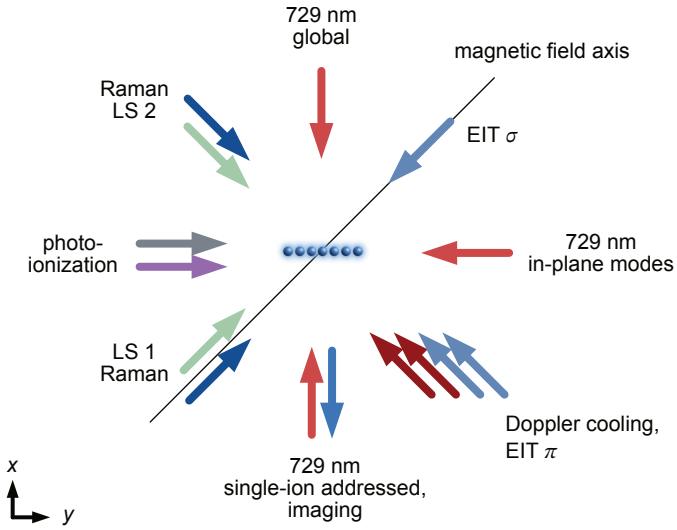

Figure 4.3: **Laser beam and magnetic field geometry from the top**. Multiple laser beams are required for different functionalities. Photoionization beams are used to ionize neutral Ca atoms. Cooling of the ions is achieved through Doppler and EIT cooling beams. Beams for entangling interactions, including both LS and Raman beams, are sent to the ions under an angle of 45° to allow for **k** vectors parallel to the direction of the 729 nm beam. The LS 1 beam is aligned along the magnetic-field axis, while LS 2 is oriented perpendicular to it. In addition, a 729 nm laser is employed to coherently drive the qubit transitions in an addressed or global manner.

- **Ion loading**: To efficiently load ions in the trap, we use laser ablation. As we are working with large Coulomb crystals of up to 100 ions, a fast process is needed to load a large number of ions into the trap. To this end, a pulsed laser at 515 nm ablates neutral atoms from a solid Ca target. Some of the ablated particles fly through the trapping region, where they are ionized and captured by the trapping potential. If the power of the ablation pulse is above a certain threshold, this process directly ionizes the Ca atoms. However, it is desirable to work at lower powers, such that predominantly neutral atoms are ablated, which are then ionized in an isotope-selective way [76].

- **Laser cooling**:
  Doppler cooling: Doppler cooling is implemented on the dipole-allowed $S_{1/2} \leftrightarrow$

$P_{1/2}$ transition using a laser at 397 nm, red-detuned relative to the atomic resonance. Due to the Doppler effect, ions moving towards the incoming laser beam experience a frequency shift that brings the laser frequency closer to the resonance, thereby increasing the likelihood of photon absorption. Following excitation, the ion undergoes spontaneous emission, where the photon is emitted in a 4π angle, i.e. in a random direction. As a result, there is a net momentum reduction along the propagation axis. When averaged over many such absorption-emission cycles, this leads to a net loss of kinetic energy, effectively cooling the ion ensemble. It is worth noting that this principle works equivalently in all three spatial directions, as the trap provides a restoring force along each axis of the trap. For this purpose, the laser field simply needs adequate overlap with all spatial directions. Consequently, a single beam is sufficient to Doppler-cool the ions.

EIT cooling: Electromagnetically-induced transparency (EIT) cooling is an efficient cooling technique for cooling multiple modes near the ground state. The technique works by carefully shaping the absorption spectrum of the cooling transition. By driving a Λ-type three-level system in a way that establishes a coherent superposition of the two ground states, the ion is pumped into a "dark" state that does not couple to the excited level. This quantum-interference effect, which suppresses carrier and BSB excitation, can be engineered such that the remaining absorption is selectively enhanced on the RSB. In practice, EIT cooling is realized by coupling the two Zeeman ground states of the $S_{1/2}$ manifold to the $P_{1/2}$ level, typically using blue-detuned 397 nm light [77].

- **State readout**: Qubit states are detected using fluorescence from the 397 nm cooling laser. A high-numerical-aperture (NA = 0.44) objective collects part of the scattered light, which is then directed to an EMCCD camera. We can discriminate between states via the electron shelving technique [78]: ions fluoresce when they can be excited by the $S_{1/2} \leftrightarrow P_{1/2}$ transition. If the ion is in the metastable $D_{5/2}$ state, it remains dark. This enables reliable distinction between the two qubit basis states. In our system, this can be implemented directly on the optical qubit transition. For the ground-state qubit, the same functionality is achieved via additional shelving pulses with the global 729 nm beam.

4.3 LIGHT-SHIFT GATE SETUP

The LS gates are implemented using a single-mode fiber laser[1] with a wavelength of 532 nm, delivering up to 50 W of optical power and a beam diameter of 0.88 mm. The laser beam is split into two paths using polarizing beam splitters (PBSs). Each arm is independently frequency-, phase- and amplitude-controlled using a single-pass acousto-optical modulator (AOM)[2], which enables the generation of the moving standing wave in the optical domain. The AOMs employed in this setup operate with crystalline quartz, a material chosen for its ability to withstand high optical and RF power levels, both typically on the order of several watts. In general, the optical components have to withstand large

[1] IPG Laser, GLR-532-50-SF
[2] Gooch and Housego, I-M110-2C10B6-3-GH26

optical powers, i.e. high-power polarization optics are required. This involves waveplates with low-loss AR coatings and air gaps between the individual plates[3], as well as PBS with low-loss AR coatings and an epoxy-free optical contact bond between the two prisms, thereby reducing absorption and scattering losses to a minimum[4]. A complete picture of the LS gate setup is shown in Fig. 4.4. The laser light is coupled into two ten meter-long optical fibers[5], which guide the beams to the trapping region. Following fiber outcou-

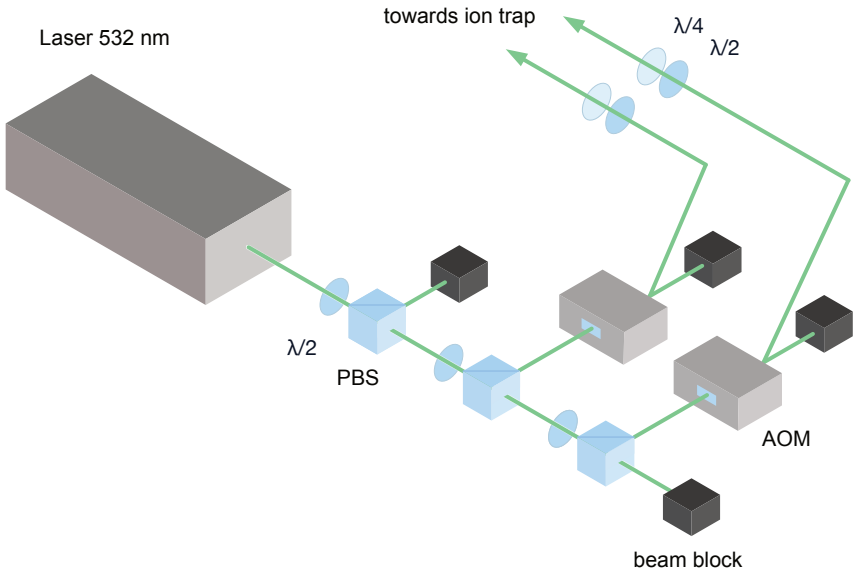

Figure 4.4: **Experimental setup of the 532 nm laser**. The beam is splitted into two arms using polarizing beam splitters (PBS). Each path is precisely frequency, amplitude and phase controlled with an individual single-pass AOM, allowing to generate a moving standing wave. Further, the polarization of the laser light can be controlled accurately with half and quarter waveplates. Finally, the two beams are then sent through optical fibers to the ion trap.

pling, piezo-actuated mirror mounts are used to achieve precise alignment of the beams. The beams are directed onto the crystal at an angle of 45° relative to the crystal plane, resulting in a k-vector that is perpendicular to the crystal plane, as shown in Fig. 4.3 and 4.5. To generate a moving standing wave that selectively couples to the out-of-plane motional modes of the ion crystal, a configuration is employed in which one node of the standing wave intersects the ion crystal, as illustrated in Fig. 4.5. This geometry facilitates alignment and ensures efficient coupling to the desired motional modes.

Linearly polarized light with vertical orientation is used to produce the moving standing wave. This polarization is chosen to minimize differential Stark-shift fluctuations of the ground-state qubit, which would otherwise reduce coherence, as discussed previously. Furthermore, a vertical orientation is chosen to generate only an intensity gradient rather

[3] Bernhard Halle Nachfl. GmbH, RZQ 2.10L.0532 and RZQ 4.10L.0532
[4] Thorlabs, PBS12-532-HP
[5] Thorlabs, P3-488PM-FC-10

than a polarization gradient. Specifically, the use of circularly polarized light would induce differential AC Stark shifts between the Zeeman sublevels of the ground state, resulting in an unwanted phase accumulation by the qubit. Furthermore, fluctuations in laser intensity would translate into phase noise, thereby introducing decoherence. To eliminate these effects and effectively store information in the ground state, linearly polarized beams are exclusively employed, using Glan-laser polarizers[6] to suppress the orthogonal polarization component. The viewport used to guide the LS 1 beam onto the ion trap exhibits a relatively high reflectivity ($\approx 10\,\%$) for vertically polarized light. This reflection imposes a limitation on the maximum usable laser power, as the reflected beam is directed toward the imaging objective, where it can cause undesired effects.

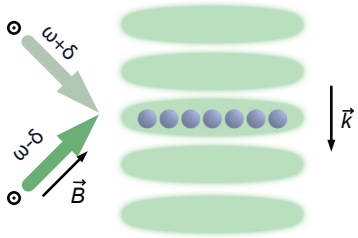

Figure 4.5: **Moving standing wave configuration**. The two beams have an angle of 90° relative to each other and vertical polarization. The beams are aligned such that the k-vector of the moving standing wave is perpendicular to the crystal. With this, we can couple to the out-of-plane modes. The magnetic field is pointing along one of the LS beams.

To maintain a stable relative phase between the resulting beams, the optical setup is designed for interferometric stability. Phase noise in an interferometer generally arises from fluctuations in wavelength of the light source and is affected by the optical path length difference between its arms. Minimizing this path length difference therefore helps reduce phase instability. In the implemented configuration, the geometric arrangement of the optical components limits the optical path length difference to less than 2 cm.

As already shown in Fig. 4.3, the LS beams are spatially overlapped with the Raman beams. This configuration facilitates rough alignment of the LS beams onto the ion crystal. Fine alignment is performed using piezo-actuated mirror mounts.

[6] Thorlabs, GLB10-405

5

LIGHT-SHIFT GATES

This chapter presents an experimental investigation of the implementation of LS gates in a 2D trapped-ion quantum simulator. The analysis begins with simulations (Sec. 5.1) of two parameters governing the gate performance: the AC Stark shift and the photon scattering rate. Subsequently, we extend these simulations to evaluate the gate duration and associated errors. Sec. 5.2 focuses on the experimental characterization of AC Stark shifts and compares the results with theoretical predictions from the simulations mentioned above. In Sec. 5.3, we turn to the characterization of the ODF for different initial electronic states, providing insight into the displacement amplitude. Finally, Sec. 5.4 presents experimental demonstrations of the LS gate implementation in both a two-ion crystal and a ten-ion crystal configuration.

5.1 SIMULATIONS

To assess the performance of the experiment and the agreement of the results with theoretical predictions, it is interesting to perform simulations of the AC Stark shift and scattering rate as well as the expected gate duration based on analytic equations from an atomic physics model. The simulations were conducted following the methodology outlined in the paper of Sawyer and Brown [33].

The simulation results presented in the following figures were obtained using parameters that closely match those of the experimental measurements. All calculations are done for the optical qubit transition $S_{1/2}, m_j = -1/2 \leftrightarrow D_{5/2}, m_j = -1/2$, as this transition exhibits minimal sensitivity to magnetic field fluctuations. Implementing the LS gates requires two non co-propagating beams with a finite k-vector difference, which in our setup addresses the out-of-plane mode whose k-vector is perpendicular to the crystal plane. The geometry is shown in Fig. 5.1. All beams are assumed to be Gaussian beams with a waist of 47.9(2) µm and an optical power of 325 mW, which is the arithmetic mean of the power in the two LS beams. The geometry of the two laser beams is defined by the two angles θ and ϕ, as shown in Fig. 5.1. The angle θ specifies the orientation between the wave vector **k** and the magnetic field **B**, where $\theta = 0°$ corresponds to LS 1 and $\theta = 90°$ to LS 2. The polarization angle ϕ describes the orientation of the electric field relative to the k–B plane and takes values $\phi \in \{0, \pi\}$ in this setup. When **k** is parallel to **B** ($\theta = 0°$), the k–B plane is undefined, but a reference plane spanned by k and B is introduced for consistency. The laser light is linearly polarized. Coupling between electronic states and motion is throughout the measurements mediated by the COM motional mode in out-of-plane direction with a mode frequency of approximately 2.222 MHz. With this mode frequency and a wavelength of 532 nm, the Lamb-Dicke parameter is given by $\eta = 0.089$. In a configuration where the two beams intersect at an angle of 90°, the resulting **k**-vector is given by $\mathbf{k} = \frac{1}{\sqrt{2}} \cdot \frac{2\pi}{\lambda}$.

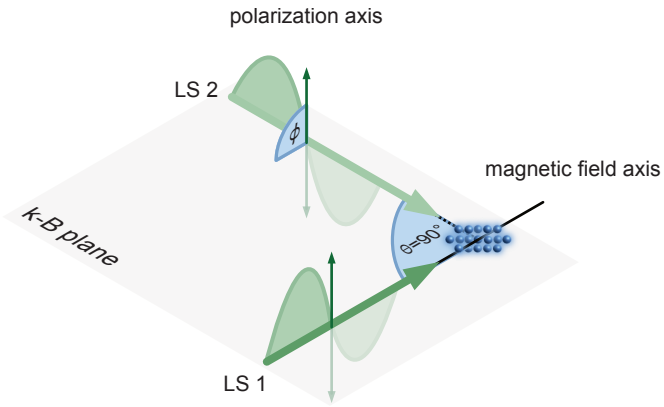

Figure 5.1: **Laser beam geomtry**. The geometry of the two laser beams is characterized by the angles θ and ϕ. The angle θ defines the orientation between the wave vector **k** and the magnetic field **B**, with $\theta = 0°$ corresponding to LS 1 and $\theta = 90°$ to LS 2. The polarization angle ϕ is the angle between the electric field vector and the k–B plane, taking values $\phi \in \{0, \pi\}$.

5.1.1 AC STARK SHIFT AND SCATTERING RATE

The differential AC Stark shift of the qubit states, induced by the gate laser beams, constitutes the primary parameter governing the gate operation. This shift arises mainly from electric dipole transitions between the S and P states, as well as the D and P states, as discussed in Sec. 3.2 and illustrated in Fig. 3.3. The AC Stark shift is calculated using Eq. 3.20, while the total scattering rate is obtained by summing the contributions from inelastic and elastic processes, given by Eqs. 3.82 and 3.83, respectively:

$$\Gamma_{\text{scatt}} = \sum_{j=1}^{N} (\Gamma_{\text{el}} + \Gamma_{\text{in}}), \tag{5.1}$$

where N is the number of ions.

For the realization of high-fidelity gate operations, it is desirable to achieve a large differential AC Stark shift while maintaining a low photon scattering rate, thereby minimizing gate errors. Consequently, operating at laser wavelengths far detuned from the dipole transition is advantageous, provided that sufficiently high laser intensities are available to produce a significant Stark shift. For systems with many levels and large detunings, detailed atomic-structure calculations are worthwhile for identifying optimal laser wavelengths. The result of such a calculation is shown in Fig. 5.2, the simulated differential AC Stark shift (blue curve) and the total scattering rate (green curve) for a single ion interacting with a single laser beam is illustrated as a function of wavelength over the range of 250 nm to 2000 nm. The AC Stark shift displays pronounced resonant features near the dipole transitions at 397 nm, 393 nm and 854 nm. A magic wavelength is observed at 928 nm, where the differential Stark shift between the qubit states vanishes. This occurs because, at this wavelength, the absolute Stark shifts of the $S_{1/2}$ and $D_{5/2}$ states are equal. For wavelengths longer than this value, the Stark shift approaches a plateau due to contributions from counter-rotating terms. The photon scattering rate is large in the vicinity of the resonances and decreases monotonically with increasing detuning. According to Eq. 3.11, the AC Stark shift for wavelengths close to the dipole transitions exhibits an inverse linear dependence on the detuning of the resonant transition, following the relation $\Delta E \propto 1/\Delta$. In contrast, the scattering rate, as derived from Eqs. 3.80 and 3.84, scales with the inverse square of the detuning, i.e., $\Gamma_{\text{scatt}} \propto 1/\Delta^2$; this difference in scaling arises because the Stark shift is a coherent, virtual effect, whereas scattering requires real excitations to the excited state. Therefore, for a fixed laser intensity, increasing the detuning results in a linear reduction of the Stark shift but a more rapid, quadratic suppression of the scattering rate. Consequently, significant Stark shifts can be induced while minimizing incoherent scattering by employing high-intensity laser beams that are far-detuned from resonance. Thus, a good point is between the red and blue transition. The specific wavelength used in the experiment, 532 nm, is indicated by the black vertical line. Notably, at this wavelength, the scattering rate approaches a minimum, making it a favorable choice for gate implementation. Additionally, this wavelength is advantageous from a practical perspective, as high-power laser sources at 532 nm are commercially available and widely used in optical laboratories. At the chosen wavelength of 532 nm, the simulations yield an AC Stark shift of 69.5 kHz and a total scattering rate of 1.5×10^{-2} Hz. Considering the decay rate of the $D_{5/2}$ level, which is $2\pi \times 0.1363$ Hz, it

becomes evident that the dominant limitation on gate fidelity arises from spontaneous decay of the metastable D state rather than from photon scattering. One might ask why not operate closer to the atomic transitions to achieve a larger Stark shift, which would result in faster gates at the cost of increased scattering. However, lasers significantly detuned from 532 nm are considerably more expensive, less powerful, and less robust. In big ion crystals the gate speed is ultimately limited by the coupling to nearby motional modes. For practical gate speeds on the order of 150 µs, the Stark shift achievable at 532 nm is sufficient.

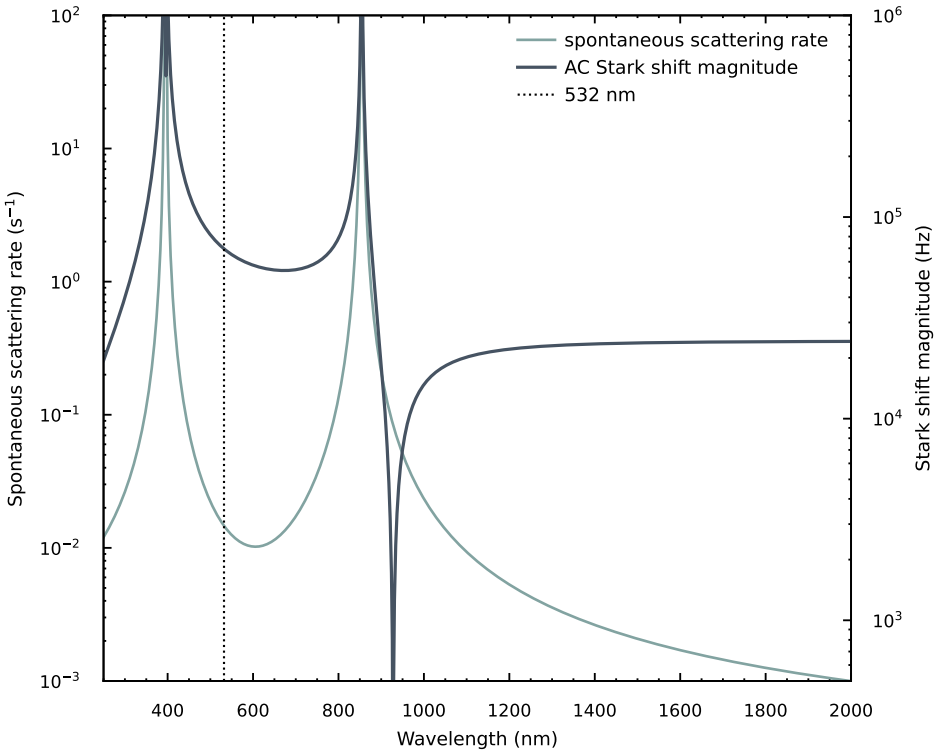

Figure 5.2: **Simulation of AC Stark shift and the spontaneous scattering rate.** The simulation considers a single ion, located at the center of a single Gaussian beam with a power of 325 mW and a beam waist of 47.9(2) µm. The chosen qubit transition is $\Delta m = 0$. The resulting AC Stark shift is depicted in dark blue, while the spontaneous scattering rate is shown in light blue. The operating wavelength of 532 nm used in the experimental setup is indicated by a dashed black line

5.1.2 GATE DURATION AND GATE ERRORS

With this understanding, we can now determine the gate duration, using Eq. 3.66. The gate error due to photon scattering is the product of the scattering rate and the gate duration τ_g and consequently calculated as [33]

$$\epsilon_{\text{scatt}} = \Gamma^{(2)}_{\text{scatt}} \cdot \tau_g, \tag{5.2}$$

where $\Gamma^{(2)}_{\text{scatt}}$ denotes the two-ion photon scattering rate given by Eq. 3.80 and 3.84

$$\Gamma^{(N)}_{\text{scatt}} = \sum_{j=1}^{N} (\Gamma_{\text{el}} + \Gamma_{\text{in}}), \tag{5.3}$$

where N is the number of ions. As mentioned above, apart from photon scattering due to the gate laser the qubit lifetime, given by the lifetime of the D level is an additional error source. Thus, the total decoherence rate is given by

$$\Gamma^{(N)}_{\text{dec}} = \sum_{j=1}^{N} \left(\Gamma_{\text{el}} + \Gamma_{\text{in}} + \frac{1}{2} A_D \right), \tag{5.4}$$

where A_D is the spontaneous decay rate of the D level and N is the number of ions. From this, the fundamental error for two ions can be defined as [33]

$$\epsilon_{\text{fund}} = \Gamma^{(2)}_{\text{dec}} \cdot \tau_g. \tag{5.5}$$

In Fig. 5.3, the gate duration and gate errors are shown for a two-ion crystal (a)) and for a 91-ion crystal (b)), respectively. It is important to note that, for a fixed wavelength, the photon-scattering induced decoherence rate scales linearly with the laser intensity, whereas the gate duration exhibits an inverse dependence on intensity. Consequently, in regimes where decoherence due to D-state spontaneous decay is negligible, the intrinsic two-qubit gate error becomes effectively independent of laser intensity. Although gate speeds increase rapidly near the S–P and D–P resonant transitions, the associated photon scattering errors grow more rapidly, leading to minimum-error operating points that are found at comparatively large detunings from these resonances. Furthermore, magic wavelengths, where the differential Stark shift is zero, are also unsuitable due to divergent gate times.

Based on Fig. 5.3a), one might initially consider a wavelength of 420 nm to be optimal, as it corresponds to a relatively short gate duration and exhibits a local minimum in the fundamental error. However, the motional mode structure, with the nearest mode located 30 kHz away from the COM mode, imposes experimental constraints on the accessible gate durations. Since the gate duration scales approximately as the inverse of the detuning, the achievable gate time is $1/\Delta \approx 33\,\mu\text{s}$. The contributions from neighboring modes can be adiabatically eliminated by extending the pulse duration. Consequently, the practical lower limit for the gate duration is on the order of 150 µs. Taking this constraint into

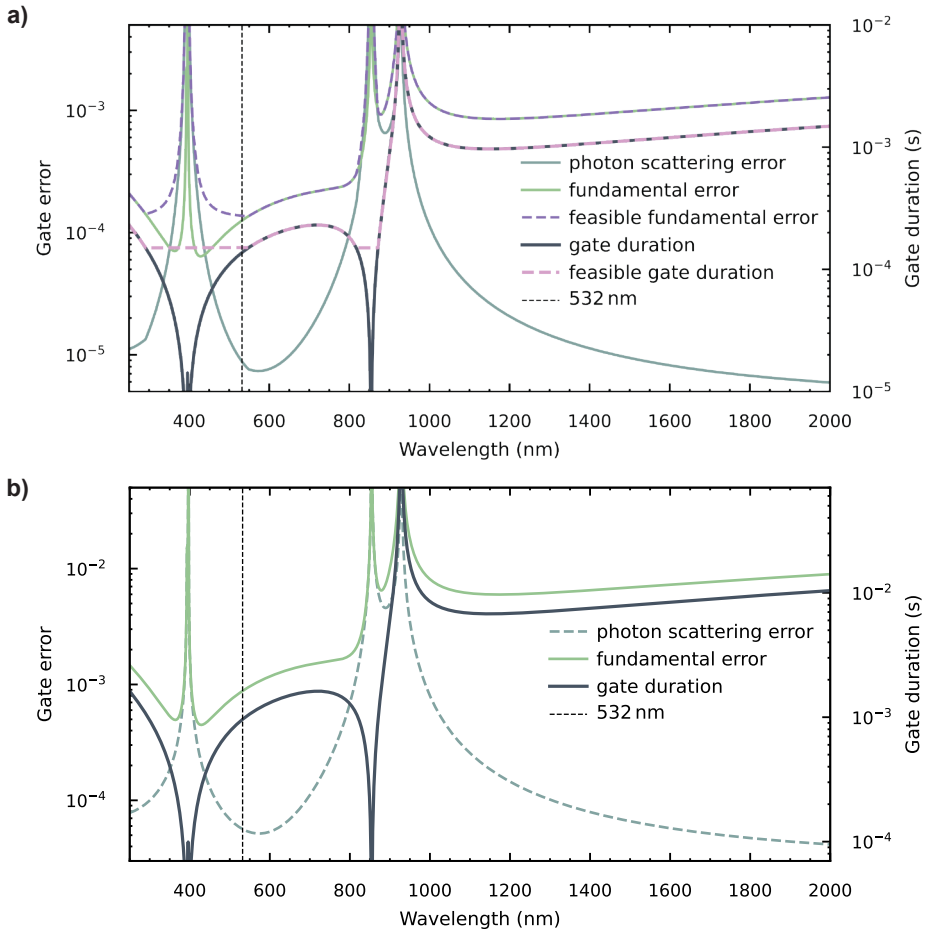

Figure 5.3: **Gate duration simulation**. In this simulation, the ions are assumed to be confined within a harmonic potential characterized by a radial trapping frequency of 2.222 MHz. At the center of the potential, two laser beams intersect to form a moving standing wave. Each beam has a power of 325 mW and a beam waist of 47.9(2) µm. The simulated gate duration is depicted in blue. The calculated fundamental error is shown in green and the photon scattering error in light blue. In **a)**, the gate duration and errors are simulated for a two-ion crystal. The dashed lines in the plot show the experimental feasible gate durations and fundamental errors, where we limited the gate duration to 150 µs. In **b)**, the gate duration and errors are simulated for a 91-ion crystal.

account, a wavelength of 532 nm emerges as a more suitable choice for experimental implementation. At this wavelength, the simulation results indicate a gate duration of 142.6 µs. In this context, this corresponds to the SD and DS states being coupled to the motion, executing closed trajectories in phase space, and thereby acquiring the intended geometric phase. The estimated photon scattering error is 8.4×10^{-6}, while the fundamental gate error is found to be 1.3×10^{-4}. The results clearly indicate that the fundamental gate error is dominated by spontaneous decay of the D level. However, this error limit is extremely low, implying that high-fidelity gates are achievable; an error of 10^{-4} is comparable to the best gates demonstrated to date [34].

To compare the gate performance for larger ion crystals, the gate duration and corresponding errors were simulated for a 91-ion crystal, as shown in Fig. 5.3b). For crystals with more than two ions, the gate duration changes due to the modified Lamb–Dicke parameter, which scales as

$$\eta_N = \frac{k_\Delta}{\sqrt{N}} \sqrt{\frac{\hbar}{2m\nu_{\text{trap}}}}, \tag{5.6}$$

where N is the number of ions, m the mass of the ion, $k_\Delta = k_1 - k_2$ the difference k-vector between the two LS beams and ν_{trap} the trap frequency. The remaining parameters required for evaluating the gate duration from Eq. 3.66 are held fixed. The simulation yields a gate duration of 962.0 µs at a wavelength of 532 nm, using the same input parameters as in the two-ion case. The photon-scattering error is 5.6×10^{-5} and the fundamental error 8.8×10^{-4}. Achieving the same gate duration of 142.6 µs, as obtained for the two-ion crystal, would require increasing the beam power to approximately 2.3 W. This demonstrates that implementing the gate in larger ion crystals becomes increasingly power-intensive.

5.2 AC STARK SHIFTS

Following the theoretical discussion of the AC Stark shift, we now turn to the analysis of the experimental results. The investigation begins with a measurement of the beam waist of the LS beams. These are inferred from Stark shifts observed in a site-dependent 91-ion crystal with known crystal size. Subsequently, AC Stark shifts are measured for a range of optical transitions and between different Zeeman sublevels. In detail, we investigate first transitions between the ground state $S_{1/2}$ and the metastable $D_{5/2}$ states; next, by evaluating the Stark shift within the $D_{5/2}$ manifold itself; and finally, by determining the Stark shift of the ground state.

5.2.1 BEAM SIZE

To accurately compare the simulations with experimental data, we had to input the beam size at the position of the ion crystal into the simulation. This is determined by measuring the differential Stark shift induced by the LS beam on a large crystal. Large crystals have the advantage of possessing a clearly resolved intensity profile. The beams are aligned by centering the intensity maximum on the crystal. A 91-ion crystal is employed for this purpose, as it represents a particularly stable configuration. The corresponding pulse sequence for the AC Stark shift measurement is illustrated in Fig. 5.4a).

To measure the Stark shift with a decent precision of approximately 30 Hz we employ Ramsey-type spectroscopy, which utilizes the 729 nm laser for coherent manipulation of the optical qubit (S to D) as well as the LS laser at 532 nm to induce the Stark shift. Ramsey spectroscopy has the advantage that the Stark shift can be directly measured, by illuminating the ion with the LS laser and simultaneously determining the shift via 729 nm Ramsey spectroscopy. However, this method is not very precise and requires substantial calibration, as the laser frequency must be scanned over a wide range. A more accurate approach is to use a Ramsey sequence, where the LS laser induces a phase shift on a superposition state, which is created using the 729 nm laser [79]. By scanning the Ramsey evolution time and fitting the resulting oscillation frequency, the Stark shift can be measured very precisely with minimal calibration effort. The sequence works as follows: it begins with a $\pi/2$ pulse with phase 0° on the 729 nm carrier transition, corresponding to a rotation around the x-axis. This operation coherently transfers populations from the ground state $S_{1/2}$ into an equal superposition of $S_{1/2}$ and $D_{5/2}$

$$|\psi_1\rangle = \frac{1}{\sqrt{2}}(|S\rangle + |D\rangle). \tag{5.7}$$

During the following free-evolution period of duration T, the ion is exposed to the 532 nm laser, which induces a differential AC Stark shift between the two qubit states. Since the Stark shift for both qubit states are different, we define the accumulated phases during the pulse of duration T as $\phi_S = T \cdot \Delta_S$ and $\phi_D = T \cdot \Delta_D$. The resulting state can be written as

$$|\psi_2\rangle = \frac{1}{\sqrt{2}}(e^{-i\phi_S}|S\rangle + i e^{-i\phi_D}|D\rangle). \tag{5.8}$$

Here, the Stark-induced phase accumulation $\Delta\phi$ encodes the differential frequency shift that is to be measured. To mitigate the effects of laser or qubit coherence drift and residual Stark shifts, a spin-echo π pulse with a phase of 90° is applied using the 729 nm laser. This corresponds to a rotation about the y-axis of the Bloch sphere, inverting the populations of $S_{1/2}$ and $D_{5/2}$. Although the spin-echo sequence is not strictly necessary for measurements involving a single LS beam, it is included here to ensure robustness against such slowly varying errors. Following a second interval of free evolution of duration T, a final $\pi/2$ pulse with a phase of 180°, corresponding to a rotation around the $-x$-axis, concludes the sequence. This pulse projects the accumulated phase ϕ onto a population difference and yielding the state

$$|\psi_3\rangle = \frac{1}{2}e^{-i\phi_S}\left[(1 - e^{-i\Delta\phi})|S\rangle + i(1 + e^{-i\Delta\phi})|D\rangle\right]. \tag{5.9}$$

At last, $|\psi_3\rangle$ is projected by measuring the probability of finding the ion in the D state, which is given by

$$P_D = \frac{1}{2}[1 + \cos(\Delta\phi)]. \tag{5.10}$$

State readout is performed via fluorescence detection at 397 nm using an EMCCD camera. This technique is used throughout this thesis for various measurements with similar arguments if compared to other methods.

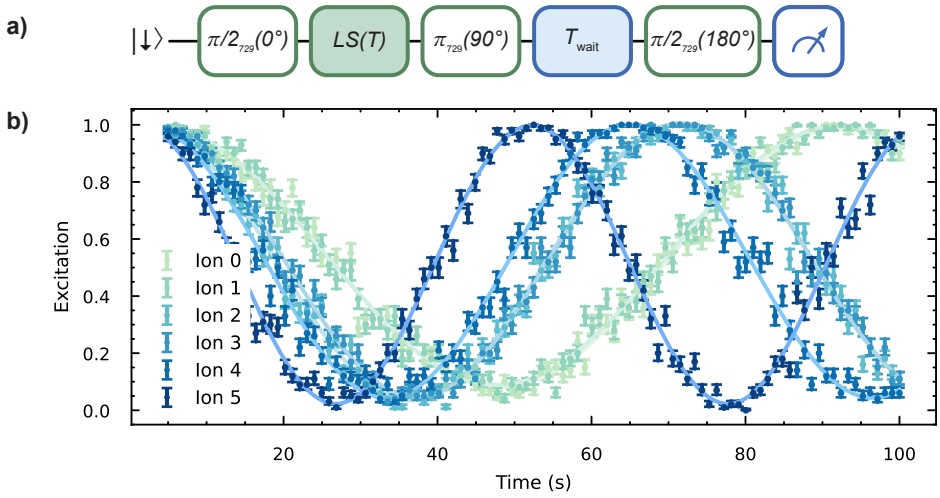

Figure 5.4: **Pulse sequence and corresponding Rabi fringes illustrating the differential Stark shift of the SD transition.**. In **a)**, the pulse sequence is shown. A $\pi/2$ pulse creates a coherent superposition between the S and D states. A LS laser pulse of duration T is applied, inducing a differential Stark shift. To suppress the influence of slow laser frequency drifts, a spin-echo π-pulse is implemented using the qubit laser. After a second free-evolution interval of duration T, a final $\pi/2$-pulse maps the accumulated phase onto a population difference, enabling state readout. In **b)**, the corresponding Rabi fringes for ions $0-5$ are shown. A large crystal of 91 ions was illuminated with LS 1 at an optical power of 340 mW. Solid lines represent sinusoidal fits to the data, and the error bars indicate uncertainties estimated using the Jeffreys integral using a confidence interval of 68 % [80].

The optical powers of the two LS beams were set to 310 mW for LS 1 and 340 mW for LS 2, respectively. To determine the Stark shift of each ion, the excitation probability was recorded as a function of time, revealing characteristic Rabi fringes. These oscillations were measured separately for each ion and each LS beam. Figure 5.4b) shows representative Rabi fringes for ions 0–5 obtained with LS 1. The error bars in the plot are obtained from Jeffrey's integral [80], using a confidence interval of 68 %. By fitting the data with a sinusoidal function (solid line), the Rabi frequency Ω was extracted from the oscillation period and used to calculate the corresponding Stark shift, $\Delta E = \Omega/2\pi$. By recording the differential Stark shift experienced by each ion as a function of its position within the crystal, the spatial intensity profile, and thus the beam size, can be extracted. The resulting data is shown in Fig. 5.5.

The ion positions can serve as a precise spatial ruler, provided that the trap oscillation frequencies have been accurately measured. With this, the beam profile can be determined and the measured Stark shift distribution can be fitted with a 2D Gaussian function of the

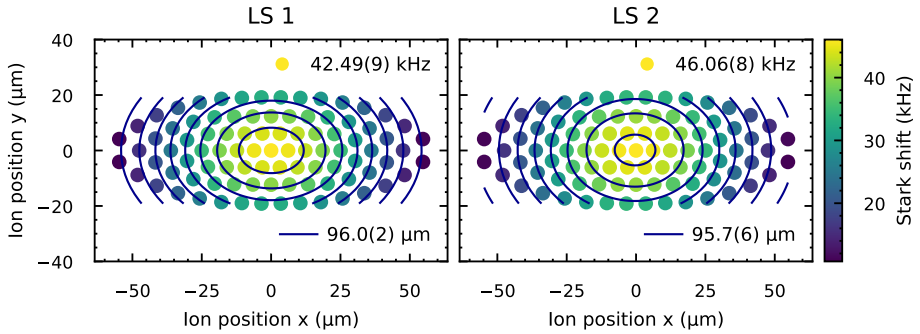

Figure 5.5: **Beam size measurement.** For a large 91-ion crystal, the AC Stark shift was measured individually for each ion. By fitting the spatial Stark shift distribution with a 2D Gaussian profile, the beam waist of the applied LS beam was extracted. The optical powers were 310 mW for LS 1 and 340 mW for LS 2, respectively. The qubit transition used in this measurement was $\Delta m = 0$. From the fits, the beam diameters were determined to be 96.0(2) µm for LS 1 and 95.7(6) µm for LS 2.

form:

$$I(x,y) = A \cdot \exp\left(-\frac{(x-x_0)^2}{2\sigma_x^2} - \frac{(y-y_0)^2}{2\sigma_y^2}\right), \tag{5.11}$$

where A denotes the peak Stark shift at the beam center, (x_0, y_0) represent the beam center coordinates, and σ_x, σ_y are the standard deviations along the respective axes. Note that the differential Stark shift is proportional to the local laser intensity (see Eq. 3.20). The beam waists are defined as the radii at which the intensity falls to $1/e^2$ of the maximum. These are related to the Gaussian standard deviations by $\omega_{x/y} = \sqrt{2}\sigma_{x/y}$. To calculate the beam diameters, it is assumed that the beam has a circular intensity profile, and its propagation direction is perpendicular to the short principal axis (y-axis) of the ion crystal. Under these conditions, the angle between the beam and the long principal axis (x-axis) of the crystal can be determined by $\theta = \arccos(\sigma_y/\sigma_x)$, yielding $\theta = 45.5(2)°$, which is in good agreement with the expected geometry. From this, the extracted beam diameters are 96.0(2) µm for LS 1 and 95.7(6) µm for LS 2, respectively.

Based on the extracted beam diameters, we can now compare the experimentally measured peak Stark shift at the beam center with the simulated value. For LS 1 with a power of 310 mW and a beam waist of 48.0(1) µm, the simulation predicts a Stark shift of 66.2 kHz. For LS 2 with a power of 340 mW and a beam waist of 47.9(3) µm, we obtain a simulated Stark shift of 73.0 kHz. However, a significant discrepancy is observed between the simulated and measured Stark shifts. While partial deviations may be attributed to reflection losses at the vacuum viewport, these losses alone are insufficient to account for the full deviation. Therefore, further investigation is required to identify additional sources of error and to fully understand the origin of the observed discrepancy between measurement and simulation.

5.2.2 STARK SHIFT FOR DIFFERENT SD TRANSITIONS

Next, we examined the differential Stark shifts for various $S_{1/2} \leftrightarrow D_{5/2}$ transitions. Even if the absolute values do not match, comparing the relative differences between transitions can reveal whether the model captures the underlying trends or if there are fundamental discrepancies.

The Stark shifts were measured for three transitions originating from the $S_{1/2}, m_j = -1/2$ ground state:

- $S_{1/2}, m_j = -1/2 \leftrightarrow D_{5/2}, m_j = -1/2$ ($\Delta m = 0$),
- $S_{1/2}, m_j = -1/2 \leftrightarrow D_{5/2}, m_j = -5/2$ ($\Delta m = -2$), and
- $S_{1/2}, m_j = -1/2 \leftrightarrow D_{5/2}, m_j = +3/2$ ($\Delta m = +2$),

The pulse sequence used for these measurements is identical to that presented earlier in Fig. 5.4a). The results are shown in Fig. 5.6. The error bars are estimated using Jeffrey's integral [80] with a confidence interval of 68 %. As previously noted, the absolute scale

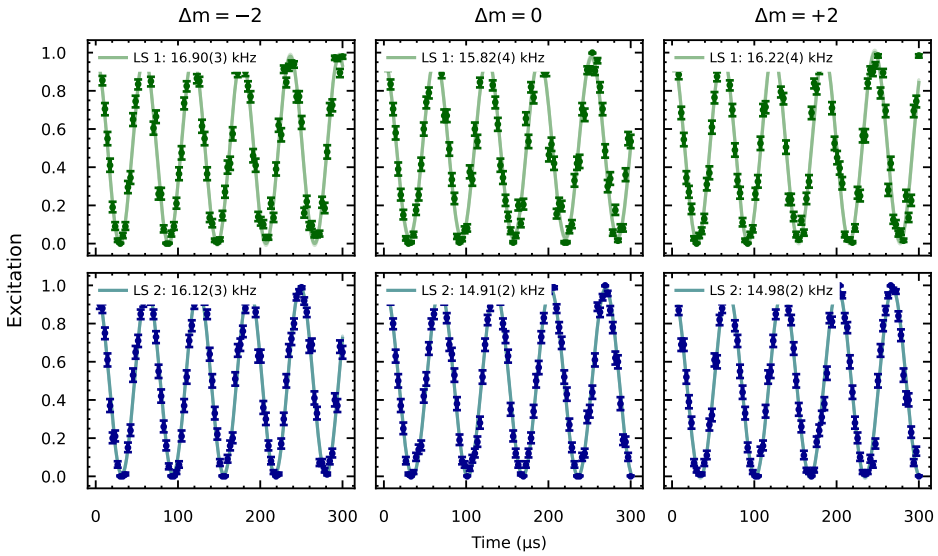

Figure 5.6: **Differential Stark shifts for S to D transitions**. Specifically, the Stark shifts were measured for $\Delta m = -2, 0, +2$ for a single ion with both beams. Here, the upper row shows the Stark shifts measured with the LS 1 beam and the second row with the LS 2 beam, respectively. The error bars are estimated using Jeffrey's integral, using a confidence interval of 68 % [80].

of the Stark shifts did not agree with theoretical predictions. For this reason, we instead considered the ratios of the measured Stark shifts for different transitions and compared them with the corresponding simulated ratios. The results are summarized in Tab. 5.1. As shown, the experimentally obtained Stark shift ratios are in good agreement with the simulated values, indicating that the relative transition strengths and polarization effects

are well captured by the model. This gives a hint that the discrepancy in absolute values of the Stark shifts either stems from experimental imperfections or that there is a factor 2 missing in some of the definitions that are used in the simulation.

Ratio	Simulation	LS 1	Deviation	LS 2	Deviation
$\Delta m = 0/\Delta m = -2$	0.930	0.936(3)	0.6(3) %	0.925(2)	0.5(2) %
$\Delta m = 0/\Delta m = +2$	0.976	0.975(3)	0.1(3) %	0.995(2)	2.0(2) %
$\Delta m = -2/\Delta m = +2$	1.049	1.042(3)	0.7(3) %	1.076(2)	2.6(2) %

Table 5.1: **Comparison between simulated and measured ratios of AC Stark shifts for different transitions**. The table shows the ratios of Stark shifts between the transitions $\Delta m = -2, 0, +2$ for a single ion. Both LS 1 and LS 2 beams were used in the measurement. The deviations indicate the relative difference between the measured and simulated values.

5.2.3 DIFFERENTIAL STARK SHIFT IN THE D MANIFOLD

Next, we analyzed the AC Stark shift within the $D_{5/2}$ manifold. In particular, the Stark shifts associated with the transitions:

- $D_{5/2}, m_j = -1/2 \leftrightarrow D_{5/2}, m_j = -5/2$ ($\Delta m_D = -2$) and
- $D_{5/2}, m_j = -1/2 \leftrightarrow D_{5/2}, m_j = -3/2$ ($\Delta m_D = -1$)

were measured. Previously, the differential Stark shift of the $S_{1/2} - D_{5/2}$ transition was measured using a Ramsey sequence on the optical qubit. To determine the Stark shift within the $D_{5/2}$ manifold, it is necessary to first prepare a coherent superposition of the relevant $D_{5/2}$ states. Since we cannot directly drive the magnetic transitions between two D levels, a sequence of 729 nm pulses has to be utilized for this. To this end, we employ the following pulse sequence (see Fig. 5.7a)), exemplified for the $\Delta m_D = -2$ transition. The sequence begins by applying a $\pi/2$ pulse on the $S_{1/2}, m_j = -1/2 \leftrightarrow D_{5/2}, m_j = -1/2$ transition using the 729 nm laser. The remaining population in the ground state is then transferred to $D_{5/2}, m_j = -5/2$ via a π pulse on the corresponding transition, resulting in a coherent superposition of the two $D_{5/2}$ Zeeman sublevels. After application of the LS pulse of duration T, the echo pulse, which consists of three π pulses (π pulse on $-5/2$ to transfer to the GS, then another π pulse for the spin-echo, with another π pulse, the GS population is transferred back to $-5/2$) is applied. The system is then allowed to evolve for an additional waiting time T, during which no LS pulse is applied. Finally, the $D_{5/2}, m_j = -5/2$ population is transferred back to the ground state via a π pulse. The $\pi/2$ pulse applied to the $D_{5/2}, m_j = -1/2$ state serves solely to close the Ramsey sequence and does not map the optical qubit onto the ground-state qubit.

The differential AC Stark shifts in the $D_{5/2}$ manifold are shown in Fig. 5.7b). Since the absolute Stark shifts deviated from theory, we compared measured Stark-shift ratios for different transitions to simulated values, see Tab. 5.2. Due to a different power setting in the LS beams, we repeated the measurement of the $S_{1/2} \leftrightarrow D_{5/2}$ differential Stark shifts to obtain accurate values. For the $\Delta m = 0$ transition, we measured differential Stark shifts of 19.92(3) kHz for LS 1 and 20.96(3) kHz for LS 2. For the $\Delta m = -2$ transition, the

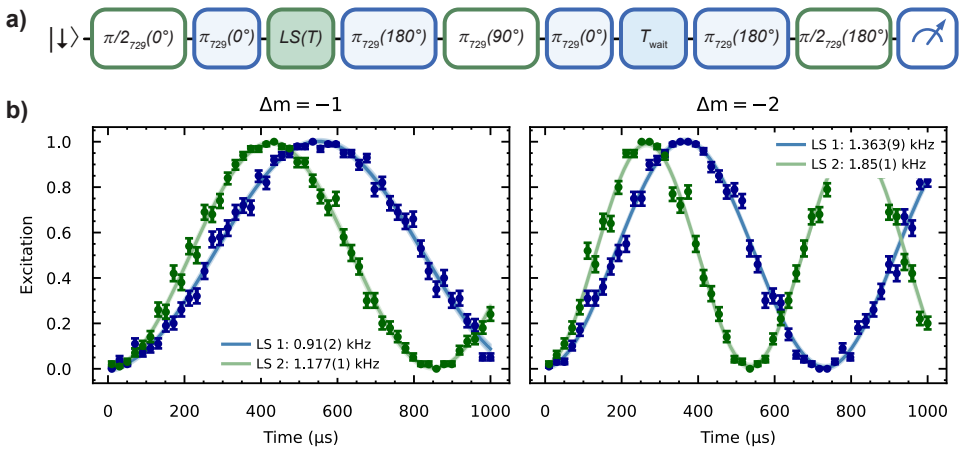

Figure 5.7: **Differential Stark shift in the D manifold**. a) shows the pulse sequence. First, a superposition of two Zeeman sublevels is generated via a $\pi/2$ and a π pulse. The Stark shift is induced by a LS pulse of duration T. The sequence includes a spin-echo consisting of three π pulses. After a wait time T, the populations are returned to the ground state, completing the Ramsey sequence. Boxes with a green frame indicate the $\Delta m = 0$ transition, while light blue boxes correspond to the $\Delta m = -2$ or $\Delta m = -1$ transition. b) shows the measured Stark shift for both beams for a single ion. Here, the Stark shift was measured for the transitions $\Delta m_D = -1$ (left panel) and $\Delta m_D = -2$ (right panel).

corresponding differential Stark shifts were 21.34(5) kHz for LS 1 and 22.81(3) kHz for LS 2.

A significant discrepancy is observed between experimental measurements and theoretical predictions when comparing the ratio of the differential Stark shift within the D manifold to the Stark shift between the S and D levels. In particular, ratios involving the $\Delta m_{DD} = -1$ transition exhibit pronounced deviations of up to a factor of two. This discrepancy warrants further investigation and may arise either from an error involving the $D_{5/2}$ states in the simulation or from measured Rabi fringes that are higher than expected. Ratios that do not involve the $\Delta m_{DD} = -1$ transition also deviate from the simulated values, although to a lesser extent. We tentatively attribute these remaining deviations to polarization imperfections, as the $D_{5/2}$ manifold is intrinsically more sensitive to polarization effects due to the fine structure of the D manifold and the corresponding Clebsch–Gordan coefficients. Our working hypothesis is that the LS beams exhibit a small deviation from ideal linear polarization. Introducing a slight ellipticity of approximately 4.9 % for LS 1 in the simulations reduces the discrepancy for transitions not involving $\Delta m_{DD} = -1$ to within 0.7 %. For LS 2, an ellipticity of roughly 13.3 % accounts for the observed deviations for the same subset of transitions, yielding discrepancies of up to 0.04 %. To test this hypothesis experimentally, one would need to probe the sensitivity of the $D_{5/2}$ manifold to polarization imperfections by comparing transition frequencies between Zeeman sublevels $m \leftrightarrow m'$ and their mirror counterparts $-m \leftrightarrow -m'$. The LS beams are nominally linearly polarized. Any residual ellipticity introduces a circular component that breaks the mirror symmetry of the transitions, leading to small differential frequency shifts. By measuring and comparing these transitions, one could directly

Ratio	Simulation	LS 1	Deviation	LS 2	Deviation
$\Delta m_{SD} = 0/\Delta m_{DD} = -2$	13.286	14.6(1)	10.2(9) %	11.33(6)	14.7(5) %
$\Delta m_{SD} = -2/\Delta m_{DD} = -2$	14.286	15.7(1)	9.8(9) %	12.33(7)	13.7(5) %
$\Delta m_{DD} = -2/\Delta m_{DD} = -1$	3.000	1.50(4)	50(3) %	1.568(8)	47.7(6) %
$\Delta m_{SD} = 0/\Delta m_{DD} = -1$	39.858	21.9(5)	45(3) %	17.76(3)	55(1) %
$\Delta m_{SD} = -2/\Delta m_{DD} = -1$	42.858	23.5(5)	45(3) %	19.33(3)	55.0(1) %

Table 5.2: **Comparison between simulated and measured ratios of AC Stark shifts in the D manifold**. The table shows ratios of Stark shifts between SD and DD transitions for a single ion. The measured Stark shifts in the D manifold involves the transitions $\Delta m_D = -2$ and $\Delta m_D = -1$. The resulting ratios are subsequently compared with the experimentally measured Stark shifts for the SD transitions as well as with theoretical predictions.

quantify these polarization imperfections. While such measurements were not performed for the $D_{5/2}$ manifold, Fig. 5.6 shows small differences in the AC Stark shifts of the S to D transitions for $\Delta m = \pm 2$ of up to 1.1 kHz. These observations provide an initial indication of residual polarization imperfections. To fully assess their impact, the measurements should be repeated for the $D_{5/2}$ manifold, where polarization effects are expected to be more pronounced.

5.2.4 GROUND STATE STARK SHIFT

In future experiments involving LS gates, we aim to implement two-qubit gates on the optical qubits using a global laser beam. To achieve this, selected ions are transferred from the ground-state (GS) qubit manifold to an optical qubit using the individually addressed 729 nm laser. These optical qubits are then entangled via the global 532 nm laser. It is crucial that the LS laser does not affect the remaining GS qubits, i.e., it must not induce any unwanted differential Stark shift. Otherwise, the Stark shift of each GS qubit would have to be precisely monitored and compensated, which introduces significant experimental overhead and makes the system highly sensitive to polarization and intensity drifts of the LS laser.

The pulse sequence used for this measurement is conceptually similar to that shown in Fig. 5.4a). However, instead of employing the 729 nm laser to create the superposition, an RF pulse is applied via a magnetic coil to coherently manipulate the GS Zeeman levels. The result of this measurement is presented in Fig. 5.8. Due to the large detuning from the fine structure of the P manifold and the use of linearly polarized light, the differential Stark shift in the GS qubit cancels. By fitting the experimental data with a sinusoidal model (not shown), we extracted an upper bound for the differential Stark shift of 0.7(4) Hz. This result is consistent with theoretical predictions, confirming that the differential Stark shift is essentially negligible.

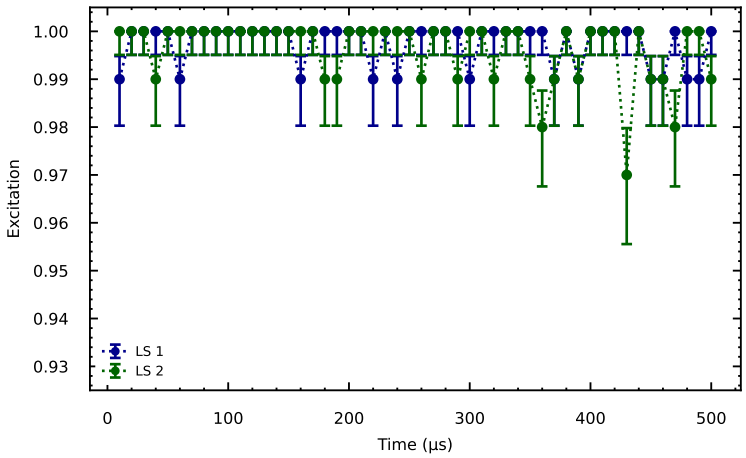

Figure 5.8: **Ground state Stark shift**. The differential Stark shift was measured for a single ion for both beams. The ground state Stark shift for LS 1 is represented in blue, while the ground state Stark shift for LS 2 is depicted in green, respectively. Error bars are estimated from Jeffrey's interval, using a 68 % confidence interval.

5.3 CHARACTERIZATION OF THE OPTICAL DIPOLE FORCE

Having thoroughly characterized the AC Stark shifts for various electronic transitions, we now turn to the implementation of the ODF, which we characterize by measuring displacements of the motional mode. In contrast to the measurements presented previously, we now simultaneously apply both LS beams to generate a moving standing wave. We investigate two regimes: an on-resonant displacement of the motional mode and an off-resonant displacement leading to closed trajectories in phase space.

5.3.1 RESONANT DISPLACEMENT OF THE MOTIONAL MODE

We start by examining the resonant displacement of the motional mode. For this, the frequency detuning between the two beams is set to match the COM mode frequency of 2.222 MHz, enabling coupling to the motional mode. In the following, we refer to this operation as the ODF pulse. To perform the measurement, the COM mode is ground-state cooled using EIT cooling. An ODF pulse resonant to the motional mode is applied for a duration τ, which displaces the ion's motional wavefunction; if the ion is initially in the motional ground state, this displacement corresponds to the creation of a coherent state, as introduced in Sec. 3.4. To probe the motional state after the displacement, we apply an analysis pulse using the 729 nm laser on the BSB. The excitation dynamics in time of this BSB pulse is very sensitive to the motional state, thus a fit of this dynamics allows for an estimation of the distribution of occupied motional Fock states (at least for motional states in our parameter regime, i.e. coherent states with moderate displacements) [81]. The pulse sequence for this measurement is shown in Fig. 5.9. A key ingredient for the LS gate are state-dependent dipole forces (due to state-dependent differential Stark shifts). Thus, we characterize the strength of the ODF for various intial electronic states, among them the qubit states $S_{1/2}, m_j = -1/2$, $D_{5/2}, m_j = -1/2$ and $D_{5/2}, m_j = -5/2$, the latter

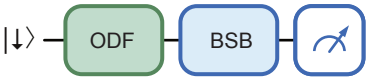

Figure 5.9: **Pulse sequence for the resonant displacement of the motional mode**. The ion is ground-state cooled. An ODF pulse resonant to the motional mode is applied for a duration τ. With a BSB pulse, the motional state after the displacement can be probed.

being a check for consistency.

We start with the displacement of the $S_{1/2}, m_j = -1/2$ state. For each step we apply an ODF pulse with pulse lengths between 0 µs and 200 µs. This has shown to be sufficient for a robust fit of the excitation dynamics. The resulting excitation dynamics for three different ODF pulse lengths (0, 100 and 200 µs) are shown in Fig. 5.10a). For an ODF pulse length of 0 µs, i.e. without the application of an ODF pulse, the ion is close to the motional ground state with a high population in $\bar{n} = 0$. In this regime, one expects Rabi fringes on the BSB with a large contrast, assuming negligible heating. The experimental data, however, shows a slightly reduced contrast, which is consistent with the residual mean occupation number of $\bar{n} \approx 0.05$ typically achieved with EIT cooling. For measurements with applied ODF pulses, a rapid decay of the BSB contrast towards zero is observed, followed by a revival at longer pulse durations. This behavior is characteristic of a coherent motional state. In contrast, for a thermal state, the contrast would decay to zero and remain there without revival. As predicted by the Jaynes–Cummings model, the internal-state population $P_\uparrow(t)$ exhibits characteristic quantum collapses and revivals as a function of time [82]. These revivals are a purely quantum mechanical phenomenon, arising from the discrete nature of the energy spectrum and the relatively narrow initial distribution over motional Fock states [82, 83]. In this regime, the system interacts with quantized motion, and the individual Rabi fringes associated with different motional states evolve with slightly different frequencies. The resulting dephasing leads to an apparent collapse of the population oscillations. At specific later times $\tau_{\text{revival}} = 4\pi\sqrt{\bar{n}}/\Omega$, the relative phases of the individual components re-align, leading to a revival of coherent oscillations. In contrast, if the motion were treated classically, i.e., a continuous distribution of motion energy, the overlapping oscillations would produce a continuous interference pattern, obscuring the distinct revival structure. The observed collapse and revival dynamics thus serve as a hallmark of the underlying quantum nature of the ion–field interaction [81].

To quantify the distribution of occupied motional states, we perform a fit of the data with the time-dependent excitation probability [81]

$$P_\uparrow(t) = \sum_n P_n \sin^2\left(\frac{\Omega_{n,n+1}}{2}t\right), \tag{5.12}$$

where the Rabi frequency between levels $|\downarrow, n\rangle$ and $|\uparrow, n+1\rangle$ is $\Omega_{n,n+1} = \sqrt{n+1}\cdot\eta\Omega$. Ω is the Rabi frequency of the carrier transition, which we measure to be 148.6(2) kHz and take as a fixed parameter in the fit. η is the Lamb-Dicke parameter given as $\eta = 2\pi/\lambda \cdot \sqrt{\hbar/(2m\nu_{\text{mode}})} = 0.065$, where $\lambda = 729\,\text{nm}$ and $\nu_{\text{mode}} = 2\pi \cdot 2.222\,\text{MHz}$. The term P_n represents the occupation probability of the n-phonon state in the initial motional

distribution and is treated as an independent fitting parameter.

From the fit shown in Fig. 5.10a), the phonon number distribution P_n can be extracted. Figure 5.10b) shows the related histograms of the distribution P_n. As expected without an ODF pulse we mostly occupy the motional ground state with little occupation of higher phonon states due to imperfect cooling. For a displaced motional ground state, the distribution turns into a Poissonian distribution as expected from quantum theory for a coherent state, as introduced in Sec. 3.4. A Poissonian fit of the form

$$P(n) = |\langle n|\alpha\rangle|^2 = e^{-\bar{n}}\frac{\bar{n}^n}{n!}, \tag{5.13}$$

reveals the mean phonon number $\bar{n}$, which is related to the displacement amplitude by

$$\bar{n} = \langle a^\dagger a\rangle = |\alpha|^2. \tag{5.14}$$

The extracted distribution is shown in Fig. 5.10b), where a Poissonian fit (green curve) is overlaid. The good agreement with the fit confirms that the ion's motional state closely approximates a coherent state under the applied ODF. For the initial state we do not expect a Poissonian distribution. In the ideal case, just the ground-state is occupied, i.e. a single Fock state. Imperfect cooling can leave the state either in a thermal or non-thermal state, which makes a proper fit challenging. Fig. 5.10b) employs a Poissonian fit as well as a thermal fit of the form

$$P(n)_{\text{therm}} = N\cdot\left(\frac{\bar{n}}{1+\bar{n}}\right)^n \tag{5.15}$$

for the initial state. Here, N describes a normalization constant.

By using Eq. 5.14, we can now calculate the diplacement α from the phonon number distribution shown in Fig. 5.10b) and plotted as a function of the ODF pulse length. The extracted values are then compared to the theoretical prediction, given by

$$\alpha = \eta_{532}\cdot\Delta E_{S_{1/2}}\cdot\tau_{\text{ODF}}, \tag{5.16}$$

where $\eta_{532} = 0.126$ is the Lamb-Dicke parameter for the ODF beam at 532 nm and mode frequency 2.22 MHz. $\Delta E_{S_{1/2}}$ is the Stark shift of the $S_{1/2}$ level and τ_{ODF} is the duration of the applied ODF pulse. Since the absolute Stark shift of the $S_{1/2}$ cannot be measured directly, we measure the differential Stark shift for the $\Delta m = 0$ transition. The observed differential shifts were 15.47(2) kHz for LS 1 and 15.68(3) kHz for LS 2. From the simulations, we get a relation $\Delta E_{SD,\Delta m=0}\times 0.95 = \Delta E_{S_{1/2},m_j=-1/2}$. With this, we get a Stark shift of $\Delta E_{S_{1/2}} = 14.80(2)$ kHz. In this analysis, the geometric mean of the Stark shifts induced by the two individual LS beams was used to account for their combined effect. The experimental results, along with the theoretical predictions from Eq. 5.16, are presented in Fig. 5.10c). The experimentally extracted displacement values show good agreement with the theoretical prediction. However, for short ODF pulse durations of approximately up to 25 µs, a slight deviation is observed, since we start in the motional ground-state being a Fock state rather than a coherent state. At longer pulse durations, good agreement

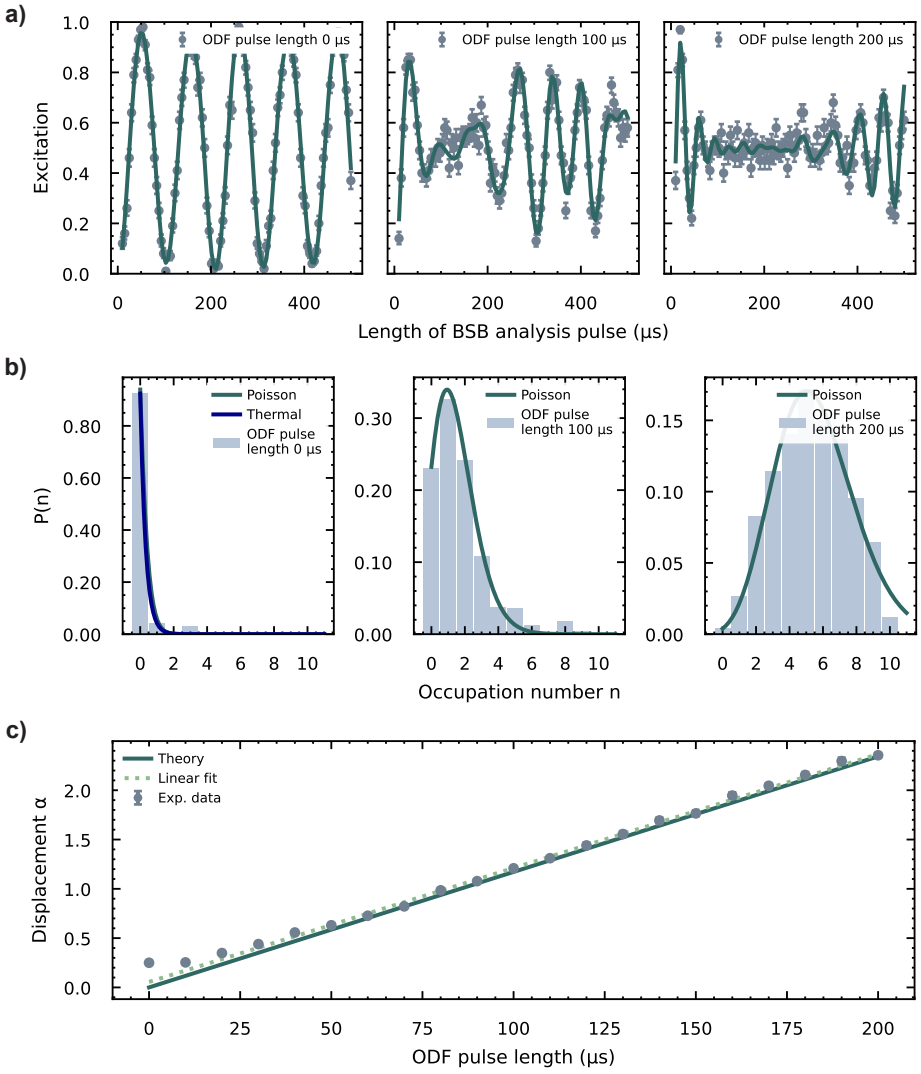

Figure 5.10: **Displacement of the motional state** $S_{1/2}, m_j = -1/2$. In **a)**, three representative BSB analysis pulses are shown: one without displacement and two following ODF pulses of 100 µs and 200 µs duration. The solid lines represent fits acoording to Eq. 5.12, providing information on the motional mode population. **b)** shows the reconstructed phonon number distribution extracted from a). A Poissonian fit (green curve) is overlaid. In the beginning, where the motional ground state is not in a pure state, we fit a thermal distribution (blue curve) additionally. Note the different scaling of the y-axis. **c)** shows the extracted displacement amplitude from b) as a function of the ODF pulse length. The solid line illustrates the simulated displacement amplitude according to Eq. 5.16. The dashed line represents a linear fit of the experimental data.

between theory and experiment is observed, where the initial non-coherent part is gone.

Next, we turn to the second qubit state, namely $D_{5/2}, m_j = -1/2$. In this case, the optical power in the ODF beams had to be significantly increased in order to observe a measurable signal. This is in agreement with theory since the absolute Stark shift of the $D_{5/2}, m_j = -1/2$ state is smaller by a factor of 19.02 compared to the $S_{1/2}, m_j = -1/2$ state, leading to a proportionally reduced ODF strength. The measured differential Stark shifts for the $\Delta m = 0$ transition were 39.1(1) kHz for LS 1 and 28.73(8) kHz for LS 2, respectively. Using the simulations from Sec. 3.2, the absolute Stark shift of the state $D_{5/2}, m_j = -1/2$ was estimated to be 1.67(6) kHz, calculated as the geometric mean of the two measured differential shifts. To achieve a sufficient Stark shift for this measurement, the ODF beams were operated at the maximum available power. However, due to imperfect alignment of the LS 2 beam, its effective power at the ion position was lower than that of LS 1. Due to the substantial discrepancy between the individual shifts from LS 1 and LS 2, the validity of using a geometric mean in this case is uncertain and may not accurately reflect the true single-beam contributions. Additionally, to compensate for the weaker coupling, the ODF pulse duration was extended substantially, ranging from 0 ms to 20 ms. The result is shown in Fig. 5.11a). The data was fitted again with Eq. 5.12. As can be seen from the plot, the collapse and revival of the wavefunction is a lot weaker than in the case for the $S_{1/2}, m_j = -1/2$ state. From Fig. 5.11a), we can again extract the phonon distributions, which are shown in Fig. 5.11b). From the phonon number distribution shown in Fig. 5.11b), the displacement amplitude α was extracted and compared with the theoretical prediction, as presented in Fig. 5.11c). A significant deviation between the experimental data and theoretical model is observed. While the data still exhibits the expected linear behavior, the slope differs noticeably from the simulated prediction. One possible explanation is the increased sensitivity of the $D_{5/2}$ state to polarization imperfections compared to the $S_{1/2}$ state, suggesting that the polarization of the ODF beams may not be perfectly linear, as already discussed in Subsec. 5.2.3. Additionally, the observed imbalance in the differential Stark shifts from the two beams could likely contribute to the discrepancy.

As a check for consistency, we perform another measurement with the ion initialized in the $D_{5/2}, m_j = -5/2$ Zeeman sublevel. For the $\Delta m = -2$ transition, the observed differential Stark shifts were 21.34(5) kHz for LS 1 and 22.80(3) kHz for LS 2. Using the simulations, we get an absolute Stark shift of $\Delta E_{D_{5/2}, m_j = -5/2} = 2.24(3)$ kHz. The displacement of the motional state is probed with ODF pulse lengths ranging from 0 ms to 2 ms. The resulting data is shown in Fig. 5.12. A significant deviation between the experimental data and theoretical model is observed. Most likely, the simulations do not fully capture the atomic-physics model of the D states, although this requires further investigation.

5.3.2 OFF-RESONANT DISPLACEMENT OF THE MOTIONAL MODE

In order to make further progress toward the implementation of the LS gate, which relies on off-resonant excitation of a motional mode such that the motional state follows a closed trajectory in phase space, we investigated this regime by detuning the LS beams from the COM mode by $\delta = 2$ kHz. As discussed previously in Fig. 3.5d), such a detuning causes

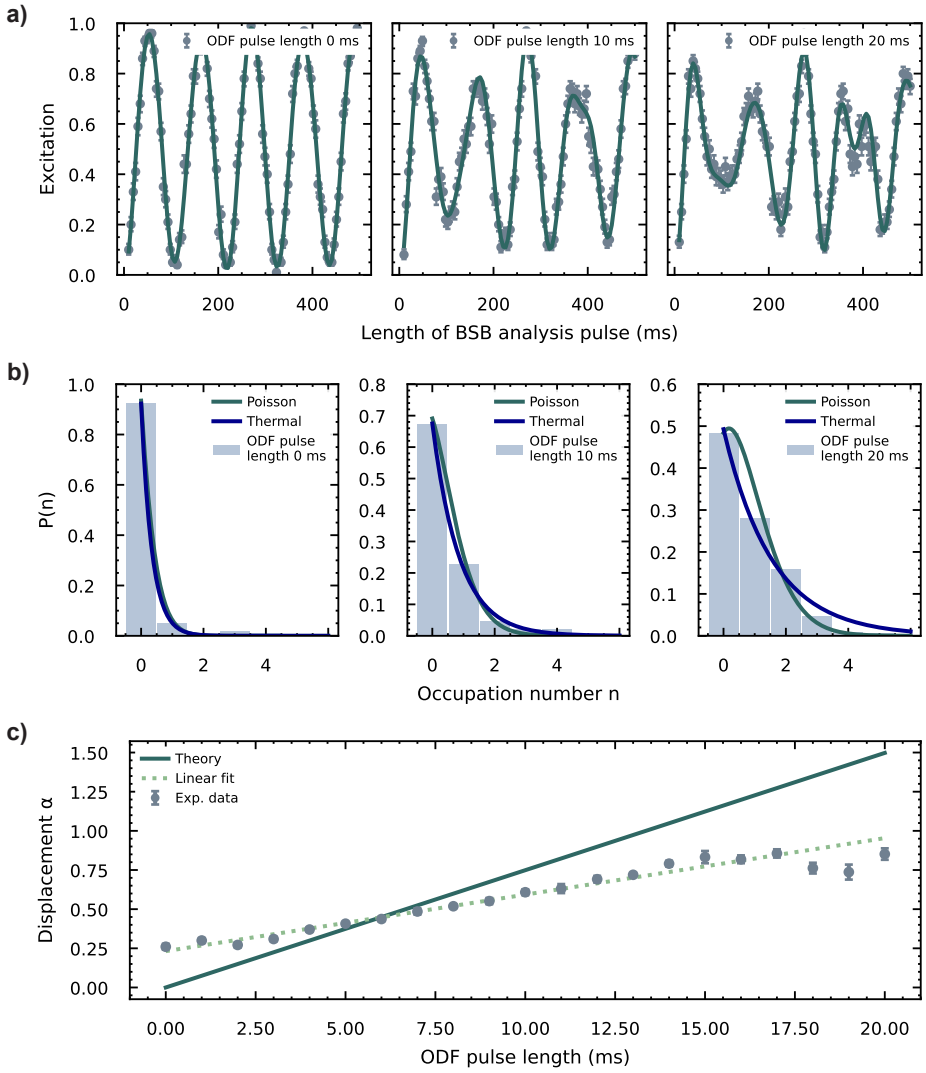

Figure 5.11: **Displacement of the motional state** $D_{5/2}, m_j = -1/2$. **a)** shows three representative BSB analysis pulses: one without displacement and two with ODF pulse lengths of 10 ms and 20 ms, respectively. The solid line represents fits according to Eq. 5.12. In **b)**, the reconstructed phonon number distributions from a) are shown. A Poissonian fit (green curve) is overlaid, as well as a thermal distribution (blue curve). Mind the different scaling of the y-axis. **c)** shows the extracted displacement amplitude from b) as a function of the ODF pulse length. The solid line shows the simulated displacement amplitude according to Eq. 5.16. The dashed line represents a linear fit to the experimental data.

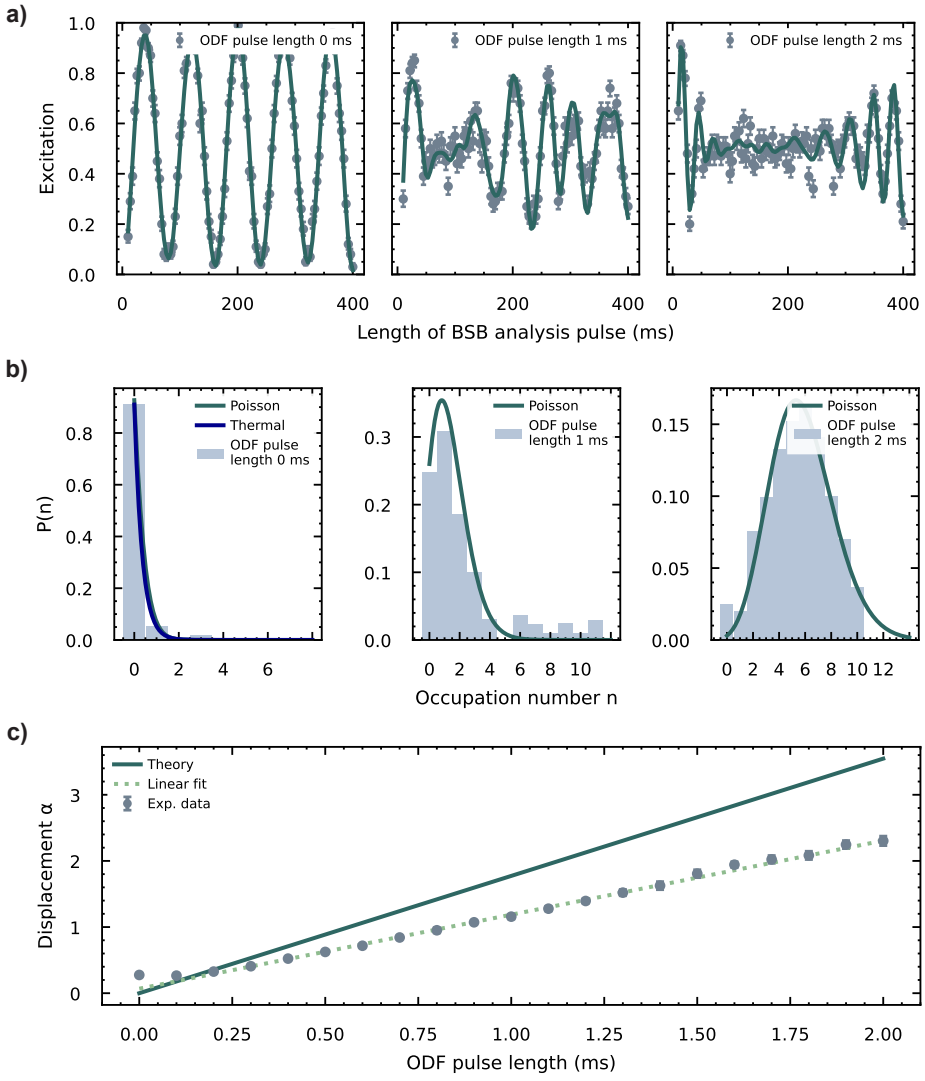

Figure 5.12: **Displacement of the motional state** $D_{5/2}, m_j = -5/2$. **a)** shows three representative BSB analysis pulses: one without displacement and two with ODF pulse lengths of 1 ms and 2 ms. The data is fitted with Eq. 5.12, represented by the solid line. In **b)**, the reconstructed phonon number distributions from a) are shown. A Poissonian fit (green) and a thermal fit (blue), for the initial ground state, are overlaid. Note the y-axis scaling. **c)** shows the extracted displacement amplitude from b) as a function of the ODF pulse length, where the solid line shows a fit according to Eq. 5.16. The dahsed line represents a fit to the experimental data.

the motional state to perform closed trajectories in phase space. For this experiment, we again use the $\Delta m = 0$ optical qubit transition and apply both LS beams simultaneously to generate a moving standing wave. The experimental sequence consists of an initial $\pi/2$ pulse of the 729 nm laser to create a superposition of the two electronic states, followed by an ODF pulse, and finally a second $\pi/2$ pulse of the 729 nm laser for state analysis. When the ODF pulse is applied to a superposition state, the motional wave packets are displaced in opposite directions for the two electronic components, thus creating entanglement between motion and the internal qubit state. This displacement can be characterized as [58, 84]

$$\alpha(t) = \frac{\eta \cdot \Delta_s}{2\delta} e^{i\delta t/2} \sin\left(\frac{\delta t}{2}\right), \tag{5.17}$$

where η is the Lamb-Dicke parameter, Δ_s the differential Stark shift, and δ the detuning from the COM mode. The resulting state after the displacement α and β can be described by

$$|\Psi\rangle = \frac{1}{\sqrt{2}}(e^{i\phi}|0\rangle|\alpha(t)\rangle + e^{-i\phi}|1\rangle|-\beta(t)\rangle), \tag{5.18}$$

where ϕ describes the accumulated qubit phase during the LS pulse. The resulting excitation dynamics are shown in Fig. 5.13a) and b). We did this measurement for two different powers, resulting in two different differential Stark shifts of 13.826(3) kHz for Fig. 5.13a) and 23.212(3) kHz for Fig. 5.13b). If a finite displacement ($|\alpha(t)| \neq 0$) is present, the two wave packet components remain partially separated, making the corresponding motional states distinguishable and carrying which-path information that suppresses the interference contrast [84]. In the absence of displacement ($|\alpha(t)| = 0$), the wave packets fully overlap upon recombination, resulting in maximal interference and thus in a revival of the contrast. More specifically, this happens at the time $t = 1/\delta = 500\,\mu s$. During this evolution, the electronic superposition and the motion become periodically entangled and disentangled as the wave packets separate and re-overlap, respectively. This leads to a characteristic decay and revival of the observed excitation as the motional trajectories complete successive loops. For Fig. 5.13a), the displacement was relatively small, such that the wave packets remained partially overlapping, allowing residual oscillations to be observed even at maximal separation. In the case for higher power, as shown in Fig. 5.13b), the larger displacement allows the wave packets to separate more, minimizing interference and resulting in a larger loss of contrast. The probability of measuring the qubit in the excited state after the sequence can be fitted with

$$P = |\langle\Psi|\sigma_y|\Psi\rangle|^2 = \exp\left(-16|\alpha(t)|^2 \sin^2\left(\frac{\theta}{2}\right)\right) \cdot \sin^2(2\phi), \tag{5.19}$$

where θ is the relative phase of the LS beams. The Lamb-Dicke parameter, the differential Stark shift, the detuning and the phases ϕ and θ are fitted according to Eq. 5.19. From this, the fit parameters are extracted and used to calculate the displacement by using Eq. 5.17 and represent it in the corresponding phase-space diagram, which demonstrates that the trajectory forms a closed loop. This condition is crucial for the gate to operate purely on the qubits and to remain robust against the initial motional state. In the context of LS

gates, closing the phase-space trajectory ensures that the motional degrees of freedom are fully disentangled from the qubits at the conclusion of the gate, leaving only the desired spin-dependent phase. We also compare the measured displacement with theoretical predictions, observing good agreement. A displacement of zero occurs at pulse length scans of 0 µs and 500 µs, where the loop starts and ends, as expected. The maximum displacement is reached at 250 µs, the point at which the contrast exhibits its minimum.

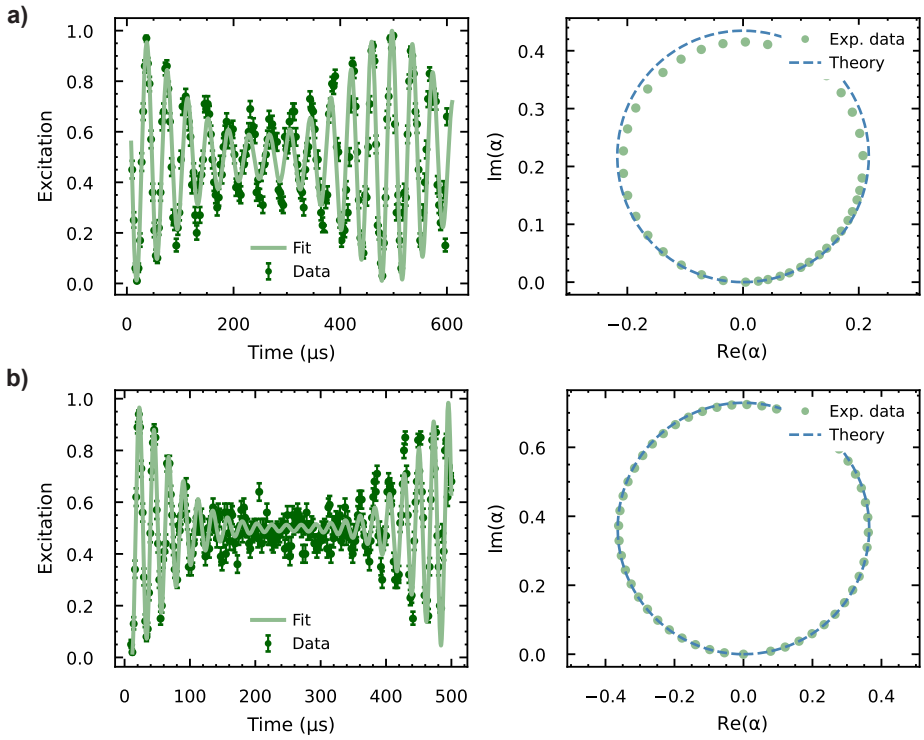

Figure 5.13: **Splitting and recombination of a motional wave packet**. The excitation dynamics are presented in **a)** for a differential Stark shift of 13.826(3) kHz and in **b)** for a differential Stark shift of 23.212(3) kHz. The solid lines represent fits to the data based on Eq. 5.19. The detuning of the LS beams was set to 2 kHz. The error bars correspond to one standard deviation, estimated using Jeffreys' integral with a 68 % confidence interval [80]. The extracted displacements are visualized in phase space and compared with theoretical predictions according to Eq. 5.20.

To quantify the actual separation of the wave packets induced by the displacement, we consider the distance between them, defined as

$$d = (|\alpha| - |\beta|)x_0 = (|\alpha| - |\beta|)\sqrt{\frac{\hbar}{2m\nu_{\text{mode}}}}, \tag{5.20}$$

where m is the ion mass and $\nu_{\text{mode}} = 2.22\,\text{MHz}$ the radial mode frequency. This gives a ground-state size of $x_0 = 7.55\,\text{nm}$. For the data shown in Fig. 5.13a), the displacement

amplitude is $\alpha = 0.42$, corresponding to a separation of $d = 6.34\,\text{nm}$. In Fig. 5.13b), $\alpha = 0.73$ yields $d = 11.02\,\text{nm}$. The interference contrast is higher for the smaller separation and reduced for the larger separation. To achieve a full loss of excitation probability contrast, a complete spatial separation of the wave packets is required with a displacement amplitude of $|\alpha| \geq 1$.

5.4 LIGHT-SHIFT GATES

Having thoroughly characterized both the AC Stark shift and the ODF mode coupling — two fundamental system characterizations — we now proceed to the implementation and analysis of the gate itself. To this end, experimental measurements were first carried out in a two-ion crystal to determine the basic gate properties, followed by an extension of the study to a ten-ion crystal to investigate scalability.

5.4.1 LS GATE IMPLEMENTATION AND CALIBRATION

Prior to presenting the experimental results for the LS gate, we will first discuss the initialization and calibration procedures. The gate implementation follows the pulse sequence illustrated in Fig. 5.14. Initially, a global $\pi/2$ pulse is applied to generate a coherent super-

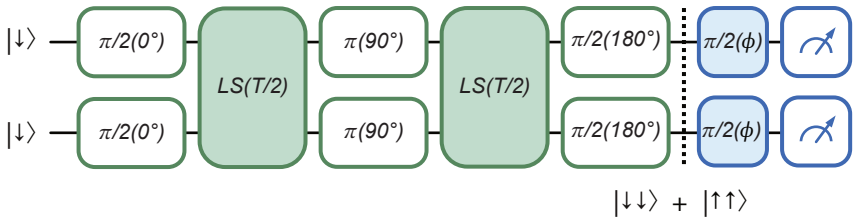

Figure 5.14: **Gate pulse sequence**. A $\pi/2$ pulse creates a superposition between $S_{1/2}$ and $D_{5/2}$ states. An off-resonant LS pulse of duration T is applied, completing the first loop in phase space. A subsequent spin-echo pulse is applied, in order to eliminate unwanted single qubit Stark shifts. Then another LS pulse is applied, closing the second loop in phase space. To read out the populations, an additional $\pi/2$ pulse is applied, which maps the populations from the x-basis onto the z-basis. An additional $\pi/2$ pulse can be applied for measuring the parity.

position between the $S_{1/2}$ and $D_{5/2}$ state. Since the amplitudes of the ODF differs for the $S_{1/2}$ and $D_{5/2}$ states due to different absolute Stark shifts, this leads to the accumulation of unwanted single-qubit phases during the gate operation. To compensate for these phases, eliminate unwanted single-qubit Stark shifts and enhance gate robustness, the operation is implemented in a two-loop configuration. For this, we split an off-resonant ODF pulse, from now on called LS pulse, in two equal parts and apply an echo pulse between them, where the spin-echo pulse inverts the qubit states between the loops, effectively canceling the single-qubit contributions while preserving the desired entangling phase. Finally, a $\pi/2$ pulse is used to map the state populations from the x-basis onto the z-basis. To evaluate the gate performance, we apply an additional single-qubit rotation via a $\pi/2$ pulse while varying the phase ϕ to measure parity oscillations. This operation rotates the measurement basis such that the relative phase between $|\downarrow\downarrow\rangle$ and $|\uparrow\uparrow\rangle$ is mapped onto the populations of the measurement basis states and we can record the resulting parity

signal, as already introduced in Sec. 3.5.3.

Before executing the full gate operation, a series of calibration steps are required to ensure optimal performance. This is done by measuring the state populations following the application of a gate sequence. Ideally, the gate sequence should be executed multiple times to amplify the effects of any errors, thereby enhancing the accuracy of the calibration process.

1. To enable efficient population transfer between the $S_{1/2}$ and $D_{5/2}$ states, the qubit transition frequency ω_{SD} is calibrated prior to gate operations by doing Ramsey spectroscopy with the 729 nm laser.

2. The ideal phase-space closure condition constrains the gate duration τ_g and the detuning of the modes δ via $\delta\tau_g = 2\pi n$, where n is an integer. In practice, pulse-shaping transients, AOM delays and nonlinearities cause deviations from the ideal relation. Therefore, we perform an iterative optimization: pick a nominal δ near the COM mode, set τ_g near $2\pi/\delta$, and then iteratively fine-scan τ_g and δ to minimize the undesired populations in the unwanted states $p_{\uparrow\downarrow} + p_{\downarrow\uparrow}$.

3. Similarly, the beam power is calibrated, as it determines the size of the phase-space loop traced by the ions. Maximum entanglement is achieved when the loop encloses the optimal geometric phase of π, which occurs at the correctly calibrated power.

5.4.2 TWO-ION CRYSTAL

To start with the simplest case, the LS gate was tested on a two-ion crystal. This configuration offers the advantage of manageable complexity: scaling to larger crystals becomes very challenging, as numerous effects, such as additional motional modes, make it more challenging to identify the correct gate parameters. The gate operation was performed on the transition between the electronic states $S_{1/2}, m_j = -1/2$ and $D_{5/2}, m_j = -1/2$, due to its reduced sensitivity to magnetic field fluctuations. To perform the LS gate, we first calibrated the gate according to the steps outlined in Subsec. 5.4.1. With this, the detuning from the COM mode was set to 5 kHz and the gate duration to 238 µs per loop. At first glance, one might wonder why the gate duration exceeds 200 µs. This longer duration arises from the pulse shaping of the LS beams, which is required to minimize excitation of the spectator mode. As a consequence, the phase-space trajectory must be extended slightly to ensure that it closes precisely at the origin, thereby completing the loop. The beam power was calibrated to 72 % of the full available power to generate a maximally entangling gate.

As already discussed in Sec. 3.5.3, we can evaluate the performance of the gate, and therefore the gate fidelity, by measuring the populations of the $|00\rangle$ and $|11\rangle$ states and parity oscillations. The result is shown in Fig. 5.15. On the left side, the parity oscillations are shown and on the right side, the populations are shown. For the parity, a contrast of 98.9(6) % is obtained. For the populations in the $|00\rangle$ state, we achieve 48(1) % and for $|11\rangle$ 52(1) %. The population in other states is 0.9 %. Based on these results, the gate fidelity can be calculated using Eq. 3.70, yielding a value of 99.0(8) %.

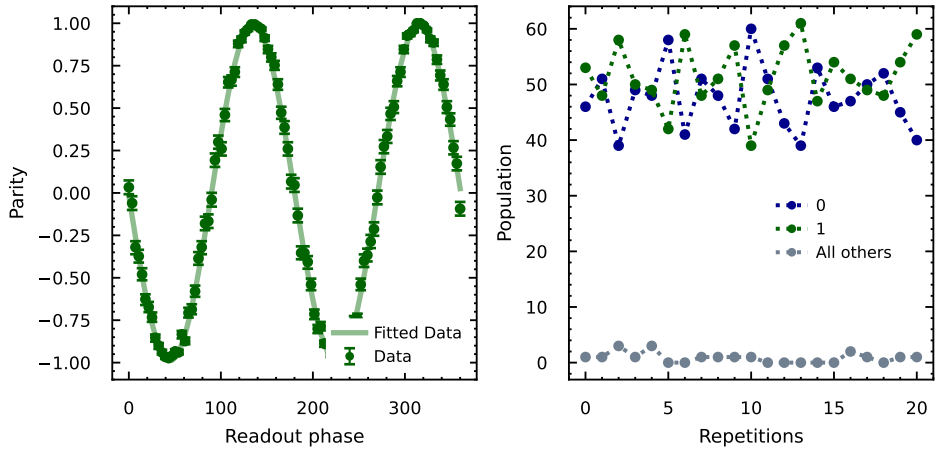

Figure 5.15: **LS gate on a two-ion crystal**. The transition $\Delta m = 0$ was used to perform the gate. The gate duration was calibrated to 238 µs per loop, and the detuning to 5 kHz. On the left side, a parity measurement can be seen. The amplitude is 98.9 %. On the right side, the population measurement is shown. Population in the $|00\rangle$ state is 47.6 % and in $|11\rangle$ 51.6 %. The population in other states is 0.9 %.

5

DISCUSSION

The measured gate fidelity of 99.0(8) % is slightly below the limit set by the best reported LS gates for two-ion crystals. Clark et al. demonstrated a state-of-the-art LS gate achieving a fidelity of 99.94(3) % (infidelity of $6(3) \times 10^{-4}$) for a gate duration of 35 µs [34]. While our gate operates close to the maximally entangling regime, its fidelity falls short of this benchmark, indicating the presence of residual technical imperfections. Based on simulations of the gate duration and gate errors, a higher fidelity could be expected, as the fundamental error arising from photon scattering and D-level decay (see Eq. 5.5) is estimated to be 4.16×10^{-4}, corresponding to a theoretical upper limit of 99.96 %. The discrepancy between the measured and theoretical limits suggests that technical factors currently dominate the error budget. One likely contributor is a slight population imbalance between the $|00\rangle$ and $|11\rangle$ states, implying that the phase-space trajectory does not perfectly accumulate the desired geometric phase. Residual motional excitation and small calibration inaccuracies in the detuning or gate duration may also cause minor qubit misrotations, further reducing the observed fidelity.

The observed technical imperfections likely originate from limitations in the current experimental setup. In particular, laser intensity fluctuations are expected to play a significant role. In the present configuration, 10-meter-long optical fibers connect the laser system to the ion trap. The extended fiber length introduces challenges for interferometric stability, which is critical for the performance of the LS gate. Optical fibers are highly sensitive to environmental perturbations: temperature fluctuations along the fiber can alter the refractive index and effective path length, while mechanical vibrations induce rapid phase fluctuations. Longer fibers amplify these effects, resulting in larger deviations

of the relative phase between the laser beams that drive the gate. Since the LS gate relies on precise phase relationships to generate state-dependent forces and accumulate the desired geometric phase, any phase drift directly reduces gate fidelity, often manifesting as a reduction in parity contrast. In the future, the laser system will be moved closer to the ion trap, which helps to reduce this effect. Another potential source of error originates from the laser, specifically from fluctuations in its intensity. Intensity fluctuations on the timescale of the gate alter the size of the phase-space loop and thus the accumulated geometric phase, leading to a mismatch in the final population. To address this problem, active power stabilization can be implemented, which will be discussed in Ch. 6. Implementing these improvements is expected to enhance LS gate fidelity to approach its theoretical limit.

5.4.3 TEN-ION CRYSTAL

Subsequently, we investigated the performance of LS gates in a ten-ion crystal. This was achieved using individually addressed 729 nm laser beams in conjunction with globally applied 532 nm laser beams. The pulse sequence is analogous to that used for the two-ion crystal (see Fig. 5.14); the key difference is that the 729 nm beams are applied in an addressed rather than a global manner. Under this configuration, only the addressed ions participate in the entangling interaction, while the non-addressed ions remain in their ground state, as shown previously in Sec. 5.2.4. To illustrate the operation of the gate in a multi-ion configuration, ions 4 and 6 were selected for entanglement, as shown in Fig. 5.16. This choice was arbitrary, since any ion pair within the crystal can, in principle, serve for this measurement.

Figure 5.16: **Ten-ion crystal**. The LS gate on a ten-ion crystal is achieved using addressed 729 nm beams and global 532 nm beams. Only the addressed ions 4 and 6 get entangled, the remaining ions stay in the ground state.

The gate was calibrated according to Subsec. 5.4.1, where we found a detuning of 305 µs per loop, a detuning from the COM mode of 3.32 kHz and the power to 100 % of the full available power. To evaluate the performance of the quantum gate, the fidelity was determined through two-qubit quantum state tomography using a maximum-likelihood estimation approach, as outlined in Sec. 3.5.3. This procedure involved preparing the target quantum state 1000 times and performing projective measurements in the eigenbases of the single-qubit Pauli operators σ_x, σ_y and σ_z (i.e. the $+X, -X, +Y, -Y, +Z$ and $-Z$ eigenstates). The reconstruction of the density matrix was carried out by iteratively solving Eq. 3.78 and is shown in Fig. 5.17. From the resulting density matrix, the fidelity was computed to be 79(1) %. The errorbars are obtained from Monte Carlo simulations, as described in Sec. 3.5.3. The purity of the states, defined as $\mathrm{Tr}(\rho^2)$, was determined to 69(2) %.

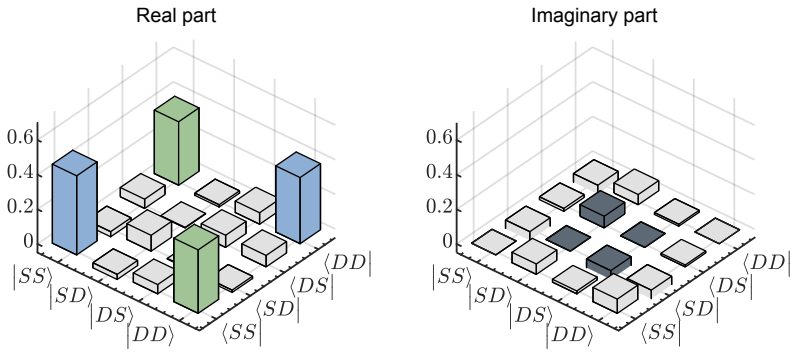

5

Figure 5.17: **Two-qubit state tomography reconstruction via MLE**. The density matrix was reconstructed by solving Eq. 3.78. With this, a fidelity of 79(1) % was achieved. The error bars stem from Monte Carlo simulations.

DISCUSSION

The observed gate performance is highly reduced compared to the two-ion case, with a measured fidelity significantly below unity and a state purity of 69(2) %. From simulations we theoretically expect a fidelity of 99.73 %, where the fundamental error is 2.70×10^{-3}. This discrepancy probably arises from the increased susceptibility of larger ion crystals to experimental imperfections. As the number of ions increases, the motional mode spectrum becomes denser, making the gates more sensitive to frequency drifts and timing errors. Moreover, spatial inhomogeneities and cross-talk between closely spaced ions enhance the system's sensitivity to laser intensity fluctuations and misalignment [85]. Furthermore, increasing the gate duration (in our case 305 µs per loop) extends the interaction time between the ions and the laser fields. As a result, laser intensity and phase noise act over a longer period, leading to enhanced phase fluctuations in both the qubit and motional states. In addition, magnetic-field noise and laser-frequency drifts can induce dephasing of the qubit transition during the gate. Collectively, these effects lead to greater sensitivity to noise and control errors. These noise sources can decohere the intended pure state, transforming it into a mixed state. As a result, both the fidelity, which measures the overlap with the ideal target state and the purity, quantifying the coherence of the state, are reduced. To the best of our knowledge, no experimental realization of a LS gate in extended ion crystals has been reported so far. Our results thus constitute an important demonstration that this gate mechanism can be successfully applied in larger ion systems. With the improvements outlined above, we are confident that the gate fidelity already achieved can be further enhanced.

6

System Enhancements

To enhance the fidelity of the LS gates, a number of improvements have been implemented in the experimental setup. In the first instance, active stabilization of the laser power was implemented in order to reduce intensity fluctuations, which are a primary cause of gate errors (see Sec. 6.1). We prove the functionality of the stabilization by means of relative intensity noise (RIN) measurements, showing a reduction of the noise level at the relevant frequencies of at least 20 dBc/Hz. Additional enhancements include the integration of new shorter optical fibers to enhance interferometric stability and fiber couplers, designed for high-optical powers, as will be discussed in Sec. 6.2. The design of the fiber couplers will be outlined, along with accompanying optical simulations.

6.1 Laser Power Stabilization

To further approach the theoretical performance limit of the LS gates, we implement laser-power stabilization. To this end, we actively stabilize the laser intensity in the frequency range between 10 Hz and 100 kHz, where intensity noise affects the performance of the gate. The configuration of the power stabilization system is illustrated in Fig. 6.1. A single-pass AOM[1] is positioned directly subsequent to the laser head. The zeroth-order diffracted beam is blocked with a beam block (BB), while the first-order diffracted beam is passed through a beam sampler (BS), directing the reflected beam onto a photodiode (PD)[2], which provides a feedback signal to a custom-built proportional-integral (PI) controller. The controller, in turn, regulates the RF power applied to the AOM, thereby stabilizing the diffracted laser power. The diffracted beam is directed towards the LS setup, as shown earlier in Fig. 4.4. The PI unit provides a low-noise bias voltage for the photodiode and includes a transimpedance amplifier for current-to-voltage conversion. This is followed by a low-noise analog PI controller that feeds back on a voltage-variable attenuator. The attenuator limits the unit's bandwidth to about 300 kHz.

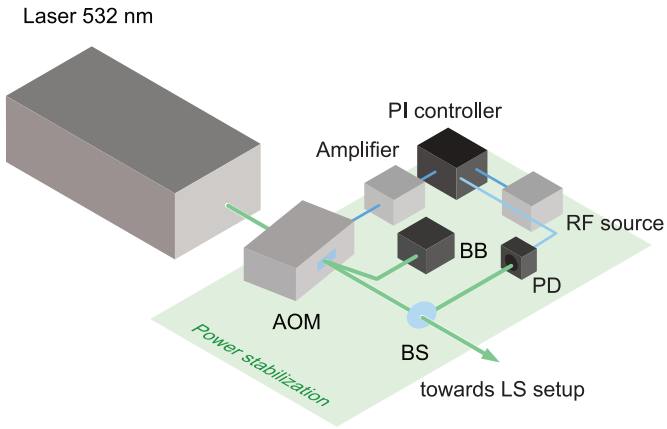

Figure 6.1: **Laser power stabilization**. The laser power is stabilized with a single-pass AOM. The zeroth-order beam is blocked with a beam block (BB), while the first-order diffracted beam passes through beam sampler (BS), directing the reflected beam to a photodiode (PD) that generates a feedback signal for a custom-built proportional-integral (PI) controller. The controller adjusts the RF drive (that is connected to the controller via an amplifier) applied to the AOM, ensuring the laser power remains stable. The diffracted beam is directed toward the LS setup, as shown earlier in Fig. 4.4.

6.1.1 Foundations of Intensity Noise Characterization

The performance of the power stabilization is assessed through intensity noise characterization. The intensity noise of a laser arises from a combination of fundamental quantum noise and technical noise sources. Quantum noise originates from intrinsic processes such as the spontaneous emission and the interplay between the gain dynamics and resonator losses [86]. Technical noise sources include excess noise from the pump

[1] Gooch and Housego, I-M110-2C10B6-3-GH26
[2] Thorlabs, SM05PD2B

source or noise from the resonant frequency-doubling stage, mechanical vibrations of the resonator mirrors, and thermal fluctuations within the gain medium, among others [87]. The overall intensity noise spectrum is not solely determined by these sources, but also depends sensitively on the laser operating conditions.

The instantaneous optical power $P(t)$ of a laser can be expressed as the sum of its root-mean-square (RMS) value P_{rms} and power fluctuations of $\delta P(t)$:

$$P(t) = P_{\text{rms}} + \delta P(t). \tag{6.1}$$

To quantify power fluctuations, we use the power spectral density (PSD). In signal processing, the power spectrum $S_{xx}(f)$ describes how a continuous-time signal's power is distributed across frequency components. By Fourier analysis, any signal can be represented as a superposition of frequency components over a continuous range, with some of the power potentially concentrated at discrete frequencies. The PSD gives the statistical average of this power as a function of frequency. The spectrum is discretized into evenly spaced frequency bins, whose width depends on the sampling rate and total number of samples, as given by the Nyquist–Shannon sampling theorem. This theorem states that accurate reconstruction requires the sampling frequency to be at least twice the highest signal frequency [88]. The corresponding Nyquist frequency $f/2$ marks the upper limit of unambiguous representation; higher-frequency components fold back as aliases, distorting the PSD. The lowest resolvable frequency is set by the total acquisition time: $f_{\text{min}} = 1/T_{\text{acq}}$.

The PSD can be defined as a one-sided PSD of only positive frequencies or a two-sided PSD of both positive and negative frequencies. To obtain the PSD, we compute the Fourier transform of the autocorrelation function of $\delta P(t)$. Here, an additional factor of 2 is included to obtain the one-sided PSD:

$$S_{xx}(f) = 2\int_{-\infty}^{+\infty} \langle \delta P(t)\delta P(t+\tau)\rangle \exp\big(i2\pi f\tau\big)d\tau. \tag{6.2}$$

Here, f denotes the noise frequency. In this convention, the units of $S_{xx}(f)$ are V^2/Hz, although it is often reported in logarithmic scale (dBV^2/Hz), computed as $10\log_{10}(S_{xx}(f)/(1\,\text{V}^2))$.

A widely used deduced metric is the relative intensity noise (RIN), which quantifies power fluctuations normalized to the averaged optical power, given by

$$\text{RIN} = \frac{\langle \delta P(t)^2\rangle}{P_{\text{rms}}^2} = \frac{\text{PSD}}{P_{\text{rms}}^2}. \tag{6.3}$$

The units are often reported in dBc/Hz, which is the noise power per hertz relative to the power of a carrier signal. A single number giving a hint on intensity noise is the integrated RIN, which is obtained by integrating the RIN spectrum over the frequency range of interest:

$$\text{Integrated RIN} = \sqrt{\int_{f_{\text{min}}}^{f_{\text{max}}} \text{RIN}(f)\,df}. \tag{6.4}$$

This quantity provides a measure of the RMS laser intensity fluctuations over the specified frequency band.

6.1.2 RIN CHARACTERIZATION

We now proceed to the measurements, in which the RIN was characterized for three different optical powers of the laser: 1 W, 4 W and 8 W, both for the free-running and stabilized case. Since our previous measurements in Ch. 5 were performed at a laser output power of 1 W, it is instructive to examine the RIN at this operating point. The higher powers were included to investigate how the intensity noise scales with increasing optical output, as higher optical powers will be required for future experiments involving larger ion crystals. In order to measure low-noise levels of the RIN from DC to MHz frequencies, fast, low-noise and high-resolution data acquisition of the analog photodiode signals is required. To this end, we use a commercial intensity noise analyzer (Thorlabs, PNA1) with a noise floor under $-140\,\mathrm{dBV^2/Hz}$, a bandwidth from DC to 3 MHz and 18 Bit resolution. We measure the RIN using two photodiodes. On the one hand we use the monitor output of the PI unit, which is the buffered output voltage of the transimpedance amplifier. If the PI controller is running, this measurement reflects the in-loop error signal. As an independent cross-check, an external reference photodiode (Thorlabs, PDA10A1) is used. This model already contains a transimpedance amplifier, i.e. it can be directly connected to the noise analyzer. This measurement is useful to assess if the home-built photodiode (hereafter referred to as the feedback PD[3]) and the amplifier circuit is properly working, and is not introducing additional noise into the system. A setup of the measurement is shown in Fig. 6.2.

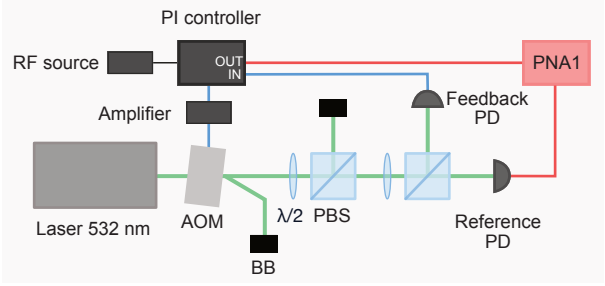

Figure 6.2: **Setup for the characterization of RIN**. The laser power is stabilized using an AOM, connected to a PI controller, as discussed before. Excess light is directed to a beam block using a half-wave plate and a PBS, while the attenuated beam is sent to a second PBS, which divides the power such that each photodiode receives a signal corresponding to 2 V. The reference photodiode is connected directly to the PNA1, whereas for the feedback photodiode, the monitored signal is taken from the output of the PI controller.

The results are presented in Fig. 6.3. Apart from these measurements, background measurements of the intensity noise analyzer and of both photodiodes were performed to identify the noise level of the measurement system. Here, background refers to measurements taken with no light incident on the photodiode. We begin with Fig. 6.3a), which

[3]Thorlabs, SM05PD2B

shows the RIN of the feedback PD. Note that all measurements were referenced to 2 V, corresponding to the output voltage of the feedback PD. The black curve at the bottom corresponds to the background of the PNA1, which is consistent with the manufacturer's specifications. The gray curve represents the background measurement of the feedback PD together with its home-built amplifier. As expected, a low noise level is observed. At higher frequencies around 3 MHz, a rise occurs due to the bandwidth limitation of the transimpedance amplifier, which is anticipated. The upper curves depict the unstabilized measurements: the 1 W unstabilized data in light green, 4 W in pink, and 8 W in teal. All unstabilized measurements exhibit a high noise level at low frequencies between 10 Hz and 100 kHz, which is highly problematic for gate operations. For higher optical powers, a broadband peak around 700 Hz is observed, likely originating from the laser itself. The sharp peaks in the spectra may result from electrical noise in the laboratory environment or from intrinsic laser fluctuations, although this has not been definitively confirmed. The RIN measurements with active stabilization are shown in green (1 W), red (4 W), and light blue (8 W). As desired, a strong reduction of low-frequency noise is observed, with levels decreasing by up to −63 dBc/Hz. At higher frequencies, the servo bump of the PI unit appears around 300 kHz (determined by the bandwidth of the voltage-variable attenuator), leading to an increased noise level of approximately −115 dBc/Hz. Note that tuning the PI parameters could reduce the strength of this servo bump, but this would come at the cost of higher noise at lower frequencies.

Fig. 6.3b) shows the respective curves for the reference photodiode. Note that the noise level of the photodiode (gray curve) is higher than the PNA noise level. This is not unexpected since the PI unit was developed for the stabilization of the RF power for ion traps, which requires extremely low noise levels at the ppm level. The reference photodiode, however, is a standard product from Thorlabs with no particular focus on ultra-low noise. However, apart from residual features from this increased noise level of the reference photodiode, specifically in the range between 10 Hz and 1 kHz, the spectra of the laser noise are pretty much similar to those from the in-loop error signal, i.e. proper functionality of the stabilization system can be confirmed.

As noted above, another relevant quantity is the integrated RIN, shown in Fig. 6.3c) and d) for the feedback and reference photodiodes, respectively. Each data point represents the integral of the RIN spectrum from DC up to the corresponding frequency; thus, the rightmost point of each curve corresponds to the total integrated RIN over the full spectrum. In the free-running case, strong low-frequency noise leads to a rapid increase of the integrated RIN, whereas active power stabilization suppresses this increase up to approximately 100 kHz. At this frequency, the integrated RIN is 0.025 % for 1 W, 0.024 % for 4 W, and 0.024 % for 8 W, compared to values exceeding 0.26 % in the free-running case. At higher frequencies, the integrated RIN increases due to the spectral power contained in the servo bump. This effect is pronounced, resulting in an apparent increase by a factor of roughly 34 when integrated over the full spectrum. This arises from the logarithmic scaling of the frequency axis, which can underestimate the contribution of narrow peaks at high frequencies. Nevertheless, these high-frequency noise components are effectively averaged out for quantum gates with durations of several hundred microseconds.

These results demonstrate that the implemented power stabilization allows for a significant suppression of intensity noise on timescales relevant to the gate operation. Such a reduction is beneficial, as intensity fluctuations during the gate duration can directly degrade quantum gate fidelity. By minimizing these fluctuations, we expect a corresponding improvement in gate performance and overall fidelity, enabling more reliable and precise quantum operations, which will be investigated in upcoming experiments.

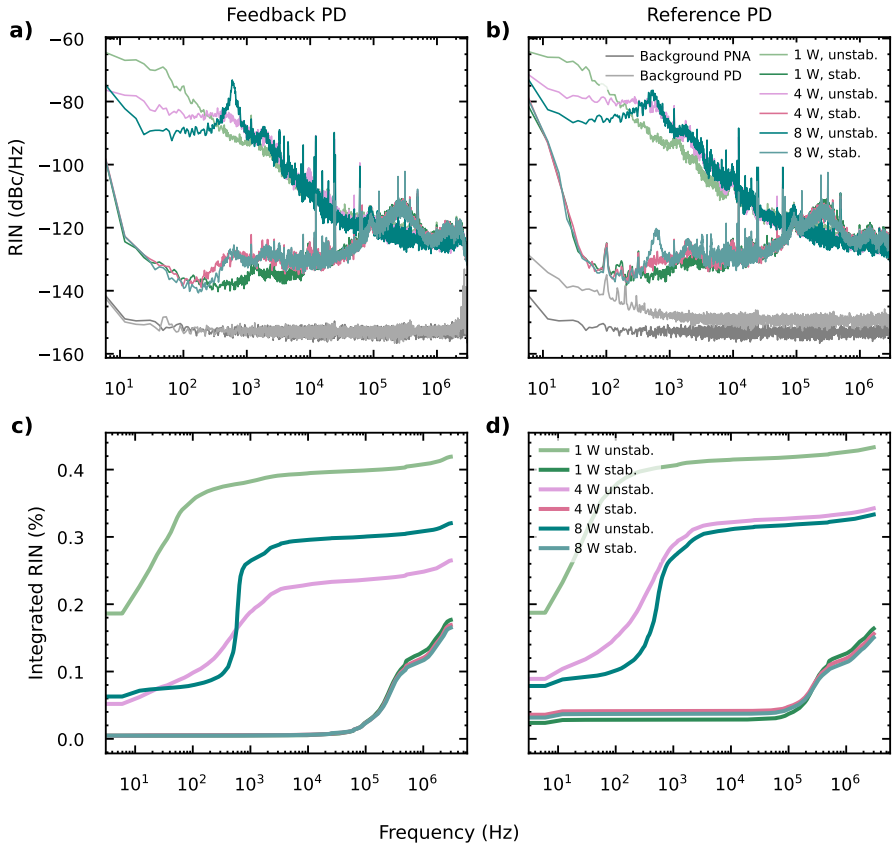

Figure 6.3: **RIN of the free-running and stabilized laser**. In **a)** and **b)**, the RIN is presented for the feedback and reference photodiode, respectively. For each photodiode, the RIN was measured for three optical output powers of the laser: 1 W, 4 W and 8 W, both for the free-running and the stabilized laser. Additionally, the background noise of the intensity noise analyzer and that of the photodiode were recorded. Note that all measurements were referenced to 2 V. In panel **c)** and **d)**, the integrated RIN is depicted for both photodiodes corresponding to all spectra shown in panel **a)** and **b)**.

6.2 FIBER COUPLERS AND FIBERS

Another improvement to the LS gate setup is the implementation of new fiber couplers and fibers designed for high optical power. This section presents the design of the couplers together with supporting optical simulations and discusses the selection of the new fibers.

6.2.1 FIBER COUPLERS

A big problem in the fiber-coupling of high-intensity lasers is dust and aerosols in the air around the fiber facet, which can lead to localized absorption and permanent damage when exposed to high-intensity light [89]. We reduce these effects through the the use of custom-built, sealed fiber couplers that provide a dust-protected environment for the focusing optics and fiber facets. The fiber incoupler and outcoupler are shown in Fig. 6.4a) and b), respectively. Both couplers employ translation mounts with degrees of freedom in

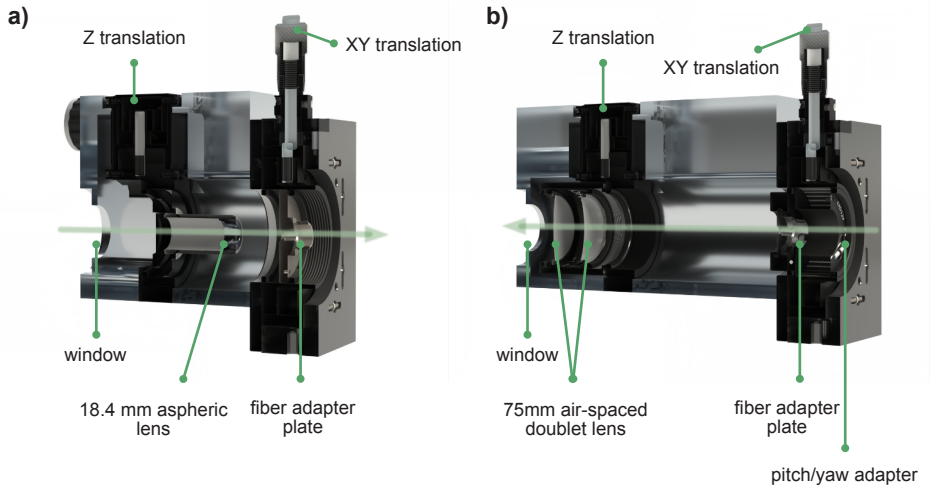

Figure 6.4: **3D rendering of the cross section of the fiber couplers**. The light-green arrow denotes the propagation direction of the laser beam. **a)** shows the fiber incoupler, and **b)** depicts the fiber outcoupler. Both couplers employ translation mounts with degrees of freedom in the XY-plane as well as along the Z-axis, enabling proper alignment for efficient light coupling. The window is not shown in the 3D rendering. The incoupler incorporates an aspheric lens with a focal length of 18.4 mm to adjust the incident beam to the appropriate size (12.2 µm) for coupling into the fiber. The outcoupler employs a 75 mm air-spaced doublet lens to expand the output beam to a diameter of approximately 100 µm at the position of the ions.

the XY-plane[4] as well as along the Z-axis[5], enabling proper alignment of the fiber facet with respect to the focusing lens to achieve efficient fiber-coupling. The outcoupler has the additional possibility for tilt operations[6] of the fiber facet to simultaneously minimize astigmatism and coma, since an abberation-free beam on the ion crystal is desired. Apart from the translation stages, custom-built aluminum parts are manufactured to fit into the cage system between the translation stages. In combination with a wedged window[7]

[4]Thorlabs, ST1XY-A/M
[5]Thorlabs, SM1ZA
[6]Thorlabs, KAD12F
[7]Thorlabs, WW11050-C10

glued on the input/output and Kapton tape covering the remaining gaps, a mostly dust-free environment can be ensured.

The incoupler employs a configuration in which a collimated beam is generated using a separate lens to focus the light. Although this approach is generally not optimal due to the introduction of optical aberrations, these aberrations have a comparatively minor impact on the coupling efficiency in this case. The fiber outcoupler operates as follows: rather than producing a collimated beam and subsequently using a separate lens to focus the light onto the ions, which can introduce aberrations from the additional optical element, we generate a converging beam by positioning the lens close to its focal length to the fiber facet. The outcoupler is then placed at the location where this converging beam reaches its focal spot at the ions. Combined with a high-power air-spaced doublet lens, designed to suppress spherical aberrations, and careful alignment of the fiber facet relative to the lens, this approach produces a beam with minimal aberrations at the position of the ion crystal. To determine suitable optical components and minimize abberations, simulations were performed using Zemax OpticStudio. For the fiber incoupler, the primary objective was to focus the incoming beam to the appropriate spot size of 12.2 µm to match the mode field diameter of the fiber. Based on the simulation results, for the incoupler, an aspheric lens with a focal length of 18.4 mm[8] was selected. Note that these results represent an optimization, and several constraints must be taken into account. The model assumes ideal optical components with perfect surface quality and coating performance. It further requires exact axial distances and perfectly concentric alignment; in practice, even small tilts or lateral displacements can lead to significant increases in aberrations. For the fiber outcoupler, the beam size at the ion position had to match the crystal size of 100 µm. With the simulations, a 75 mm air-spaced doublet lens[9] was selected. Fig. 6.5 shows the aberrations of the fiber outcoupler. All seven Seidel coefficients are plotted for each optical surface, along with the cumulative contributions in the focal plane at a wavelength of 532 nm. The simulations reveal that only spherical aberrations are introduced by the lens surfaces. Since these occur with opposite signs, they largely cancel, leaving only a minimal residual contribution of 33 nm. Furthermore, the Airy disk was simulated as illustrated in Fig. 6.6b), representing the smallest achievable focused spot size. The Airy disk for the fiber outcoupler has a diameter of 104.6 µm. For the incoupler, the Seidel coefficients showed a total contribution of 0.02 nm and an Airy disk of 14.7 µm. For both, the in- and out-coupler, the simulated spot lies well within the Airy disk, thus confirming operation near the diffraction limit with minimal aberrations.

Before final assembly, all custom-built components were cleaned in an ultrasonic bath to remove residual oil and dust from their surfaces. Finally, the fiber couplers were sealed with Kapton tape to prevent contamination from entering the assemblies.

6.2.2 FIBERS

Special attention is given to managing the high optical power densities present in the system, which pose a significant risk of damaging optical components, particularly the

[8] Thorlabs, C280TMD-A
[9] Thorlabs, ACA254-075-532

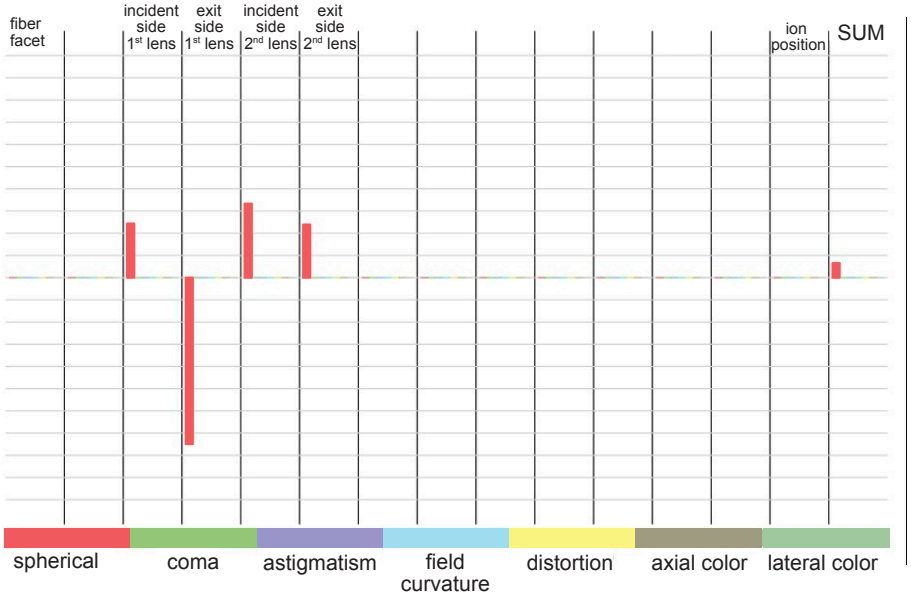

Figure 6.5: **Aberrations in the fiber outcoupler**. Aberrations of the fiber outcoupler were analyzed in Zemax OpticStudio. All seven Seidel coefficients are shown for each surface, along with their cumulative contribution in the focal plane. The fiber outcoupler employs an air-spaced doublet lens. Each surface of the doublet introduces spherical aberrations of opposite signs, which largely cancel, leaving only a small residual contribution.

facets of optical fibers. To mitigate this risk, high-power photonic crystal fibers (PCF)[10] will be employed. These contain a regular pattern of microscopic air channels along its length, enabling a unique guiding mechanism and tailorable optical properties. These fibers exhibit several important advantages [90]. First, they support single-mode behaviour in conjunction with large mode areas. As an example: the PCF we use has a mode field diameter of 12.2 µm compared to a standard single-mode fiber for 532 nm with a mode field diameter of 3.3 µm. This results in smaller power densities on the facet and in the fiber core, which reduces the likelihood for power-induced damage. In addition, PCF employ an end-capped design, which reduces the optical intensity at the air-glass interface, thereby lowering the risk of facet damage. Finally, the presence of an air-gapped connector helps to minimize losses in the surrounding ceramic as well as in the glue. This allows for transmission of powers of up to 20 W per fiber (3 m length), which is sufficient even for big ion crystals.

Furthermore, we will significantly reduce the fiber length from its current length of 10 m down to 3 m to improve the phase-stability of the interferometer on short time scales. Such stability is important, since phase noise of the interferometer directly translates into fluctuations of the standing-wave phase at the ions (apart from the fact that longer fibers become problematic at these power levels due to the onset of stimulated Brillouin scattering). This directly affects the final phase of the entangled state. As a result, the gate

[10] NKT Photonics, AEROGUIDE-15-PM

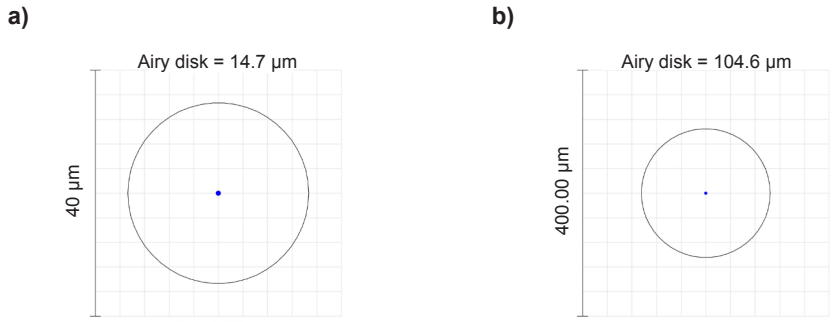

Figure 6.6: **Simulated spot sizes**. The spot sizes of the fiber incoupler and outcoupler were simulated in Zemax OpticStudio. **a)** shows the fiber incoupler, with an Airy disk diameter of 14.7 µm. The Airy disk represents the smallest achievable focused spot size for the given wavelength and aperture. The simulated spot lies well within this limit, indicating operation close to the diffraction limit. **b)** shows the fiber outcoupler, where the Airy disk diameter is 104.6 µm. Here too, the simulated spot remains well within the Airy disk, confirming almost diffraction-limited performance with minimal aberrations.

fidelity would be reduced if the phase stability were not maintained. Relocating the laser system closer to the ion trap is expected to enhance the stability of the interferometer and, consequently, improve the gate fidelity.

7

SUMMARY AND OUTLOOK

The central achievement of this thesis has been the successful implementation of light-shift gates within a two-dimensional trapped-ion quantum simulator, enabling two-qubit entangling gates and in the future potentially global ZZ interactions. These gates provide the capability to selectively entangle arbitrary pairs of ions, an essential prerequisite for preparing tailored input states adapted to the Hamiltonian under investigation. This advancement broadens the scope of quantum simulations that can be realized and enhances the overall versatility of the simulator and programmability. To realize this operation, individually addressed 729 nm laser beams are used to transfer selected ions from the ground-state qubit manifold to an optical qubit state. The entangling interaction is then mediated by a global 532 nm laser, which is far detuned from any electronic transition of the $^{40}Ca^{+}$ ion. This large detuning suppresses photon scattering, allowing for the implementation of high-fidelity entangling gates.

To assess the feasibility of the gate implementation, simulations of the AC Stark shift and photon scattering rate were conducted. From this, the expected gate durations and associated errors were estimated, providing a quantitative framework for evaluation and enabling direct comparison between experimental observations and theoretical predictions. On the experimental side, an optical setup for a laser at 532 nm has been constructed to implement the light-shift gates. The beam is divided into two paths using polarizing beam splitters. Each path is independently controlled in frequency, amplitude, and phase via a dedicated acousto-optic modulator, enabling the generation of a moving standing wave. Using this setup, we first measured the beam size and the AC Stark shift for the optical qubit. There we found an offset between experiment and simulation of about 25 kHz. While partial deviations may be attributed to reflection losses at the vacuum viewport, these losses alone are insufficient to account for the full deviation. Therefore, further investigation is required. For the following measurements, we instead considered the relative differences between transitions. This was characterized for the optical qubit, where we found good agreement between experiment and simulation up to deviations of 2.6 %. In case of the metastable qubit, larger deviations of about 15 % are observed. We showed that these deviations can be partly attributed to polarization imperfections.

Introducing a slight ellipticity in the simulations of 4.9 % for light-shift beam 1 and 13.3 % for light-shift beam 2, we can reduce these deviations to within 0.7 %. However, for transitions, which employ the $\Delta m_{DD} = -1$ transition, we observed deviations by a factor of two. It is likely that the atomic-physics model employed in the simulations does not fully account for the $D_{5/2}$ states, though further study is necessary to ascertain the extent of its failure. Furthermore, measurements of the ground-state qubit manifold were performed. As expected from the large detuning relative to the fine structure of the P orbital and the use of linearly polarized light, was found to effectively cancel. This capability is required for the subsequent implementation of the light-shift gates. In that protocol, a 729 nm laser is used to transfer two selected qubits into the optical qubit manifold, while the other ions remain in the ground-state. A global 532 nm beam is then applied to entangle only the selected ions. It is therefore important that the 532 nm light does not induce unwanted Stark shifts on the ground-state qubit manifold.

Another central parameter in the implementation of light-shift gates is the optical dipole force, which allows for coupling between the ions' internal states and their collective motion. To characterize this coupling, the effect of coherent displacements of the motional state induced by a light-shift pulse for different electronic states was investigated. In these experiments, the parameters of the optical dipole force were set to allow for resonant excitation of the mode, which gives rise to a coherent displacement. From this, we extracted phonon distributions for comparison with theoretical predictions. Measurements were performed for three different initial states. For the $S_{1/2}, m_j = -1/2$ motional ground state, the experimentally measured displacements closely matched the theoretical predictions, with a deviation of 0.5 %. In contrast, for the $D_{5/2}, m_j = -1/2$ and $D_{5/2}, m_j = -5/2$ states, deviations of a factor 1.6 were observed. As in the case for the AC Stark shifts, it is likely that the atomic physics model used in the simulations is not fully capturing the $D_{5/2}$ states, although this needs further investigation. To further advance toward the implementation of the light-shift gate, which relies on off-resonant excitation of a motional mode such that the motional state follows a closed trajectory in phase space, we investigated this regime by detuning the light-shift beams from the center-of-mass mode. By determining the displacement amplitude from the decay and revival of the excitation-probability contrast, we observed good agreement with theoretical predictions, with deviations of up to 4.6 %. The consistency between experiment and theory in these measurements is crucial, as it validates our understanding of the optical dipole force-mediated coupling mechanism and confirms the control of motional displacements. These elements are prerequisites for attaining light-shift gate operations.

Finally, the light-shift gate was implemented and characterized. In a two-ion crystal, we achieved a gate fidelity of 99.0(8) %. Simulations predict a theoretical upper limit of 99.96 %, indicating that residual errors are primarily of technical origin. The dominant error sources are most likely laser-intensity fluctuations, which lead to variations in the AC Stark shift and thereby degrade the population contrast. Another relevant contribution possibly is the interferometric instability introduced by the 10 m optical fibers connecting the laser system to the trap, which can perturb the final phase of the entangled state. Environmental perturbations along these fibers, such as temperature drifts and mechanical

vibrations, lead to phase noise and reduced gate fidelity. As described below, some of these issues will be addressed in a revised version of the setup. To investigate scalability, the gate was implemented in a ten-ion crystal by addressing two central ions with the 729 nm beam while applying the light-shift beam globally. A fidelity of 78.6(10) % was obtained, representing, to our knowledge, the first demonstration of a light-shift gate in a ten-ion system in such a configuration. The reduced fidelity arises from the denser motional spectrum and increased susceptibility to off-resonant couplings, mode crosstalk, and dephasing, compounded by technical noise sources such as intensity fluctuations and polarization imperfections, some of them are more critical for larger ion numbers.

The thesis is concluded with a chapter describing a revised version of the setup to address some of the issues limiting the gate fidelity. First, active laser intensity stabilization was implemented using a single-pass acousto-optical modulator placed after the laser head. A photodiode monitors the output intensity and provides feedback to a custom PI controller that regulates the acousto-optical modulator's radio-frequency drive. We demonstrated noise suppression in a frequency range of 10 Hz to 50 kHz, relevant to the employed gate durations of around 500 µs. Within this band, the noise can be reduced between 8 dBc/Hz and 63 dBc/Hz, representing a sufficient improvement. The effect of the improved stability will be tested on the ion crystals in future experiments. Furthermore, additional improvements are anticipated from replacing the current 10 m optical fibers with shorter 3 m ones and by positioning the laser system closer to the ion trap, both of which will enhance interferometric stability and further benefit the achievable gate fidelity. To cope with higher powers, which are required for bigger ion crystals beyond 10 ions, the fiber handling was improved in terms of employing high-power photonic crystal fibers as well as home-built shielded fiber couplers.

With these technical upgrades in place, the next step will be to systematically evaluate their impact on gate stability and performance. Under the improved experimental conditions, featuring active laser power stabilization and reduced fiber lengths, the light-shift gates will be re-characterized to quantify the achieved gains in fidelity and robustness. These improvements will enable more systematic benchmarking of light-shift gates and provide deeper insight into the remaining error sources and the ultimate fidelity limits attainable in the current setup. Future studies will also explore the implementation of higher optical powers to extend light-shift gate operations to larger ion crystals, investigating entangling gates between arbitrary ion pairs. On the simulation side, it is interesting to use the global ZZ interaction in combination with the existing XX and XY interaction to explore more complex spin models or to extend the toolbox of interaction models with the goal of performing variational quantum simulation experiments.

BIBLIOGRAPHY

[1] A. Einstein, "On the Quantum Theory of Radiation," *Phys. Z.*, vol. 18, no. 121, pp. 167–183, 1917.

[2] A. L. Schawlow and C. H. Townes, "Infrared and Optical Masers," *Phys. Rev.*, vol. 112, no. 6, pp. 1940–1949, 1958. DOI: 10.1103/PhysRev.112.1940.

[3] T. H. Maiman, "Stimulated Optical Radiation in Ruby," *Nature*, vol. 187, pp. 493–494, 1960. DOI: 10.1038/187493a0.

[4] M. A. Nielsen and I. L. Chuang, *Quantum Computation and Quantum Information*. Cambridge University Press, 2000. DOI: 10.1017/CBO9780511976667.

[5] J. P. Dowling and G. J. Milburn, "Quantum technology: The second quantum revolution," *Philos. Trans. R. Soc. A*, vol. 361, pp. 1655–1674, 2003. DOI: 10.1098/rsta.2003.1227.

[6] I. M. Georgescu, S. Ashhab, and F. Nori, "Quantum simulation," *Rev. of Mod. Phys.*, vol. 86, no. 1, pp. 153–185, 2014. DOI: 10.1103/RevModPhys.86.153.

[7] J. Preskill, "Quantum computing and the entanglement frontier," *arXiv*, vol. 1203.5813, 2012. DOI: 10.48550/arXiv.1203.5813.

[8] S. Ghosh, A. Deshpande, D. Hangleiter, A. V. Gorshkov, and B. Fefferman, "Complexity Phase Transitions Generated by Entanglement," *Phys. Rev. Lett.*, vol. 131, no. 030601, 2023. DOI: 10.1103/PhysRevLett.131.030601.

[9] R. P. Feynman, "Simulating Physics with Computers," *Int. J. Theor. Phys.*, vol. 21, no. 6/7, pp. 467–488, 1982. DOI: 10.1007/BF02650179.

[10] D. P. DiVincenzo, "The Physical Implementation of Quantum Computation," *Fortschr. Phys.*, vol. 48, no. 9-11, pp. 771–783, 2000. DOI: 10.1002/1521-3978(200009)48:9/11<771::AID-PROP771>3.0.CO;2-E.

[11] J. I. Cirac and P. Zoller, "Quantum Computations with Cold Trapped Ions," *Phys. Rev. Lett.*, vol. 74, no. 20, pp. 4091–4094, 1995. DOI: 10.1103/PhysRevLett.74.4091.

[12] R. Blatt and C. F. Roos, "Quantum simulations with trapped ions," *Nature Physics*, vol. 8, pp. 277–284, 2012. DOI: 10.1038/nphys2252.

[13] C. D. Marciniak, T. Feldker, I. Pogorelov, R. Kaubruegger, D. V. Vasilyev, R. van Bijnen, P. Schindler, P. Zoller, R. Blatt, and T. Monz, "Optimal metrology with programmable quantum sensors," *Nature*, vol. 603, pp. 604–609, 2022. DOI: 10.1038/s41586-022-04435-4.

[14] C. Monroe, W. C. Campbell, L. M. Duan, Z. X. Gong, A. V. Gorshkov, P. W. Hess, R. Islam, K. Kim, N. M. Linke, G. Pagano, P. Richerme, C. Senko, and N. Y. Yao, "Programmable quantum simulations of spin systems with trapped ions," *Rev. Mod. Phys.*, vol. 93, no. 025001, 2021. DOI: 10.1103/RevModPhys.93.025001.

[15] L. Postler, S. Heuβen, I. Pogorelov, M. Rispler, T. Feldker, M. Meth, C. D. Marciniak, R. Stricker, M. Ringbauer, R. Blatt, P. Schindler, M. Müller, and T. Monz, "Demonstration of fault-tolerant universal quantum gate operations," *Nature*, vol. 605, pp. 675–680, 2022. DOI: 10.1038/s41586-022-04721-1.

[16] C. Figgatt, A. Ostrander, N. M. Linke, K. A. Landsman, D. Zhu, D. Maslov, and C. Monroe, "Parallel entangling operations on a universal ion-trap quantum computer," *Nature*, vol. 572, pp. 368–372, 2019. DOI: 10.1038/s41586-019-1427-5.

[17] M. Meth, J. Zhang, J. F. Haase, C. Edmunds, L. Postler, A. J. Jena, A. Steiner, L. Dellantonio, R. Blatt, P. Zoller, T. Monz, P. Schindler, C. Muschik, and M. Ringbauer, "Simulating two-dimensional lattice gauge theories on a qudit quantum computer," *Nature Physics*, vol. 21, pp. 570–576, 2025. DOI: 10.1038/s41567-025-02797-w.

[18] M. K. Joshi, F. Kranzl, A. Schuckert, I. Lovas, C. Maier, R. Blatt, M. Knap, and C. F. Roos, "Observing emergent hydrodynamics in a long-range quantum magnet," *Science*, vol. 376, pp. 720–724, 2022. DOI: 10.1126/science.abk2400.

[19] B. W. Li, Y. K. Wu, Q. X. Mei, R. Yao, W. Q. Lian, M. L. Cai, Y. Wang, B. X. Qi, L. Yao, L. He, Z. C. Zhou, and L. M. Duan, "Probing Critical Behavior of Long-Range Transverse-Field Ising Model through Quantum Kibble-Zurek Mechanism," *PRX Quantum*, vol. 4, no. 010302, 2023. DOI: 10.1103/PRXQuantum.4.010302.

[20] J. Zhang, G. Pagano, P. W. Hess, A. Kyprianidis, P. Becker, H. Kaplan, A. V. Gorshkov, Z. X. Gong, and C. Monroe, "Observation of a many-body dynamical phase transition with a 53-qubit quantum simulator," *Nature*, vol. 551, pp. 601–604, 2017. DOI: 10.1038/nature24654.

[21] S. A. Guo, Y. K. Wu, J. Ye, L. Zhang, W. Q. Lian, R. Yao, Y. Wang, R. Y. Yan, Y. J. Yi, Y. L. Xu, B. W. Li, Y. H. Hou, Y. Z. Xu, W. X. Guo, C. Zhang, B. X. Qi, Z. C. Zhou, L. He, and L. M. Duan, "A site-resolved two-dimensional quantum simulator with hundreds of trapped ions," *Nature*, vol. 630, pp. 613–618, 2024. DOI: 10.1038/s41586-024-07459-0.

[22] C. Kokail, C. Maier, R. van Bijnen, T. Brydges, M. K. Joshi, P. Jurcevic, C. A. Muschik, P. Silvi, R. Blatt, C. F. Roos, and P. Zoller, "Self-verifying variational quantum simulation of lattice models," *Nature*, vol. 569, pp. 355–360, 2019. DOI: 10.1038/s41586-019-1177-4.

[23] D. Kiesenhofer, H. Hainzer, A. Zhdanov, P. C. Holz, M. Bock, T. Ollikainen, and C. F. Roos, "Controlling Two-Dimensional Coulomb Crystals of More Than 100 Ions in a Monolithic Radio-Frequency Trap," *PRX Quantum*, vol. 4, no. 020317, 2023. DOI: 10.1103/PRXQuantum.4.020317.

[24] C. Maier, T. Brydges, P. Jurcevic, N. Trautmann, C. Hempel, B. P. Lanyon, P. Hauke, R. Blatt, and C. F. Roos, "Environment-Assisted Quantum Transport in a 10-qubit Network," *Phys. Rev. Lett.*, vol. 122, no. 050501, 2019. DOI: 10.1103/PhysRevLett.122.050501.

[25] A. M. Polloreno, A. M. Rey, and J. J. Bollinger, "Individual qubit addressing of rotating ion crystals in a Penning trap," *Phys. Rev. Res.*, vol. 4, no. 033076, 2022. DOI: 10.1103/PhysRevResearch.4.033076.

[26] B. J. McMahon, K. R. Brown, C. D. Herold, and B. C. Sawyer, "Individual-Ion Addressing and Readout in a Penning Trap," *Phys. Rev. Lett.*, vol. 133, no. 173201, 2024. DOI: 10.1103/PhysRevLett.133.173201.

[27] F. Kranzl, M. K. Joshi, C. Maier, T. Brydges, J. Franke, R. Blatt, and C. F. Roos, "Controlling long ion strings for quantum simulation and precision measurements," *Phys. Rev. A*, vol. 105, no. 052426, 2022. DOI: 10.1103/PhysRevA.105.052426.

[28] A. Sørensen and K. Mølmer, "Quantum Computation with Ions in Thermal Motion," *Phys. Rev. Lett.*, vol. 82, no. 9, pp. 1971–1974, 1999. DOI: 10.1103/PhysRevLett.82.1971.

[29] A. Sørensen and K. Mølmer, "Entanglement and quantum computation with ions in thermal motion," *Phys. Rev. A*, vol. 62, no. 022311, 2000. DOI: 10.1103/PhysRevA.62.022311.

[30] G. J. Milburn, S. Schneider, and D. F. James, "Ion trap quantum computing with warm ions," *Fortschr. Phys.*, vol. 48, no. 9-11, pp. 801–810, 2000. DOI: 10.1002/1521-3978(200009)48:9/11<801::AID-PROP801>3.0.CO;2-1.

[31] X. Wang, A. Sørensen, and K. Mølmer, "Multibit gates for quantum computing," *Phys. Rev. Lett.*, vol. 86, no. 17, pp. 3907–3910, 2001. DOI: 10.1103/PhysRevLett.86.3907.

[32] D. Leibfried, R. Blatt, C. Monroe, and D. Wineland, "Quantum dynamics of single trapped ions," *Rev. of Mod. Phys.*, vol. 75, pp. 281–324, 2003. DOI: 10.1103/RevModPhys.75.281.

[33] B. C. Sawyer and K. R. Brown, "Wavelength-insensitive, multispecies entangling gate for group-2 atomic ions," *Phys. Rev. A*, vol. 103, no. 022427, 2021. DOI: 10.1103/PhysRevA.103.022427.

[34] C. R. Clark, H. N. Tinkey, B. C. Sawyer, A. M. Meier, K. A. Burkhardt, C. M. Seck, C. M. Shappert, N. D. Guise, C. E. Volin, S. D. Fallek, H. T. Hayden, W. G. Rellergert, and K. R. Brown, "High-Fidelity Bell-State Preparation with Optical Qubits," *Phys. Rev. Lett.*, vol. 127, no. 130505, 2021. DOI: 10.1103/PhysRevLett.127.130505.

[35] M. Saffman, "Quantum computing with atomic qubits and Rydberg interactions: Progress and challenges," *J. Phys. B: At. Mol. Opt. Phys.*, vol. 49, no. 202001, 2016. DOI: 10.1088/0953-4075/49/20/202001.

[36] M. Foss-Feig, G. Pagano, A. C. Potter, and N. Y. Yao, "Progress in Trapped-Ion Quantum Simulation," *Annu. Rev. Condens. Matter Phys.*, vol. 16, pp. 145–172, 2025. DOI: 10.1146/annurev-conmatphys-032822-045619.

[37] A. Chatterjee, P. Stevenson, S. De Franceschi, A. Morello, N. de Leon, and F. Kuemmeth, "Semiconductor Qubits In Practice," *Nat. Rev. Phys.*, vol. 3, pp. 157–177, 2021. DOI: 10.1038/s42254-021-00283-9.

[38] C. Couteau, S. Barz, T. Durt, T. Gerrits, J. Huwer, R. Prevedel, J. Rarity, A. Shields, and G. Weihs, "Applications of single photons to quantum communication and computing," *Nat. Rev. Phys.*, vol. 5, pp. 326–338, 2023. DOI: 10.1038/s42254-023-00583-2.

[39] W. Paul, "Electromagnetic traps for charged and neutral particles," *Rev. of Mod. Phys.*, vol. 62, no. 3, pp. 531–540, 1990. DOI: 10.1103/RevModPhys.62.531.

[40] R. Lechner, C. Maier, C. Hempel, P. Jurcevic, B. P. Lanyon, T. Monz, M. Brownnutt, R. Blatt, and C. F. Roos, "EIT ground-state cooling of long ion strings," *Phys. Rev. A*, vol. 93, no. 053401, 2016. DOI: 10.1103/PhysRevA.93.053401.

[41] G. Morigi, J. Eschner, and C. H. Keitel, "Ground State Laser Cooling Using Electromagnetically Induced Transparency," *Phys. Rev. Lett.*, vol. 85, no. 21, pp. 4458–4461, 2000. DOI: 10.1103/PhysRevLett.85.4458.

[42] E. D. Courant and H. S. Snyder, "Theory of the Alternating-Gradient Synchrotron," *Ann. Phys.*, vol. 281, pp. 360–408, 2000. DOI: 10.1006/aphy.2000.6012.

[43] N. W. McLachlan, *Theory and Application of Mathieu Functions*, 1st ed. Oxford: Clarendon-Press, 1947.

[44] H. Hainzer, "Quantum Correlations of Large Planar Ion Crystals in a Novel Monolithic Radiofrequency Trap," Ph.D. dissertation, Leopold-Franzens University of Innsbruck, 2024.

[45] D. Kiesenhofer, "Control of two-dimensional ion crystals in a radio-frequency trap for quantum simulation," Ph.D. dissertation, Leopold-Franzens University of Innsbruck, 2025.

[46] E. Ising, "Beitrag zur Theorie des Ferromagnetismus," *Z. Physik*, vol. 31, pp. 253–258, 1925. DOI: 10.1007/BF02980577.

[47] E. Lieb, T. Schultz, and D. Mattis, "Two Soluble Models of an Antiferromagnetic Chain," *Ann. Phys.*, vol. 16, pp. 407–466, 1961. DOI: 10.1016/0003-4916(61)90115-4.

[48] C. J. Foot, *Atomic Physics*. Oxford University Press, 2005.

[49] S. H. Autler and C. H. Townes, "Stark Effect in Rapidly Varying Fields," *Phys. Rev.*, vol. 100, no. 2, pp. 703–722, 1955. DOI: 10.1103/PhysRev.100.703.

[50] D. F. James, "Quantum computation with hot and cold ions: An assessment of proposed schemes," *Fortschr. Phys.*, vol. 48, no. 9-11, pp. 823–837, 2000. DOI: 10.1002/1521-3978(200009)48:9/11<823::AID-PROP823>3.0.CO;2-M.

[51] D. Budker, D. F. Kimball, and D. P. DeMille, *Atomic Physics: An Exploration through Problems and Solutions*. Oxford University Press, 2004. DOI: 10/p9dz.

[52] J. T. M. Walraven, "Atomic Physics lectures," University of Amsterdam, Tech. Rep., 2024.

[53] R. J. Glauber, "Coherent and Incoherent States of the Radiation Field," *Phys. Rev.*, vol. 131, no. 6, pp. 2766–2788, 1963. DOI: 10.1103/PhysRev.131.2766.

[54] V. M. Schäfer, A. C. Hughes, O. Bazavan, K. Thirumalai, G. Pagano, C. J. Ballance, and D. M. Lucas, "Comparison of trapped-ion entangling gate mechanisms for mixed species," *arXiv*, vol. 2509.17893, 2025. DOI: 10.48550/arXiv.2509.17893.

[55] L. Aolita, K. Kim, J. Benhelm, C. F. Roos, and H. Häffner, "High-fidelity ion-trap quantum computing with hyperfine clock states," *Phys. Rev. A*, vol. 76, no. 040303, 2007. DOI: 10.1103/PhysRevA.76.040303.

[56] C. H. Baldwin, B. J. Bjork, M. Foss-Feig, J. P. Gaebler, D. Hayes, M. G. Kokish, C. Langer, J. A. Sedlacek, D. Stack, and G. Vittorini, "High-fidelity light-shift gate for clock-state qubits," *Phys. Rev. A*, vol. 103, no. 012603, 2021. DOI: 10.1103/PhysRevA.103.012603.

[57] C. J. Ballance, T. P. Harty, N. M. Linke, M. A. Sepiol, and D. M. Lucas, "High-Fidelity Quantum Logic Gates Using Trapped-Ion Hyperfine Qubits," *Phys. Rev. Lett.*, vol. 117, no. 060504, 2016. DOI: 10.1103/PhysRevLett.117.060504.

[58] D. Leibfried, B. DeMarco, V. Meyer, D. Lucas, M. Barrett, J. Britton, W. M. Itano, B. Jelenković, C. Langer, T. Rosenband, and D. J. Wineland, "Experimental demonstration of a robust, high-fidelity geometric two ion-qubit phase gate," *Nature*, vol. 422, 2003. DOI: 10.1038/nature01492.

[59] V. M. Schäfer, C. J. Ballance, K. Thirumalai, L. J. Stephenson, T. G. Ballance, A. M. Steane, and D. M. Lucas, "Fast quantum logic gates with trapped-ion qubits," *Nature*, vol. 555, pp. 75–78, Feb. 2018, ISSN: 14764687. DOI: 10.1038/nature25737.

[60] J. P. Gaebler, T. R. Tan, Y. Lin, Y. Wan, R. Bowler, A. C. Keith, S. Glancy, K. Coakley, E. Knill, D. Leibfried, and D. J. Wineland, "High-Fidelity Universal Gate Set for $^{9}Be^{+}$ Ion Qubits," *Phys. Rev. Lett.*, vol. 117, no. 060505, 2016. DOI: 10.1103/PhysRevLett.117.060505.

[61] M. V. Berry, "Quantal phase factors accompanying adiabatic changes," *Proc. R. Soc. A*, vol. 392, pp. 45–57, 1984. DOI: 10.1098/rspa.1984.0023.

[62] C. J. Ballance, "High-Fidelity Quantum Logic in Ca^{+}," Ph.D. dissertation, University of Oxford, 2017. DOI: 10.1007/978-3-319-68216-7.

[63] R. Ozeri, "The trapped-ion qubit tool box," *Contemp. Phys.*, vol. 52, no. 6, pp. 531–550, 2011. DOI: 10.1080/00107514.2011.603578.

[64] C. F. Roos, "Ion trap quantum gates with amplitude-modulated laser beams," *New J. Phys.*, vol. 10, no. 013002, 2008. DOI: 10.1088/1367-2630/10/1/013002.

[65] J. Benhelm, G. Kirchmair, C. F. Roos, and R. Blatt, "Towards fault-tolerant quantum computing with trapped ions," *Nature Physics*, vol. 4, pp. 463–466, 2008. DOI: 10.1038/nphys961.

[66] E. Nielsen, J. K. Gamble, K. Rudinger, T. Scholten, K. Young, and R. Blume-Kohout, "Gate Set Tomography," *Quantum*, vol. 5, no. 557, 2021. DOI: 10.22331/q-2021-10-05-557.

[67] I. L. Chuang and M. A. Nielsen, "Prescription for experimental determination of the dynamics of a quantum black box," *J. Mod. Opt.*, vol. 44, no. 11-12, pp. 2455–2467, 1996. DOI: 10.1080/09500349708231894.

[68] E. Knill, D. Leibfried, R. Reichle, J. Britton, R. B. Blakestad, J. D. Jost, C. Langer, R. Ozeri, S. Seidelin, and D. J. Wineland, "Randomized benchmarking of quantum gates," *Phys. Rev. A*, vol. 77, no. 012307, 2008. DOI: 10.1103/PhysRevA.77.012307.

[69] C. A. Sackett, D. Kielpinski, B. E. King, C. Langer, V. Meyer, C. J. Myatt, M. Rowe, Q. A. Turchette, W. M. Itano, D. J. Wineland, and C. Monroe, "Experimental entanglement of four particles," *Nature*, vol. 404, pp. 256–259, 2000. DOI: 10.1038/35005011.

[70] J. J. Bollinger, W. M. Itano, D. J. Wineland, and D. J. Heinzen, "Optimal frequency measurements with maximally correlated states," *Phys. Rev. A*, vol. 54, no. 6, R4649–R4652, 1996. DOI: 10.1103/PhysRevA.54.R4649.

[71] M. Bock, "Polarization-Preserving Quantum Frequency Conversion for Trapped-Atom based Quantum Networks," Ph.D. dissertation, Universität des Saarlandes, 2020. DOI: 10.22028/D291-35322.

[72] M. Ježek, J. Fiurášek, and Z. Hradil, "Quantum inference of states and processes," *Phys. Rev. A*, vol. 68, no. 012305, p. 7, 2003. DOI: 10.1103/PhysRevA.68.012305.

[73] J. B. Altepeter, E. R. Jeffrey, and P. G. Kwiat, "Photonic State Tomography," *Adv. At. Mol. Opt. Phys.*, vol. 52, pp. 105–159, 2005. DOI: 10.1016/S1049-250X(05)52003-2.

[74] R. Loudon, *The Quantum Theory of Light*, 3rd ed. Oxford University Press, 2000. DOI: 10.1093/oso/9780198501770.001.0001.

[75] H. Uys, M. J. Biercuk, A. P. Vandevender, C. Ospelkaus, D. Meiser, R. Ozeri, and J. J. Bollinger, "Decoherence due to elastic Rayleigh scattering," *Phys. Rev. Lett.*, vol. 105, no. 200401, 2010. DOI: 10.1103/PhysRevLett.105.200401.

[76] R. J. Hendricks, D. M. Grant, P. F. Herskind, A. Dantan, and M. Drewsen, "An all-optical ion-loading technique for scalable microtrap architectures," *Appl. Phys. B*, vol. 88, no. 4, pp. 507–513, 2007. DOI: 10.1007/s00340-007-2698-3.

[77] R. Lechner, C. Maier, C. Hempel, P. Jurcevic, B. P. Lanyon, T. Monz, M. Brownnutt, R. Blatt, and C. F. Roos, "Electromagnetically-induced-transparency ground-state cooling of long ion strings," *Phys. Rev. A*, vol. 93, no. 053401, 2016. DOI: 10.1103/PhysRevA.93.053401.

[78] W. Nagourney, J. Sandberg, and H. Dehmelt, "Shelved Optical Electron Amplifier: Observation of Quantum Jumps," *Phys. Rev. Lett.*, vol. 56, no. 26, pp. 2797–2799, 1986. DOI: 10.1103/PhysRevLett.56.2797.

[79] H. Häffner, S. Gulde, M. Riebe, G. Lancaster, C. Becher, J. Eschner, F. Schmidt-Kaler, and R. Blatt, "Precision Measurement and Compensation of Optical Stark Shifts for an Ion-Trap Quantum Processor," *Phys. Rev. Lett.*, vol. 90, no. 143602, 2003. DOI: 10.1103/PhysRevLett.90.143602.

[80] L. D. Brown, T. T. Cai, and A. DasGupta, "Interval Estimation for a Binomial Proportion," *Stat. Sci.*, vol. 16, no. 2, pp. 101–133, 2001. DOI: 10.1214/ss/1009213286.

[81] D. M. Meekhof, C. Monroe, B. E. King, W. M. Itano, and D. J. Wineland, "Generation of Nonclassical Motional States of a Trapped Atom," *Phys. Rev. Lett.*, vol. 76, no. 11, pp. 1796–1799, 1996. DOI: 10.1103/PhysRevLett.76.1796.

[82] J. H. Eberly, N. B. Narozhny, and J. J. Sanchez-Mondragon, "Periodic Spontaneous Collapse and Revival in a Simple Quantum Model," *Phys. Rev. Lett.*, vol. 44, no. 20, pp. 1323–1326, 1980. DOI: 10.1103/PhysRevLett.44.1323.

[83] B. W. Shore and P. L. Knight, "The Jaynes–Cummings model," *J. Mod. Opt.*, vol. 40, no. 7, pp. 1195–1238, 1993. DOI: 10.1080/09500349314551321.

[84] U. Poschinger, A. Walther, K. Singer, and F. Schmidt-Kaler, "Observing the phase space trajectory of an entangled matter wave packet," *Phys. Rev. Lett.*, vol. 105, no. 263602, 2010. DOI: 10.1103/PhysRevLett.105.263602.

[85] T. Choi, S. Debnath, T. A. Manning, C. Figgatt, Z.-X. Gong, L.-M. Duan, and C. Monroe, "Optimal Quantum Control of Multimode Couplings between Trapped Ion Qubits for Scalable Entanglement," *Phys. Rev. Lett.*, vol. 112, no. 190502, 2014. DOI: 10.1103/PhysRevLett.112.190502.

[86] C. H. Henry and R. F. Kazarinov, "Quantum noise in photonics," *Rev. Mod. Phys.*, vol. 68, no. 3, pp. 801–853, 1996. DOI: 10.1103/RevModPhys.68.801.

[87] R. Paschotta, *Intensity Noise*, RP Photonics Encyclopedia, Available online at https://www.rp-photonics.com/intensity_noise.html, Accessed: 2025-08-02.

[88] C. E. Shannon, "Communication in the Presence of Noise," *Proc. IEEE*, vol. 86, no. 2, pp. 447–457, 1998. DOI: 10.1109/JRPROC.1949.232969.

[89] M. Fujiwara, K. Toubaru, and S. Takeuchi, "Optical transmittance degradation in tapered fibers," *Opt. Express*, vol. 19, no. 9, 2011. DOI: 10.1364/OE.19.008596.

[90] P. S. J. Russell, "Photonic-crystal fibers," *J. Light. Technol.*, vol. 24, no. 12, pp. 4729–4749, 2006. DOI: 10.1109/JLT.2006.885258.

ACRONYMS

2D	Two-Dimensional.
AOM	Acousto-Optical Modulator.
BB	Beam Block.
BS	Beam Sampler.
BSB	Blue Sideband.
COM	Center-of-Mass.
EIT	Electromagnetically Induced Transparency.
GS	Ground-State.
LS	Light-Shift.
MLE	Maximum-Likelihood Estimation.
MS	Mølmer-Sørensen.
NA	Numerical Aperture.
ODF	Optical Dipole Force.
PBS	Polarizing Beam Splitter.
PCF	Photonic Crystal Fiber.
PD	Photodiode.
PI	Proportional-Integral.
POVM	Positive-Operator Valued Measure.
PSD	Power Spectral Density.
RF	Radio-Frequency.
RIN	Relative Intensity Noise.
RMS	Root Mean Square.
RSB	Red Sideband.
RWA	Rotating Wave Approximation.

Acknowledgements

This thesis would not have come to life without the support and advice of many people. I would like to sincerely thank everyone who has contributed, whether through guidance, encouragement, or simply by offering a listening ear. Your support has been invaluable, and I am deeply grateful to each and every one of you.

First and foremost, I would like to express my deepest gratitude to Christian Roos for his continuous guidance throughout this work. Your curiosity, passion, and multifaceted way of thinking have been and continue to be a source of inspiration. Thank you for your unwavering support and for generously sharing your extensive knowledge.

I would also like to thank Lauriane Chomaz for supervising my thesis from the Heidelberg side. Although your primary research field differs from the topic of this work, I am extremely grateful for your interest and thoughtful questions. Thank you for taking the time to support me and for encouraging me in my plans.

My sincere thanks go to the 2D Crystals team for encouraging me—whether it was pushing me up mountains on a bike or helping me tackle the challenges of writing this thesis. Without your guidance, support, and generous sharing of knowledge, this thesis would not have been possible. I have learned an immense amount from all of you and it has been a privilege and a pleasure to work alongside you. In particular, I would like to express my deep gratitude to Artem for his continuous support. I could always come to you with countless questions, which you answered with great patience. You taught me a tremendous amount about optics and the proper setup of optical systems. I truly admire your critical thinking and your ability to solve problems quickly and effectively. Thank you for always taking time for me and helping me out with the numerous (coding) problems I encountered. I am equally grateful to Matthias. Your passion, deep knowledge, and relentless persistence in tackling challenges have been a constant source of inspiration. You are incredibly hardworking, always bring strong and well-thought-out opinions, and have an impressive ability to quickly come up with solutions to problems. Thank you for proof-reading my thesis and always taking time for me to teach me so many things. I really learned a lot from you. I would also like to thank Leo, our newest team member and fellow student from Heidelberg. Thank you for bringing new perspectives, political discussions, curiosity, and spirit into our group. I am looking forward to work with you in the future. I would also like to thank the honorary member of the team, Mariano, for the many enjoyable discussions and for his persistent (though unsuccessful) attempts to convince me to drink coffee — perhaps you'll have better luck during my PhD!

I would like to express my heartfelt gratitude to the entire Blatt division. Although I cannot name everyone individually, it has been immensely rewarding to be part of a team

of colleagues who are always willing to help, exchange ideas, and share their expertise. I am especially grateful to Claudia for her efficient handling of all organizational matters and her unwavering support. I also extend my sincere thanks to the electronics and mechanical workshops for their invaluable assistance and expertise throughout this work.

I am very thankful to Sara and Luise. Although our paths separated for our master's studies to Uppsala, Bremen, and Innsbruck, our friendship, beginning in the first week of our bachelor's program, has remained a constant. I cannot express enough how thankful I am to have you both by my side throughout these years. I am immensely proud of you and of the journey we have taken together. Thank you for your friendship, for all the wonderful memories we created together, for your unwavering support in both good and difficult times, and for always being there with an open ear and kind words whenever I needed them. I would also like to thank Marleen, Marc, Kostas, and Lakshmi for all the wonderful times we shared and your friendship. Thank you for the countless game nights, making me laugh until my belly hurts and all the memories that we shared. Beyond that, I truly hope we will continue our adventures together and manage to go on a few canoe trips, whether in Hamburg, Heidelberg, or Innsbruck.

Next, I want to thank my family for always believing in me and supporting me in every possible way. I cannot put into words how much that means to me, but I know that without your constant encouragement, my studies would never have been possible. Thank you for motivating me to try out new things and for always giving me the confidence to take on challenges. Thank you as well for your help with my many moves and for always being there and supporting me, whenever I needed you. You truly mean the world to me, and I am forever grateful. Thank you, Mama, Papa, Jule, Matti and Enny. Last but certainly not least, I would like to thank Jonas. Thank you for being my greatest supporter and my biggest fan. Words fail me when I try to describe how much you mean to me. Thank you for always being there, for listening to me, for believing in both me and us, and for telling me the things I most needed to hear when I doubted myself. Thank you for patiently helping me with all kinds of problems, for all the unforgettable memories we have created together, and for the countless times you visited me despite the distance.

Erklärung

Ich versichere, dass ich diese Arbeit selbstständig verfasst und keine anderen als die angegebenen Quellen und Hilfsmittel benutzt habe.

Innsbruck, den 23.11.2025,